

III-2

Materials Sciences

BLIU

Evidence for Suppression of Cation Vacancies in Ce:Gd₃Al₂Ga₃O₁₂ Scintillator by Mg Codoping

K. Fujimori¹, M. Kitaura¹, Y. Taira², M. Fujimoto³, Y. Okano⁴, H. Zen⁵, M. Katoh^{3,8}, M. Hosaka⁶, J. Yamazaki³, K. Kamada⁷ and A. Ohnishi¹

¹Faculty of Science, Yamagata University, Yamagata 990-8560, Japan

²National Institute of Advanced Industrial Science and Technology, Tsukuba 305-8568, Japan

³UVSOR Synchrotron Facility, Institute for Molecular Science, Okazaki 444-8585, Japan

⁴Center for Mesoscopic Sciences, Institute for Molecular Science, Okazaki 444-8585, Japan

⁵Institute of Advanced Energy, Kyoto University, Uji 611-0011, Japan

⁶Synchrotron Radiation Research Center, Nagoya University, Nagoya 464-8603, Japan

⁷New Industry Creation Hatchery Center, Tohoku University, Sendai 980-8579, Japan

⁸Hiroshima Synchrotron Radiation Center, Hiroshima University, Higashi-Hiroshima, 739-0046

Recently, it was clarified that Mg codoping is an effective manner to suppress the trapped electron centers responsible for phosphorescence of Ce doped Gd₃Al₂Ga₃O₁₂ (Ce:GAGG) scintillator [1]. The trapped electron centers are formed due to charge compensation of Ga/Al vacancies at the octahedral site. It is thus expected that such Ga/Al vacancies are decreased by Mg codoping. The Gamma-ray induced positron annihilation lifetime spectroscopy (GiPALS) is known to be the unique experimental method that can obtain the information on negatively charged defects such as cation vacancy of bulk crystal [2]. This method makes it clear whether Mg codoping is effective for the suppression of cation vacancies in Ce:GAGG scintillators. In the present study, GiPALS spectra of GAGG, Ce:GAGG, and Ce,Mg:GAGG crystals were measured using ultrashort γ -ray pulses available in BLIU, UVSOR [2]. The preliminary result of the GiPALS has been reported in Ref. [3].

Figures 1(a)-1(c) show PALS spectra of GAGG, Ce:GAGG, and Ce,Mg:GAGG crystals, respectively. These data were obtained at 300 K. The relative intensities and lifetimes were analyzed using the program LT10 [4]. The analyzed results are listed in Table 1. As shown by broken lines in Fig.1, PALS spectra are reproduced by two exponential decay functions with different lifetimes. This fact suggests that there are at least two annihilation sites for positrons. Such two annihilation sites are of intrinsic origins in GAGG, because the relative intensities and lifetimes are almost the same within uncertainties between GAGG and Ce:GAGG. The first and second components are assigned to positron annihilation at bulk and defect states respectively. The lifetimes of the second component are almost the same as those for positron annihilation at the sites of Al monovacancy and Al-O divacancy, which were obtained from the theoretical calculation [5]. On this basis, the second component is assigned to the positron annihilation at the defect sites of Ga/Al monovacancy and Ga/Al-O divacancy.

It was pointed out that Mg codoping has the ability to reduce cation vacancies. Figures 1(a)-1(c) revealed that the relative intensities of the second component are clearly decreased by Mg codoping. From this result, it is

evident that Mg codoping is effective for the suppression of cation vacancies in Ce:GAGG scintillator.

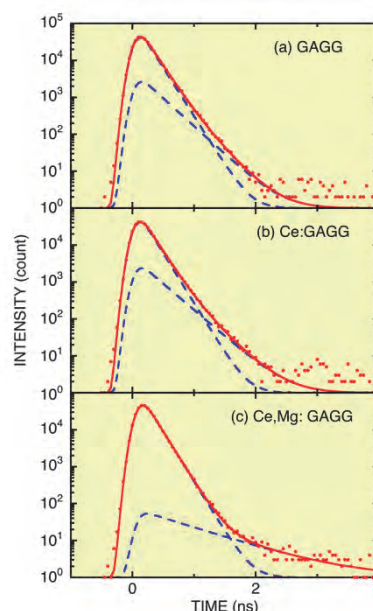


Fig. 1 :GiPALS spectra of (a) GAGG, (b) Ce:GAGG, (c) Ce,Mg:GAGG crystals, measured at 300 K under ultrashort γ -ray pulses.

Table 1. Lifetimes τ_i and relative intensities I_i of the first and second components for GAGG, Ce:GAGG, Ce,Mg:GAGG crystals.

	τ_1 (ps)	I_1 (%)	τ_2 (ns)	I_2 (%)
GAGG	165±1	92±3	286±17	8±3
Ce:GAGG	161±2	92±4	304±17	8±4
Ce,Mg:GAGG	161±1	99±1	812±30	1±1

[1] M. Kitaura *et al.*, Appl. Phys. Lett. **113** (2018) 041906.

[2] Y. Taira *et al.*, Rev. Sci. Instrum. **84** (2013) 053305.

[3] K. Fujimori *et al.*, UVSOR Activity Report 2018 **46** (2019) 44.

[4] D. Giebal and J. Kany, Phys. Procedia **35** (2012) 122.

[5] A. G. Marinopoulos, Eur. Phys. J. B **92** (2019) 242.

BL1B

Effect of Electron-Irradiation on Acceptor State of Germanium

A. Hara and T. Awano

Faculty of Engineering, Tohoku Gakuin University, Tagajo 985-8537, Japan

Germanium (Ge) has better mobility for both electrons and holes than those of silicon (Si). Moreover, as the melting point of Ge is lower than that of Si by approximately 450 °C, crystallization occurs at a lower temperature than Si. Thus, Ge is attracting attention as a semiconductor material for plastic substrates and three-dimensional integrated circuits. However, a large number of holes are generated in polycrystalline Ge due to crystal defects; hence, defect control is an important issue.

Although it is proposed by theoretical approach that Ge vacancies are related with source of the holes, detailed researches have not been disclosed. As Ge has a high dielectric constant, the energy level of the acceptor is expected to be very shallow as group-III impurities; hence, the BL1B line of UVSOR was selected to detect such defects.

Electron irradiation (e-irradiation) is convenient method to introduce vacancies and self-interstitials. Bulk p-type [Indium (In)-doped] Ge samples with 2.0 mm thickness and 12 ohm-cm resistivity were used in this experiment. The samples were irradiated with an electron beam at 4.5 MeV with $3 \times 10^{15} \text{ cm}^{-2}$ at room temperature to introduce lattice defects related to Ge vacancies, and the transmission spectra was measured at liquid He temperature. Samples were annealed at 200, 300, and 400 °C for 30 min in a conventional furnace system to evaluate variations of the spectra.

Figure 1 shows the optical transmission spectra of the In-acceptor [1,2]. Sharp lines correspond to electronic transition between ground and excited states. Owing to the complex structure of the Ge valence band, many lines exist. Figure 1 shows the spectra of as-grown and as-e-irradiated samples; in addition, samples annealed at 200, 300, and 400 °C.

Intensity of the In-acceptor decreased after e-irradiation, but increased and returned to that of as-grown sample with increasing annealing temperature at 400 °C. This indicates that e-irradiation introduced donors that were eliminated at 400 °C. Thus, simple structural defects, such as vacancies, self-interstitials and their aggregates, are not the origin of holes because the holes survive in polycrystalline Ge annealed at 500 °C.

In addition, it was clarified that the new sharp lines related to effective-mass states did not form between 20 and 100 cm^{-1} . The thermal stability of e-irradiation defects and hole-related defects generated in poly-Ge are different. Thus, more complex defects including impurities may be related to the generation center of holes.

In summary, optical transmission spectra of e-irradiated Ge were measured at liquid He temperature. It was found that e-irradiation generated donors that

were eliminated at temperatures at 400 °C. This indicates that simple structure, such as vacancies, self-interstitials and their aggregates, are not the origin of holes. In addition, new lines related to effective-mass states were not found.

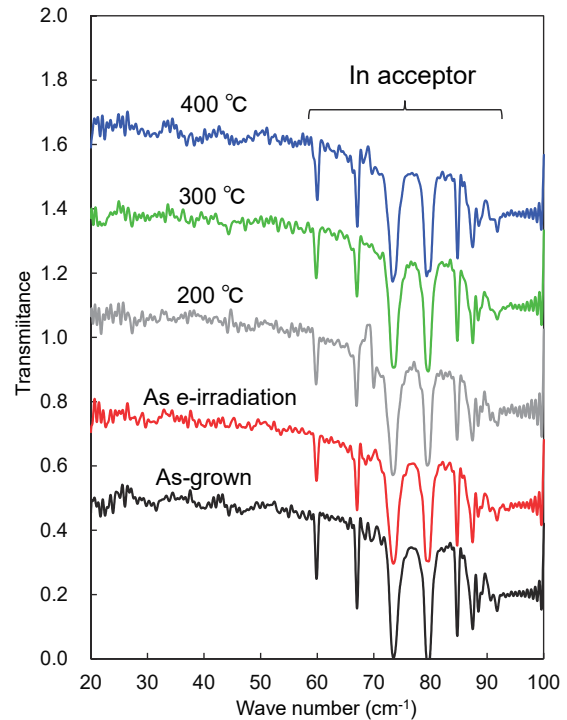


Fig. 1. Transmittance of Ge.

[1] R. L. Jones and P. Fisher, *J. Phys. Chem. Solids* **26** (1965) 1125.

[2] W. Kohn, in *Solid State Physics*, ed. F. Seitz and D. Turnbull (Academic Press, New York, 1957) Vol. **5**, p. 257.

BL1B

Change of Phase Transition Temperature of KDP Single Crystal by Alanine Doping

Z. Mita¹, A. Goto¹, H. Watanabe^{1,2} and S. Kimura^{1,2}

¹Graduate School of Frontier Biosciences, Osaka University, Suita, 565-0871, Japan

²Department of Physics, Graduate School of Science, Osaka University, Toyonaka 560-0043, Japan

Second harmonic generation (SHG) is used in laser pointers and other compact laser devices. Among many SHG materials, potassium dihydrogen phosphate (KH_2PO_4 , KDP) is well known and used in applications. Recently, it has been reported that the doping of 0.5-wt% alanine in KDP improves the SHG efficiency by a factor of about two [2].

However, many basic physical properties about the origin of the increase of the SHG efficiency due to the alanine doping has never been reported so far. To clarify the origin of the SHG efficiency change by the doping, we have measured polarization and temperature dependences of optical conductivity spectra of single-crystalline samples of pristine KDP and L-alanine-doped KDP.

We have grown KDP single crystals with and without the doping of 0.5-wt% L-alanine using the solvent evaporation method and confirmed to be orthorhombic structure at room temperature by taking X-ray Laue diffraction patterns. Anisotropic optical reflectivity spectra in the terahertz (THz) region around the phase transition temperature from 117 K to 124 K has been measured by using BL1B of UVSOR-III and laboratorial equipments. The obtained spectra were converted to optical conductivity $[\sigma(\omega)]$ spectra by the Kramers-Kronig analysis. Temperature dependence of the $\sigma(\omega)$ spectrum with the electric vector perpendicular to the c axis ($E \perp c$) in the THz region is shown in Fig. 1.

As shown in Fig. 1, we found a unique peak appearing only at the low-temperature phase (namely I). By the fitting of a Gaussian function to the peak I after subtracting the high-temperature-phase spectrum, the temperature dependences of the energy, intensity, and width of the peak were obtained as shown in Fig. 2. The peak energy shifts to the higher energy side and the intensity and width increases as the temperature decreases. The peak energy shift suggests the contraction of the lattice constant at lower temperature, so the spectra in Fig. 1 are considered to be the spectra with the electric vector parallel to the a axis because only the axis monotonically shrinks of the three independent axes [1]. Figure 3 shows the temperature dependence of the peak area of I. For pristine KDP, the phase transition temperature can be evaluated as 122 K, which is the same as that reported in the previous work [1]. For 0.5-wt% doping, the transition temperature slightly increased. To clarify the doping effect systematically, further experiments with more doping amounts or detailed temperature steps are needed.

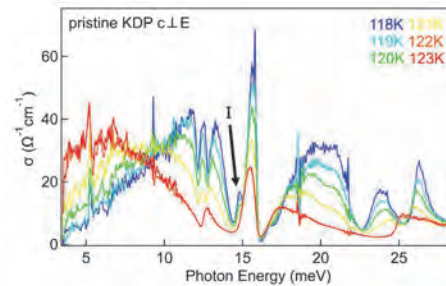


Fig. 1. Anisotropic optical conductivity $[\sigma(\omega)]$ spectra at temperatures from 118 to 123 K in the THz region perpendicular to the c -axis ($E \perp c$). A peak at 14.8 meV (namely I) appears below the phase transition temperature of 122 K.

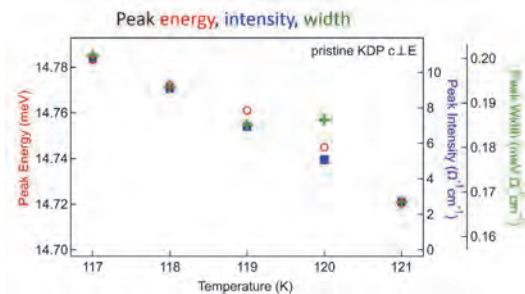


Fig. 2. Peak energy (red), intensity (blue), and width (green) of the 14.8-meV peak as a function of temperature.

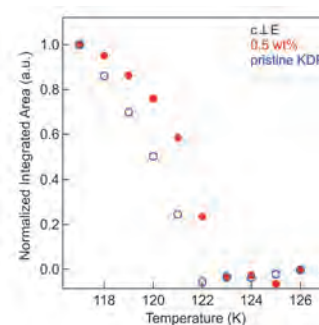


Fig. 3. Temperature dependence of the area of the 14.8-meV peak of pristine KDP (blue) and 0.5-wt% L-alanine-doped KDP (red). The area is normalized by the intensity at 117 K.

- [1] G. Busch and P. Scherrer, *Naturwiss.* **23** (1935) 737.
 [2] K. D. Parikh *et al.*, *Cryst. Res. Technol.* **45** (2010) 603.

BL2A

Mo L_{III}-edge XANES Study of Catalytically Active Mo Species on H-MFI for Methane Dehydroaromatization with Hydrogen

H. Aritani¹, K. Kuramochi², R. Yamazaki², S. Sato¹, Y. Nozawa¹, A. Kato¹ and A. Nakahira³
¹Graduate School of Engineering, Saitama Institute of Technology, Fukaya 369-0293, Japan ²Advanced Science Research Laboratory, Saitama Institute of Technology, Fukaya 369-0293, Japan
³Graduate School of Engineering, Osaka Prefecture University, Sakai 599-8531, Japan

Molybdenum-modified H-MFI zeolite is a typical GTL (Gas To Liquid) catalyst for methane dehydroaromatization (Methane To Benzene: MTB). On the Mo/H-MFI catalysts, it is a serious problem for development of MTB reaction, and thus, clarification of the deactivation process over the catalysts is one of the important points. Not only carbon deposition on acid sites of H-MFI but also excess carbonization of active Mo species causes the deactivation of MTB. Hydrogen addition to methane reactant is effective for inhibiting the deactivation [1]. However, reductive effect for active Mo species (well dispersed Mo₂C, in major) cannot be avoided. In the present study, Mo L_{III}-edge XANES study is introduced to characterize the active Mo-carbide species on H-MFI after the methane dehydroaromatization with H₂. For inhibiting excess Mo carburization, V co-modification effect on Mo/H-MFI has also been studied.

Mo(5wt%)/H-MFI and Mo-V/H-MFI catalysts were prepared by impregnation of H-MFI (Si/Al₂=30-72) support with MoO₂(acac)₂-CHCl₃ or MoO₂(acac)₂-VO(acac)₂-CHCl₃ solution (Mo/V=10-40), and followed by drying overnight and calcination at 773 K. The reaction condition for methane dehydroaromatization was described in a previous report [2,3]. Mo L_{III}-edge XANES spectra were obtained in BL2A of UVSOR-IMS in a total-electron yield mode using InSb double-crystal monochromator. Photon energy was calibrated by using Mo metal-foil at Mo L_{III}-edge, and normalized XANES spectra were presented by using REX-2000 (Rigaku) software.

As shown in Fig. 1 (top), edge energy of L_{III}-edge strongly relate to the valence of Mo ions. Using the references of Mo metal and α -Mo₂C, the reduction degree of active Mo species on H-MFI after the MTB reaction with H₂ are evaluated. For the XANES spectra of Mo-H-MFI catalysts in Fig. 1 (middle), the active Mo species are likely due to deeply reduced carbide species which is more carbonized than Mo₂C. The reduction degree almost independent on H₂ co-feed in the MTB reaction, and therefore, The MoC_x (x>0.5) species are formed through the deep reduction by methane. On these catalysts, H₂ co-feed (1-2 %) affect the inhibition of coke deposition. To suppress excess reduction, V co-modification on Mo/H-MFI (in Mo/V=10) has been found to be effective towards the enhancement of reactivity. In Fig. 1 (bottom), XANES spectra of these catalysts are shown. By V co-modification, the reduction degree of Mo species

slightly suppressed in MTB reaction. The study about optimal Mo/V ratio is now in progress.

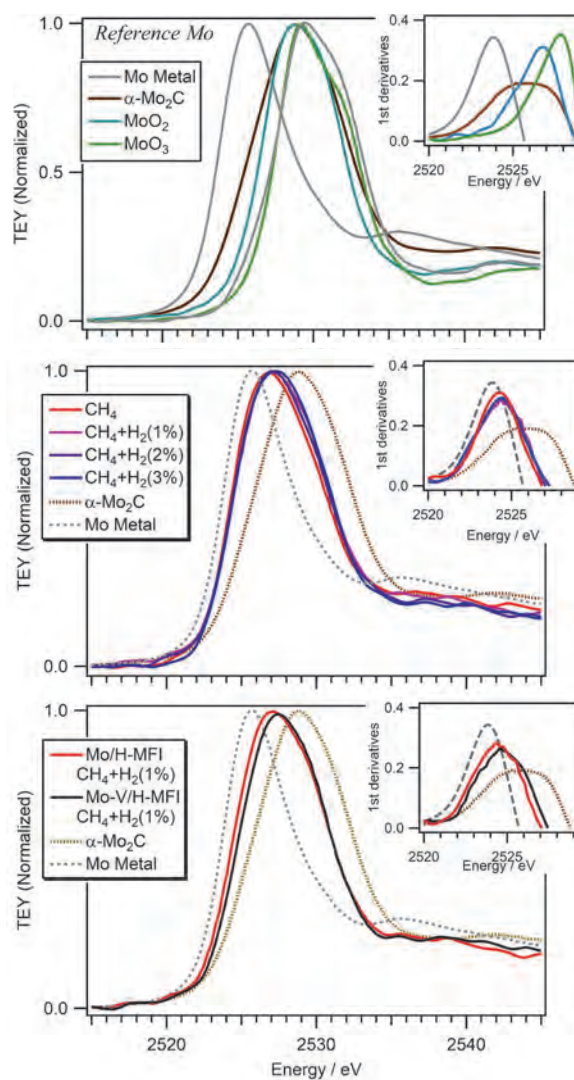


Fig. 1. Mo L_{III}-edge XANES of reference Mo samples [top], Mo/H-MFI catalysts reacted with CH₄-H₂(0-3 %) [middle], and V co-modified catalysts reacted with CH₄-H₂(1 %). First derivatives of XANES are shown in upper right of each figure.

- [1] H. Aritani *et al.*, J. Environm. Sci. **21** (2009) 736.
 [2] H. Aritani *et al.*, UVSOR Activity Report 2018 **46** (2019) 49.
 [3] H. Aritani *et al.*, UVSOR Activity Report 2017 **45** (2018) 44.

BL2A

Local Environment of Mg²⁺ on Hydroxyapatite Surface

T. Nakamura, R. Kawanabe, H. Murata and A. Nakahira

Department of Materials Science, Osaka Prefecture University, Sakai 599-8531, Japan

Hydroxyapatite (Ca₅(PO₄)₃OH, HAp) is a main inorganic component of human bones and teeth. It has both of cation- and anion-exchange abilities. In human bodies, it is exposed to various ions of body fluids. Indeed, biological HAp is not pure but contains various kinds of defects and impurity ions, which affect properties of HAp [1,2]. Therefore, it is important to investigate reactions of these ions with the surface of HAp.

Mg²⁺ is one of the main impurities of human bones, which plays an important role of bone-remodeling. In the present study, we investigated local environments of Mg²⁺ reacted on the surface of HAp using X-ray absorption near edge structure (XANES).

HAp samples were synthesized by the solution-precipitation method [3]. Starting materials were 0.1 mol/L Ca(NO₃)₂ and 0.1 mol/L (NH₄)₂HPO₄ aqueous solutions. They were mixed and matured at 80 °C for 5 h. The pH was kept at 10 by adding 0.1 mol/L KOH aqueous solution. In order to prevent formation of Ca²⁺ vacancies, the initial Ca/P was set to 2, which is larger than stoichiometric composition of HAp, 1.67. Then, they were filtrated, washed by ion-exchanged water and dried at 50 °C. Mg²⁺-doped HAp samples as a reference material were also synthesized by same procedures with addition of 0.1 mol/L Mg(NO₃)₂ aqueous solution to starting materials.

Obtained HAp powders were pressed into pellets of 10 mm in diameter. Parts of them were calcined at 1100 °C. The pellets were soaked in 50 mL of 0.01 mol/L Mg(NO₃)₂ aqueous solution for 10 min. Then, they were well washed by ion-exchanged water.

Mg-K XANES spectra were collected by the partial fluorescent (PFY) mode using a silicon-drift detector (SDD) at BL2A in UVSOR. Fluorescence X-ray spectra were de-convoluted using gauss functions, which was reported elsewhere [4]. X-ray beams were monochromated using beryl double crystals. Samples were mounted using carbon tapes on an Ti plate.

X-ray diffraction measurements indicated that samples consists of HAp and no secondary phases were observed even after calcination at 1100°C. This result indicates that our HAp samples have stoichiometric composition [1,3].

Figure 1 shows Mg-K XANES of Mg²⁺-adsorbed samples. They have the same features to those of Mg²⁺-doped HAp. This results indicated that Mg²⁺ was incorporated into HAp crystals. As-dried HAp gave smooth spectra but ones calcined at 1100 °C gave rather noisy spectra. In this case, we observed only 1 cps of fluorescence X-ray of Mg even at the peak, 1312 eV. Such weak fluorescence X-ray of Mg indicated that HAp calcined at 1100 °C caught only

small amounts of Mg²⁺. Since the as-dried HAp samples have higher solubility in water than ones calcined at 1100 °C [3], there results implies that the reaction of Mg²⁺ with surface of HAp proceeds via a dissolution-reprecipitation process.

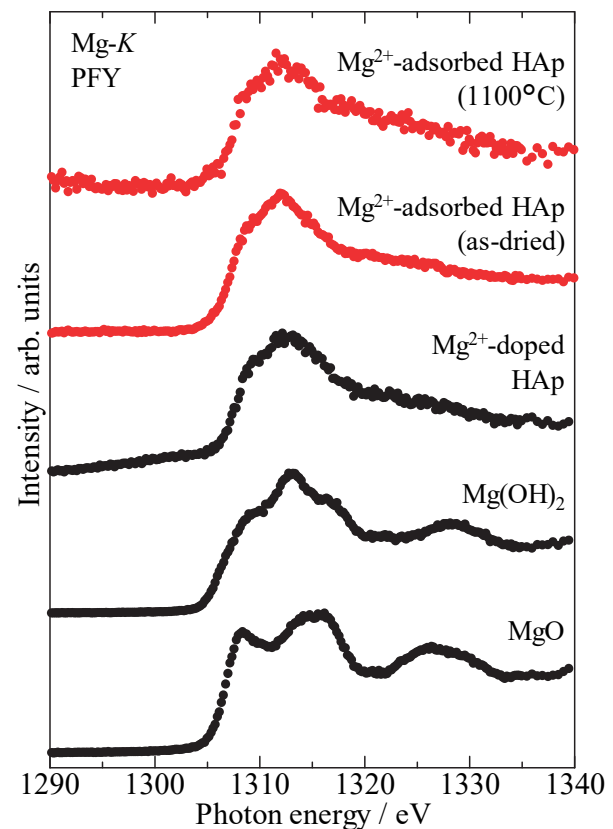


Fig. 1. Mg-K XANES of Mg²⁺-adsorbed HAp samples (red lines) and reference materials (black lines).

[1] J. C. Elliott, *Structure and Chemistry of the Apatites and Other Calcium Orthophosphates* (Elsevier, Amsterdam, 1994).

[2] E. Boanini *et al.*, *Acta Mater.* **6** (2010) 1882.

[3] K. Shitara *et al.*, *J. Asian Ceram. Soc.* **2** (2014) 64.

[4] H. Murata, *UVSOR Activity Report 2018* **46** (2019) 53.

BL2A

XAFS Analysis of Ga₂O₃ Loaded Al₂O₃ Photocatalysts for Carbon Dioxide Reduction

T. Yoshida¹, M. Akatsuka², R. Ito², A. Ozawa², M. Yamamoto¹ and T. Tanabe¹¹Advanced Research Institute for Natural Science, Osaka City University, Osaka 558-8585, Japan²Graduate School of Engineering, Osaka City University, Osaka 558-8585, Japan

Gallium oxide (Ga₂O₃) photocatalysts can reduce CO₂ to CO with H₂O, although the efficiency of CO production is very low [1]. Generally, photocatalytic activity depends on the local structure of the surface active site. However, there are few works investigating the influence of Ga₂O₃ local structure on the CO₂ photoreduction activity. In the present study, we have focused to geometrical or morphological effects of Ga₂O₃ particles supported on Al₂O₃ (referred as Ga₂O₃/Al₂O₃, hereafter) for CO₂ reduction under UV light irradiation. The reasons of utilization of Al₂O₃ as the support are twofold, (1) to increase surface area of Ga₂O₃, as evidenced by the observation that Ga₂O₃/Al₂O₃ was used for the removal of NO_x, and (2) that Al₂O₃ hardly show the photocatalytic activity for both water splitting and CO₂ reduction.

Ga₂O₃/Al₂O₃ samples were prepared by impregnation of γ -Al₂O₃ with aqueous solution of gallium nitrate followed by dry and calcination in the air at 773 K for 4 h, as described elsewhere [2]. The loading amounts of Ga₂O₃ were 1, 5, 10 and 20 wt%. Unsupported Ga₂O₃ and Ga₂O₃/SiO₂ samples were also prepared in the similar way to Ga₂O₃/Al₂O₃. The Ga₂O₃ sample was employed for XRD measurement to identify the crystal phase of Ga₂O₃. Surface areas of all the prepared samples were measured by BET method. Ga L₃-edge XANES were measured with the beam line of BL2A at UVSOR, Institute for Molecular Science in Japan, in a total electron yield mode.

Photocatalytic CO₂ reduction with H₂O was carried out over the Ga₂O₃/Al₂O₃ sample. CO production rates over 5, 10 and 20 wt% Ga₂O₃/Al₂O₃ samples were higher than those over β -Ga₂O₃ and Al₂O₃ samples, while over 1 wt% Ga₂O₃/Al₂O₃, it was almost the same as that over Al₂O₃ sample.

Unsupported Ga₂O₃ was identified as γ -Ga₂O₃ by the XRD pattern. On the other hand, very weak and broad lines due to Ga oxide phase were observed for Ga₂O₃/Al₂O₃ samples but could not be identified clearly. Based on the BET measurements for a bare Al₂O₃ and Ga₂O₃/Al₂O₃ samples, we roughly estimated the surface area of Ga oxide phase in each Ga₂O₃/Al₂O₃ sample by subtracting the component of Al₂O₃ support. We regarded that the surface areas of Ga oxide phase are almost the same each other.

Figure 1 shows Ga L₃-edge XANES spectra. Two peaks around 1121 and 1123 eV are observed for Ga₂O₃/Al₂O₃ samples. A peak appeared near 1123 eV is caused by a Ga-O-Al bond [3], indicating that some interaction between Ga₂O₃ and Al₂O₃ occurred in all the

samples. On the other hand, Ga₂O₃/SiO₂ samples showed no prominent peaks in XANES, suggesting that Ga species are highly dispersed on SiO₂ surface.

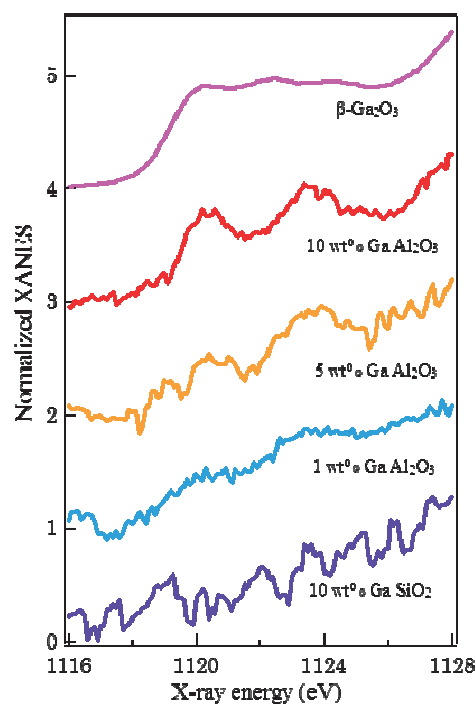


Fig. 1. Ga L₃-edge XANES spectra of all prepared samples. The spectrum of β -Ga₂O₃ is also given for comparison.

[1] H. Yoshida, L. Zhang L, M. Sato, T. Morikawa, T. Kajino, T. Sekito, S. Matsumoto and H. Hirata, *Catal. Today*, **251** (2015) 132.

[2] K. Nishi, K. Shimizu, M. Takamatsu, H. Yoshida, A. Satsuma, T. Tanaka, S. Yoshida and T. Hattori, *J. Phys. Chem. B* **102** (1998) 10190.

[3] K. Shimizu, M. Takamatsu, K. Nishi, H. Yoshida, A. Satsuma, T. Tanaka, S. Yoshida and T. Hattori, *J. Phys. Chem. B* **103** (1999) 1542.

BL2A

Local Structure Investigations of Al in Spinel Compounds Induced on Swift Heavy Ion Irradiations

S. Yoshioka¹, K. Yasuda¹, S. Matsumura¹, E. Kobayashi² and K. Okudaira³

¹Department of Applied Quantum Physics and Nuclear Engineering Kyushu University, Fukuoka 819-0395, Japan

²Kyushu Synchrotron Light Research Center (SAGA-LS), Tosu 841-0005, Japan

³Graduate School of Advanced Integration Science, Chiba University, Chiba 263-8522, Japan

Magnesium aluminate oxide (MgAl_2O_4) is one of the common spinel compounds. Since it shows a variety of interesting physical and chemical properties, its microstructure has been extensively investigated. A cationic disordered MgAl_2O_4 spinel is represented by the formula of $[\text{Mg}_{1-x}\text{Al}_x](\text{Mg}_x\text{Al}_{2-x})\text{O}_4$, where the square brackets and the parentheses denote the tetrahedral and octahedral sites, respectively. The variable x is called the inversion parameter, which quantifies the cation disorder. Radiation with swift heavy ions (SHIs) interacts with materials and causes the structural change. It is therefore applied to material processing, modifications, etc. SHI irradiation provides high energy deposition through electronic stopping to the materials. SHIs in insulating solid materials are known to leave trails of damage along the ion path with a diameter of several nanometers. Structural change related to the cationic disorder has been also observed in MgAl_2O_4 with SHI irradiation using transmission electron microscopy observation. In this study, we clarify local coordination of each cation element, on which we conducted synchrotron radiation-based X-ray analysis.

Plates of poly-crystal MgAl_2O_4 with the shape of $10 \times 4 \times 0.5$ mm were used in this study. These specimens were irradiated with 200 MeV Xe ions to fluences of $1 \times 10^{13} \text{ cm}^{-2}$ at the HI beamline of the tandem ion accelerator facility in the Japan Atomic Energy Agency (JAEA)-Tokai. At the beginning of each paragraph, two space characters should be inserted as an indent. Mg K -edge and Al K -edge XANES measurements were performed at the BL2A beamline of UVSOR Okazaki, Japan, using the partial fluorescence yield method (PFY). A KTiOPO_4 (KTP) double crystal monochromator defined Mg K and Al K absorption edges in the energy region from 1290 to 1340 eV and 1540 to 1610 eV, respectively. The samples were set with their surface perpendicular to the incident X-ray beam. Fluorescence X-rays of Mg $K\alpha$ and Al $K\alpha$ were collected using an energy dispersible silicon drift detector (SDD). All measurements of XANES spectra were carried out in vacuum of 1×10^{-5} Pa at room temperature.

Figure 1 shows the XANES spectra with the Mg K -edge (1300 eV) acquired from the MgAl_2O_4 samples before and after irradiation with 200 MeV Xe ions with fluences of $1 \times 10^{13} \text{ cm}^{-2}$. The Mg K -edge spectrum features of the irradiated MgAl_2O_4 sample were clearly different from those of the pristine sample.

Especially, both the peak intensity ratio of A/B and C/B decreased after the irradiation. The spectrum shapes on Al K -edge also changed by the irradiation. Detailed analyses on the local environment of Mg and Al in the MgAl_2O_4 irradiated with SHI are in progress by combined use of the XANES and the first principles band structure calculations.

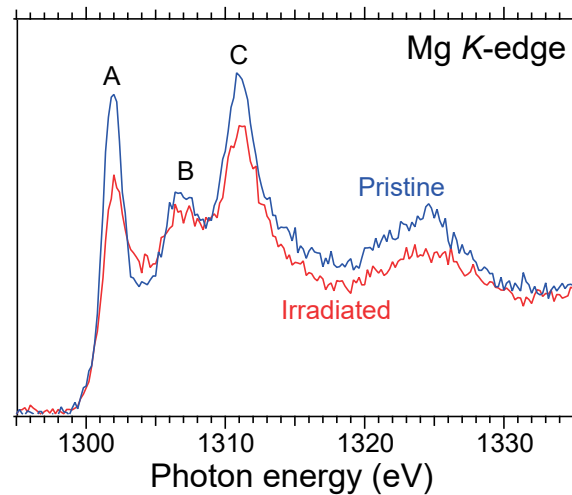


Fig. 1. Mg K -edge XANES spectra of pristine and irradiated MgAl_2O_4 with 200 MeV Xe ions to fluences of $1 \times 10^{13} \text{ cm}^{-2}$.

[1] T. Yamamoto *et al.*, Nucl. Instrum. Meth. B. **245** (2006) 235.

[2] K. Yasuda *et al.*, Nucl. Instrum. Meth. B. **250** (2006) 238.

BL2A

X-ray Absorption Analysis of Rb Ions in FAPbI₃

K. Osonoe^{1,2}, M. Tohyama¹, M. Ishida¹, K. Hirose^{1,2} and T. Yamamoto^{1,3,4}

¹Faculty of Science and Engineering, Waseda University, Tokyo 169-8555, Japan

²Institute of Space and Astronautical Science, JAXA, Sagami-hara 252-5210, Japan

³Institute of Condensed-Matter Science, Waseda University, Tokyo 169-8555, Japan

⁴Kagami Memorial Research Institute for Materials Science and Technology, Waseda University, Tokyo 169-0051, Japan

Organic-inorganic hybrid perovskite-type solar cells have attracted significant interest owing to their low-cost fabrication and high performance, exhibiting a rapid increase in power conversion efficiency after the discovery of its application for solar-cells [1]. The organic-inorganic hybrid perovskite is used as a light-absorption layer in the stacking structure of the thin films in a perovskite solar cells (PSC). Although methyl-ammonium lead tri-iodide (CH₃NH₃PbI₃; hereafter MAPbI₃) was used at early stage, MAPbI₃ is not stable at high temperature and under humid condition. Recently, FAPbI₃, FA = formamidinium: CH(NH₂)₂, based materials have been investigated to get higher stability and efficiency than MAPbI₃. In these researches, cations at FA site and anions were often partially replaced by other ions to control the tolerance factor, which is a well-known parameter to estimate a stability of perovskite structure [2]. It was reported among such studies that Rb-doping could enhance the light absorption efficiency. However, the mechanism of such enhancement of efficiency has not yet been understood. Although it is important to know a local environment of such doped ions in the host materials in an atomic scale, such analysis is often skipped due to a difficulty of the analysis for dilute dopants. In the present study, we have synthesized Rb-doped (CsFAMA)Pb(I Br)₃ and the local environment of doped Rb ions in the synthesized materials have been investigated by the X-ray absorption near-edge structure (XANES) measurements.

Thin films of Rb-doped (CsFAMA)Pb(I Br)₃ were prepared by the spin coating method on the glass substrate. After the coatings, thermal treatment was given changing the temperature. Rb concentration was approx. 3 at% to CsFAMA. Synthesized films were characterized by the conventional powder X-ray diffraction method using Cu K α X-rays, which showed all the synthesized films crystallized in a singular phased perovskite structure. Sample morphology was also observed by the scanning electron microscope (SEM), which showed the grain size changes according to the temperature of thermal treatment. Rb L₃-edge X-ray absorption near edge structure (XANES) spectra of synthesized films were observed at BL2A in UVSOR by the total electron yield method. Sample films on the glass substrate were put on the carbon adhesive tape, which were attached on the first dinode of the electron multiplier. In order to avoid charge-up of the sample films on the insulating glass substrate, carbon adhesive

tape is also attached on the film surface and dinode, which could keep the electrical conductivity between sample film and dinode.

Observed Rb-L₃ XANES spectra are shown in Fig. 1 together with the reference spectrum of RbI. Significant difference between these spectra depending upon the grain size could be clearly seen. From the results, we could confirm that the local environment of Rb ions is sensitive to change in grain size of (CsFAMA)Pb(I Br)₃.

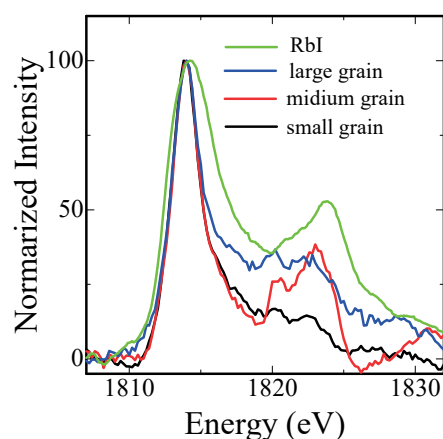


Fig. 1. Observed Rb-L₃ XANES spectra of RbI and (RbCsFAMA)Pb(I Br)₃.

[1] A. Kojima *et al.*, *J. Am. Chem. Soc.* **131** (2009) 6050.

[2] S. Burger *et al.*, *J. Mater. Chem. A* **6** (2018) 21785.

BL2A, BL5B

Luminescence Decay Curves of Inorganic Scintillators Excited with Soft X-ray Pulses under Single Bunch Operation Mode

K. Kawai¹, H. Zen², E. Nakamura³, M. Kitaura¹, K. Kamada⁴ and A. Ohnishi¹

¹Faculty of Science, Yamagata University, Yamagata 990-8560, Japan

²Institute of Advanced Energy, Kyoto University, Uji 611-0011, Japan

³UVSOR Synchrotron Facility, Institute for Molecular Science, Okazaki 444-8585, Japan

⁴New Industry Creation Hatchery Center, Tohoku University, Sendai 980-8579, Japan

The single bunch operation mode in UVSOR synchrotron facility is one of the advantages over other synchrotron facilities. This mode is characterized by the repetitive light pulses of sub-micro second. Users can carry out time-resolved spectroscopy experiment of solids, liquids, and gases. On the other hand, the beamlines used under the single bunch operation mode are not so many, so we have to develop experimental systems to explore unique time-resolved spectroscopy with vacuum ultraviolet (VUV) light and soft X-ray (SX). Actually, there are many proposals for the usage of VUV and SX photons in measurements of luminescence decay curves.

In order to respond such user's request, we tried to measure luminescence decay curves of typical inorganic scintillators at the BL2A and BL5B beamlines. The former and latter allow us to use photons in SX and VUV regions, respectively. The luminescence detection systems with a time correlated single photon counting were installed at the two beamlines. Here, we report the results of luminescence spectra and luminescence decay curves of Ce-doped $\text{Gd}_3\text{Al}_2\text{Ga}_3\text{O}_{12}$ (Ce:GAGG) and Mg-codoped Ce:GAGG scintillators, measured at 300 K under excitation with SX photons of 1.05 keV.

Figure 1 shows luminescence spectra of Ce:GAGG and Ce,Mg:GAGG scintillators. The intensities were normalized to unity at the maximum of Ce:GAGG. A prominent band is observed around 550 nm. This band has been assigned to $\text{Ce}^{3+} 5d-4f$ transition [1]. The Ce^{3+} band is weakened by Mg codoping. Luminescence decay curves of the 550-nm band were shown in Fig. 2. The luminescence decay curves are composed of short- and long-lived components. The long-lived component appears as a pile-up component. This component is enhanced under host excitation with VUV and SX photons, compared to $\text{Ce}^{3+} 4f-5d$ excitation with visible photons [2]. Since the luminescence intensity is given by time-integration of the decay curve, it should be clearly decreased by Mg-codoping. This situation can be seen in Fig. 1. The lifetime of the short-lived component also becomes shorter, and the pile-up component is weakened. These results are in agreement with those in Refs. 3.

Now, the BL2A and BL5B beamlines are ready to use SX and VUV light pulses under the single bunch operation mode. Especially, the research and development of scintillators, requiring high-energy light pulses, may be suitable. Users who want to use VUV

and SX pulses are welcome to the use of these beamlines.

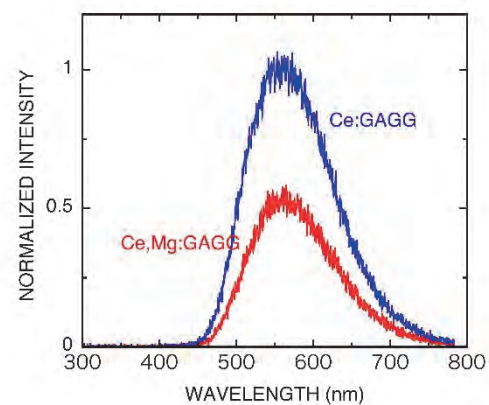


Fig. 1: Luminescence spectra of Ce:GAGG, and Ce,Mg:GAGG scintillators, measured at 300 K under excitation with SX photons of 1.05 keV.

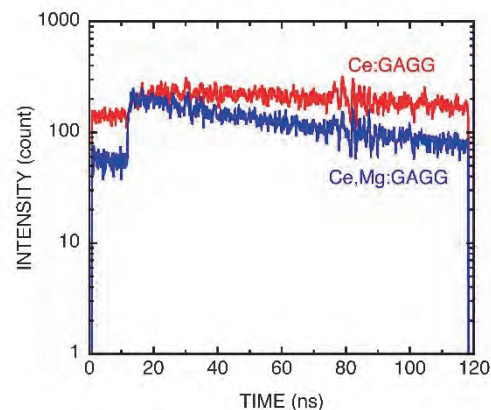


Fig. 2: Luminescence decay curves of Ce:GAGG, and Ce,Mg:GAGG scintillators, measured at 300 K under excitation with SX photons of 1.05 keV.

[1] M. Kitaura *et al.*, *J. Appl. Phys.* **113** (2014) 041906.

[2] M. Kitaura *et al.*, *Opt. Mater.* **41** (2015) 45.

[3] K. Kamada *et al.*, *Opt. Mater.* **41** (2015) 63.

[4] M. Kitaura *et al.*, *Appl. Phys. Express* **9** (2016) 072602.

BL3B

Intrinsic Luminescence from Self-trapped Excitons in $(\text{Ca}_{1-x}\text{Na}_x)_2(\text{Mg}_{1-2x}\text{Al}_{2x})\text{Si}_2\text{O}_7$ Single Crystals upon Vacuum UV Excitation

N. Kodama, T. Takahashi, T. Inoue and Y. Takahashi

Faculty of Engineering and Resource Science, Akita University, Akita 010-8502, Japan

Na- and Al-substituted melilite $(\text{Ca}_{1-x}\text{Sr}_x)_2\text{MgSi}_2\text{O}_7$ crystals are expected to exhibit incommensurate modulations similarly to Sr-substituted $(\text{Ca}_{1-x}\text{Sr}_x)_2\text{MgSi}_2\text{O}_7$ [1]. To date, little research has focused on the formation of self-trapped excitons (STEs) in terms of the dimensionality and modulation of the structure. We report intrinsic luminescence from STEs. In addition, we examine the correlation between the intensity and bandwidth of intrinsic luminescence and the two-dimensionality and structure modulation in $(\text{Ca}_{1-x}\text{Na}_x)_2(\text{Mg}_{1-2x}\text{Al}_{2x})\text{Si}_2\text{O}_7$ ($x = 0.0, 0.05, 0.10, 0.25$) crystals.

Absorption, luminescence, and excitation spectra of STEs in $(\text{Ca}_{1-x}\text{Na}_x)_2(\text{Mg}_{1-2x}\text{Al}_{2x})\text{Si}_2\text{O}_7$ ($x = 0, 0.05, 0.10, 0.25$) single crystals were measured in the temperature range of 5-293 K using the undulator beamline BL3B at the UVSOR facility. Under VUV excitation at 160 and 70 nm, intrinsic luminescence from STEs was observed in these crystals.

Figures 1(a)-1(d) show the luminescence spectra for $(\text{Ca}_{1-x}\text{Na}_x)_2(\text{Mg}_{1-2x}\text{Al}_{2x})\text{Si}_2\text{O}_7$ ($x = 0.0, 0.05, 0.10, 0.25$) excited at 160 nm in the 5-293 K range. The luminescence spectra of $(\text{Ca}_{1-x}\text{Na}_x)_2(\text{Mg}_{1-2x}\text{Al}_{2x})\text{Si}_2\text{O}_7$ with $x = 0.0, 0.05, 0.10$, and 0.25 consisted of two broad bands with peaks at 246-255 nm and 311-332 nm, associated with STE(I) and STE(II) in the 5-293 K range. The STE(I) and STE(II) luminescence intensities decreased rapidly with increasing temperature. With increasing x , the intensity of STE(I) passed through a maximum at the intermediate fraction $x = 0.10$. On the other hand, the intensity of STE(II) increased with increasing x . There are two plausible explanations for the dependence of luminescence intensities on the Na/Al fraction, x , involving (i) a two-dimensional effect or (ii) an incommensurate structural modulation effect.

The magnitude of two-dimensionality for $(\text{Ca}_{1-x}\text{Na}_x)_2(\text{Mg}_{1-2x}\text{Al}_{2x})\text{Si}_2\text{O}_7$ increased with increasing x due to the larger ionic radius involved in substituting Na^{2+} . Thus, the dependence of the STE(II) intensity on x can be explained in terms of a two-dimensional effect. On the other hand, the dependence of the STE(I) luminescence cannot be accounted for by two-dimensionality, because the maximum of the intensity varies with x . The other possible explanation is that the structural modulation effect of an incommensurate phase increases the number of local sites with larger distortion potentials. The formation of STEs and the luminescence intensity may be strongly affected by whether or not the crystals form a modulated structure (commensurate or incommensurate phase) and by the modulation amplitude. We found that the $(\text{Ca}_{1-x}\text{Na}_x)_2(\text{Mg}_{1-2x}\text{Al}_{2x})$

Si_2O_7 crystal with $x = 0.10$ showed the most intense luminescence among the four compositions examined ($x = 0.0, 0.05, 0.10$, and 0.25). The Na- and Al-substituted $(\text{Ca}_{1-x}\text{Sr}_x)_2\text{MgSi}_2\text{O}_7$ crystals with Na fractions, x , ranging from 0.0 to 0.25 are expected to exhibit two-dimensional incommensurate modulations with a modulation vector along $[110]$ and $[1\bar{1}0]$, depending on the composition, similarly to Sr-substituted $(\text{Ca}_{1-x}\text{Sr}_x)_2\text{MgSi}_2\text{O}_7$ [1]. These structural changes with varying Na composition suggest that the intense luminescence at $x = 0.10$ is mainly due to a structural modulation effect. The Na composition dependence of the bandwidths of STE(I) and (II) suggests inhomogeneous broadening of the STE luminescence due to the random distributions of the $\text{Ca}^{2+}/\text{Na}^+$ and $\text{Al}^{3+}/\text{Mg}^{2+}$ sites; this distribution creates different environments for SiO_4 and AlO_4 tetrahedra than STE sites followed by incommensurate modulation.

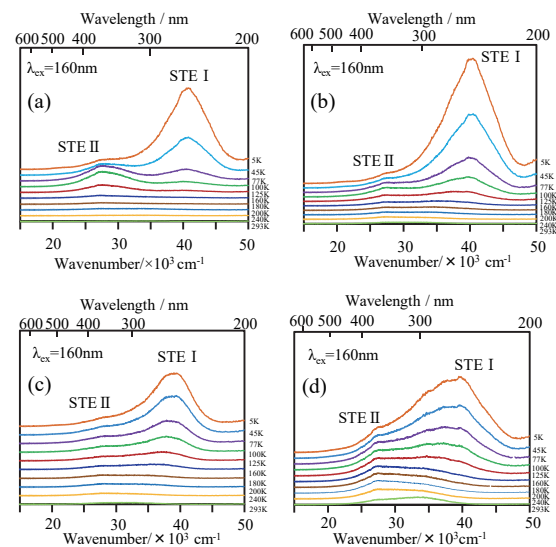


Fig. 1. Dependence of intrinsic luminescence on Na fraction, x , in $(\text{Ca}_{1-x}\text{Na}_x)_2(\text{Mg}_{1-2x}\text{Al}_{2x})\text{Si}_2\text{O}_7$: (a) $x=0.0$, (b) $x=0.05$, (c) $x=0.10$, and (d) $x=0.25$ under excitation at 160 nm in the temperature range 5-293 K.

[1] J.C. Jand, M. Schosnig, A.K. Schapaer, K. Ganster, H. Ragaer and L. Toth, Phys. Chem. Minerals **26** (1998) 128.

BL3B, BL5B

Evaluation of Fluorescence Lifetimes of Scintillators for High-energy Particle Experiments

H. Ikeda, H. Oikawa, Y. Hiruma, M. Kitaura, A. Ohnishi, Y. Tajima and H.Y. Yoshida
 Department of Physics, Yamagata University, Yamagata 990-8560, Japan

Recently, the operation of particle detectors at higher counting rates is required in a high-energy physics experiment. To satisfy this requirement, the scintillators used in a particle detector need to have a short fluorescence lifetime, which enables fast time response. For this purpose, we have measured fluorescence spectra and decay curves for plastic scintillators used in the J-PARC E14 KOTO experiment [1], commercially available recycled resin plates, and inorganic crystals. The fluorescence decay curves were measured by using light pulses from visible to vacuum ultraviolet under single bunch operation, which ensures a time-correlated single-photon counting method.

The top of Fig. 1 shows the decay curve of a plastic scintillator EJ-200 for the 430 nm band under excitation at 400 nm, and the bottom of Fig. 1 shows for the 420 nm band under excitation at 20 nm. They were measured at room temperature. The blue lines indicate experimental data. Lifetimes were analyzed by using the data analysis framework ROOT [2].

We assumed that the obtained decay curves are fitted with the formula

$$I(t) = \int_{-\infty}^{\infty} P(t')\theta(t' - T_0)G(t - t') dt' + B,$$

where

$$P(t) = \sum_{i=1}^n A_i \exp\left(-\frac{t}{\tau_i}\right),$$

($n = 1, 2, 3$ and $A_1 = 1$)

and

$$G(t - t') = \sum_{i=1}^m C_i \exp\left(-\frac{(t - t' - \mu_i)^2}{2\sigma_i^2}\right).$$

($m = 1, 2$)

$I(t)$ represents the observed decay curve, and $P(t)$ represents the true fluorescence decay curve. If the true decay curve is composed of multiple components, it is described as the linear combination of exponential decay functions with the parameters of lifetime τ_i and initial intensity A_i . $\theta(t' - T_0)$ is a step function to decide the time origin T_0 . $G(t - t')$ represents the resolution of the measurement system, the time structure of the beam, and so on, and is given by a single gaussian or a sum of two gaussians. B is a background constant that has a role in increasing a baseline. Red lines are the fitting curves which reproduce the experimental data.

We carried out the lifetime analysis for a plastic scintillator Scintirex [3] in the same method. The top of Fig. 2 shows the decay curve of Scintirex for the 436 nm band under excitation at 265 nm, and the

bottom of Fig. 2 shows for the 430 nm band under excitation at 20 nm. The fitting curves reproduce the experimental data. The fluorescence lifetimes of EJ-200 and Scintirex, determined from our analysis, are summarized in Table 1.

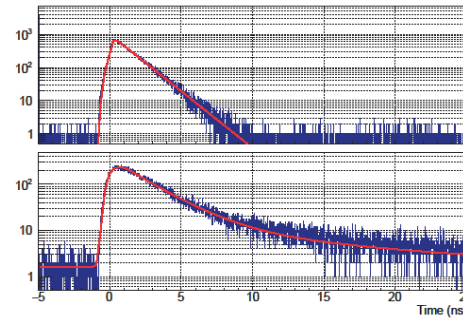


Fig. 1. Decay curve of EJ-200 measured at room temperature under excitation at 400 nm (top) and 20 nm (bottom). The former and latter are obtained for the 430 and 420 nm photoluminescence band.

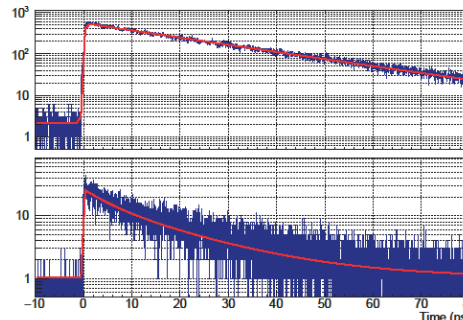


Fig. 2. Decay curve of Scintirex measured at room temperature under excitation at 265 nm (top) and 20 nm (bottom). The former and latter are obtained for the 436 and 430 nm photoluminescence band.

Table 1. Fluorescence lifetimes of EJ-200 and Scintirex, determined from our data analysis.

Sample	λ_{EX} [nm]	λ_{EM} [nm]	τ_1 [ns] (Ratio)	τ_2 [ns] (Ratio)
EJ-200	400	430	1.27±0.00	-
	20	420	2.25±0.00 (82.5 %)	10.56±0.22 (17.5 %)
Scintirex	265	436	24.79±0.08	-
	20	430	16.89±0.38 (83.3 %)	4.92±0.03 (16.7 %)

[1] J. Comfort *et al.*, Proposal for $K_L \rightarrow \pi^0 \nu \bar{\nu}$ Experiment at J-PARC (2006).

[2] R. Brun and F. Rademakers, Nucl. Instrum. Methods Phys. Res. A **389** (1997) 81.

[3] H. Nakamura *et al.*, Europhys. Lett. **95** (2011) 22001.

BL3B

Thermoluminescence of Yttrium Aluminum Garnet (YAG) Crystals Grown by Core Heating Method and Micro-pulling Down Method

Y. Kurashima¹, S. Kurosawa², R. Murakami³, A. Yamaji¹, K. Kamada^{2,3}, M. Yoshino¹, S. Tomida², H. Sato², Y. Yokota², Y. Ohashi² and A. Yoshikawa^{1,2,3}

¹Institute for Materials Research, Tohoku University, Sendai 980-8577, Japan

²New Industry Creation Hatchery Center, Tohoku University, Sendai 980-8579, Japan

³C&A Corporation, Sendai 980-0811, Japan

Scintillators are used in medical imaging such as Positron Emission Tomography (PET). Gamma-ray stopping power is one of the important scintillation properties for the PET camera and other gamma-ray detectors. Gamma-ray stopping power is proportional to $(Z_{eff})^a$, where Z_{eff} denotes effective atomic number and $a=4-5$. Hf-based materials like Ce-doped SrHfO₃[1] are attractive scintillation materials with high gamma-ray stopping power due to high density and high effective atomic number.

However, Growth of such materials by the conventional melt-growth methods with crucibles like micro-pulling down (μ -PD) method[2] are hard technique, because the melting points of Hf-based materials are typically higher than softening and melting point of the crucibles. The softening and melting point of Ir, for instance, 2000 °C and 2447 °C, respectively, while the melting temperature of SrHfO₃ is 2730 °C.

Thus, we have developed a novel crystal growth method to search novel materials with higher melting point than the melting point of the crucibles, and this method is named “Core Heating (CH) method” using electric arc or other heat source. Since, the scintillation properties of crystals grown by the CH method have not been evaluated yet, and we need to confirm the feasibility of CH method as a material search method.

To compare the growth method, we compared the scintillation properties for $(Y_{0.99}Ce_{0.01})_3Al_5O_{12}$ (Ce:YAG), because the melting point of Ce:YAG is 1940 °C and the conventional melt-growth is available. Ce:YAG crystals were grown by the CH and μ -PD method. The samples grown by CH method (CH sample) and μ -PD method (μ -PD sample) were cut and polished. If the scintillation and optical properties for CH samples are similar to those for the μ -PD sample, the CH method is judged to be a useful technique as a material search method.

We found some optical and scintillation properties such as emission wavelength, transmittance, light output excited by gamma-ray for the CH sample were the same level as those for μ -PD sample. Here, the detail of the results is reported in other papers. However, only scintillation decay time of the CH sample was different from that of the μ -PD sample. This result indicated that the CH sample has different trap sites, defects from the μ -PD sample. Therefore, we measured thermoluminescence (TL) spectra and TL glow curve to compare the trap sites. Measurement

of TL spectra and TL glow curves were performed at the beam line BL3B of UVSOR facility. The sample was irradiated with 165-nm photons for 10 min at 7 K. After we check no after-glow emission with a charge-coupled device (CCD, Roper Scientific, SPEC-10) attached to a polychromator (Acton Research Corporation, spectrapro-300i), the sample was heated up to 300 K with a heat rate of approximately 4 K/min. During the heating, the TL emission spectra were observed with the CCD.

Figure 1 shows TL glow curves of CH and μ -PD samples. The results of TL glow curves indicated no differences of number of traps and their depths were observed clearly between the CH and μ -PD samples. Therefore, such we found such trap sites are not the factor to change the decays.

In this time, the TL glow curves up to 300 K was measured, and we observed relatively shallow traps. On the other hand, deep traps observing the glow curves over 300 K might be related to be the decay-time deference, or other defects are also the candidates to make the decay time slower. As future works, we evaluate and discuss such factors.

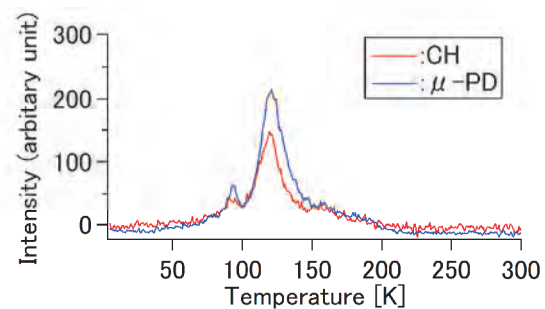


Fig. 1. TL glow curves of CH sample and μ -PD sample.

[1] S. Kurosawa, J. Pejchal, S. Wakahara, Y. Yokota and A. Yoshikawa, *Radiat. Meas.* **56** (2013) 155.

[2] A. Yoshikawa, M. Nikl, G. Boulon and T. Fukuda, *Opt. Mater. (Amst)*. **30** (2007) 6.

BL3B

Optical Properties of a $\text{Ce}_2\text{Si}_2\text{O}_7$ Single Crystal Using BL3B of the UVSOR Facility

T. Horiai¹, S. Kurosawa², A. Yamaji¹, S. Kodama¹, S. Yamato¹, Y. Kurashima¹, M. Yoshino¹, S. Toyoda², H. Sato², Y. Ohashi², K. Kamada^{2,3}, Y. Yokota² and A. Yoshikawa^{1,2,3}

¹Institute for Materials Research, Tohoku University, Sendai 980-8577, Japan

²New Industry Creation Hatchery Center, Tohoku University, Sendai 980-8579, Japan

³C&A Corporation, Sendai 980-0811 Japan

Scintillators convert energy of ionizing radiation into ultra-violet or visible light. When combined with suitable photodetectors such as a photomultiplier tube (PMT), scintillators are used in radiation detectors. Recently, Ce-doped pyrosilicate type crystals, $\text{Ce:RE}_2\text{Si}_2\text{O}_7$ (RE = rare-earth), have been studied, and Ce-doped $(\text{Gd,L a})_2\text{Si}_2\text{O}_7$ (Ce:La-GPS) has been reported to have a high light yield ($\sim 42,000$ photons/MeV), relatively short decay time (~ 63 ns), good energy resolution ($\sim 5.0\%$, 662 keV, FWHM) and shows a good temperature stability of light output up to 150 °C [1-3].

$\text{Ce}_2\text{Si}_2\text{O}_7$ nanocrystals and films were found that the emission peaks were located around 358 nm, which well matches the wavelength sensitivity of a typical PMT [4-6]. In addition, the internal quantum efficiency of the $\text{Ce}_2\text{Si}_2\text{O}_7$ was determined to be approximately 37 % at room temperature. Therefore, the $\text{Ce}_2\text{Si}_2\text{O}_7$ is also expected to have good scintillation properties. Thus, in this study, we tried to grow a relatively large mm-scale $\text{Ce}_2\text{Si}_2\text{O}_7$ single crystal, and estimated the optical properties.

We prepared the $\text{Ce}_2\text{Si}_2\text{O}_7$ single crystal using micro-pulling-down method. As starting materials, we used CeO_2 and SiO_2 powders the purities of which were at least 99.99 %. After cutting and mirror polishing the sample to thickness of 1 mm, we measured the photoluminescence spectra with a spectrometer (FLS920, Edinburgh Instruments) consisting of a Xe lamp at room temperature. Moreover, the emission and excitation spectra at 7 K were measured using excitation photons at BL3B of UVSOR, and evaluated the optical properties independent of the lattice vibration. The sample was cooled down to 7 K with liquid helium.

Figure 1 shows the emission and excitation spectra of the $\text{Ce}_2\text{Si}_2\text{O}_7$ at room temperature and 7 K. The emission spectrum of the $\text{Ce}_2\text{Si}_2\text{O}_7$ at room temperature has a single peak around 380 nm, while the emission spectrum at 7 K has double peak of $5d_1-^2F_{5/2}$ (358 nm) and $5d_1-^2F_{7/2}$ (387 nm). The emission peak around 358 nm consisted with the result measured by Choi in Ref. 4. From the results of emission and excitation spectra of the $\text{Ce}_2\text{Si}_2\text{O}_7$ at room temperature and 7 K, the emission peak of $5d_1-^2F_{5/2}$ at room temperature was quenched by the self-absorption. Comparison with the emission spectrum of Ce-doped $\text{La}_2\text{Si}_2\text{O}_7$, which has the same space group as $\text{Ce}_2\text{Si}_2\text{O}_7$ (monoclinic, $P2_1/c$) in the previous study, the emission peak of $\text{Ce}_2\text{Si}_2\text{O}_7$ is shifted to longer wavelength [7]. Here, comparing the ionic

radii of Ce^{3+} and La^{3+} in the eight-coordinate sites, the ionic radii are 1.143 and 1.160 Å, respectively [8]. Therefore, it was attributed to the stronger crystal field in $\text{Ce}_2\text{Si}_2\text{O}_7$ than in $\text{La}_2\text{Si}_2\text{O}_7$.

The $\text{Ce}^{3+} 4f-5d_x$ ($x=1-5$) transition peaks were observed in the excitation spectrum of the $\text{Ce}_2\text{Si}_2\text{O}_7$ at 7 K. The excitation peaks from $4f-5d_1$, $-5d_2$, $-5d_3$, $-5d_4$ and $-5d_5$ were positioned around 327, 292, 273, 254 and 228 nm, respectively. In addition, the excitation peak around 170 nm was observed, and determined to be the host excitation band peaking.

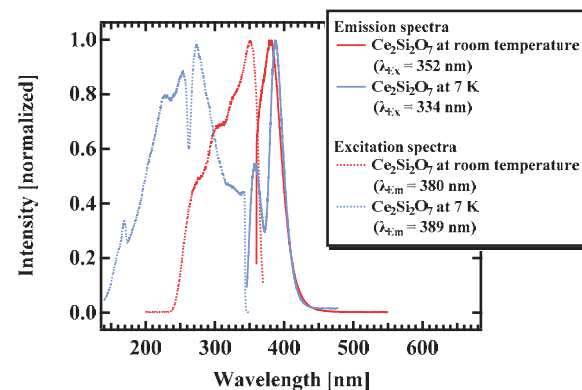


Fig. 1. Emission and excitation spectra of the $\text{Ce}_2\text{Si}_2\text{O}_7$ single crystal at room temperature and 7 K.

- [1] A. Suzuki, S. Kurosawa, A. Yoshikawa *et al.*, Appl. Phys. Express **5** (2012) 102601.
- [2] A. Yoshikawa, S. Kurosawa *et al.*, Cryst. Growth Des. **15** (2015) 1642.
- [3] S. Kurosawa, A. Yoshikawa *et al.*, Nucl. Instruments Methods Phys. Res. Sect. A **772** (2015) 72.
- [4] W.C. Choi *et al.*, Appl. Phys. Lett. **75** (1999) 2389.
- [5] L. Li *et al.*, Sci. Rep. **5** (2015) 1.
- [6] L. Kępiński *et al.*, J. Alloys Compd. **341** (2002) 203.
- [7] Q. Wei *et al.*, Materials Letters **126** (2014) 178.
- [8] R.D. Shannon, Acta. Cryst. **A32** (1976) 751.

BL3B

Low-temperature Photoluminescence Properties of Rb_2HfI_6

S. Kodama¹, S. Kurosawa², A. Yamaji¹, M. Yoshino¹, S. Toyoda², H. Sato²,
Y. Ohashi¹, K. Kamada^{2,3}, Y. Yokota² and A. Yoshikawa^{1,2,3}

¹Institute for Materials Research, Tohoku University, Sendai 980-8577, Japan

²New Industry Creation Hatchery Center, Tohoku University, Sendai 980-8579, Japan

³C&A Corporation, Sendai 980-0811 Japan

Rb_2HfI_6 has been developed as a novel red-emitting scintillator as a K_2PtCl_6 -type compound [1]. By substituting Rb into Cs, the scintillation emission peak of Rb_2HfI_6 shifted towards longer wavelength than Cs_2HfI_6 , and reached ~ 725 nm. Rb_2HfI_6 has a scintillation light output of $\sim 40,000$ photons/MeV, and such red-emission scintillator with a high light output can be used for a remote scintillation detector coupled with an optical fiber [2]. The mechanism of shift of emission wavelength has been still unclear, thus we evaluated the fundamental photoluminescence properties of Rb_2HfI_6 . We measured the low-temperature photoluminescence excitation (PLE) and emission (PL) spectra in order to determine the fundamental luminescence properties of Rb_2HfI_6 .

A single-crystalline Rb_2HfI_6 specimen was synthesized by the vertical Bridgman growth method in our laboratory from 99 %-pure HfI_4 and 99.9 %-pure RbI powders. We measured the PLE-PL spectra at 8 K in BL3B. As photo-detectors for PLE measurement, photomultiplier tubes (PMTs) (Hamamatsu K.K.) of R4220 and R636-10 were used for a blue-green and red region, respectively.

Figures 1 (a) and (b) illustrate the PL and PLE spectra of Rb_2HfI_6 at 8 K, respectively. The excitation and emission wavelengths were indicated as λ_{ex} and λ_{em} , respectively. Rb_2HfI_6 had three PLE-PL bands as follows: the blue band (λ_{ex} : 215 nm and λ_{em} : 440 nm), green band (λ_{ex} : 335 nm and λ_{em} : 590 nm) and red band (λ_{ex} : 455 nm and λ_{em} : 725 nm). The green and red bands were reported also in the case of Cs_2HfI_6 at 8 K [3], and in addition, Rb_2HfI_6 was identified to have the blue band whose λ_{ex} and λ_{em} were similar to the room temperature emission of Rb_2HfCl_6 [4]. The green band had a highest intensity, approximately 3 times higher than the red band, while only red-band emission was observed in the X-ray radioluminescence spectra at room temperature [1]. Although all emission bands had broad and single peaked spectra, PLE spectra of three bands had several excitation peaks, for example, ~ 180 nm and ~ 260 nm for blue band, ~ 335 nm and ~ 400 nm for green band. For the red band, an intense excitation peak was confirmed at ~ 455 nm, additionally a small peak at ~ 520 nm was also observed.

The splitting of the room temperature emission at low temperature was reported in the self-trapped exciton (STE) luminescence of CsI [5]. We confirmed that Rb_2HfI_6 had three photoluminescence bands at 8 K while the room temperature emission was the single band. Thus, the obtained results in this study implies that the emission origin of Rb_2HfI_6 was passively the

STE. For future works, the temperature dependence of each PLE-PL band should be studied to determine the emission mechanism.

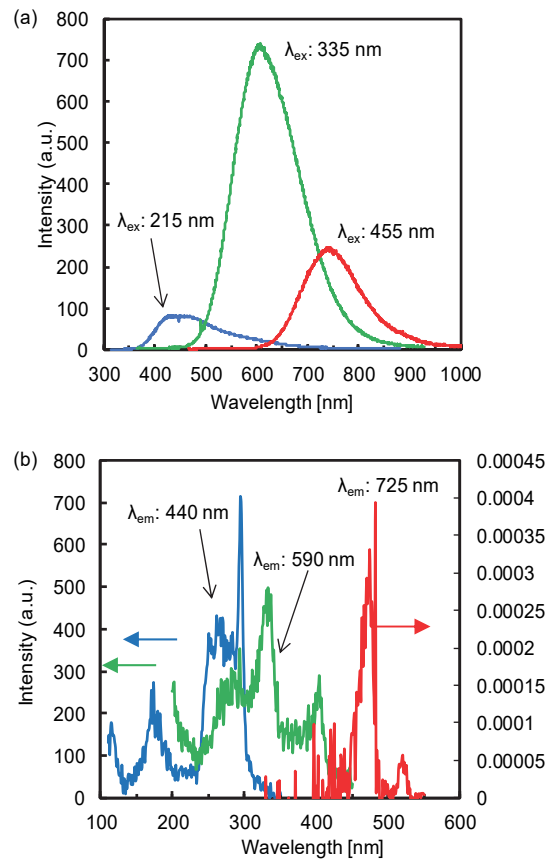


Fig. 1 (a) PL and (b) PLE spectra of Rb_2HfI_6 at 8 K. The PMTs of PLE spectra measurement of the red band ($\lambda_{\text{em}} = 725$ nm) were R636-10, and others were R4220.

[1] S. Kodama *et al.*, IEEE Trans. Nucl. Sci. (2020) in print.

[2] S. Kodama *et al.*, Appl. Phys. Express **13** (2020) 047002.

[3] S. Kodama *et al.*, UVSOR Activity Report 2018 **46** (2019) 62.

[4] K. Saeki *et al.*, J. J. Appl. Phys. **55** (2016) 110311.

[5] H. Nishimura *et al.*, Phys. Rev. B **51** (1995) 2167.

BL3B

Temperature Dependence of PL Spectra of *p*-terphenyl at 6-300 K

S. Yamato¹, S. Kurosawa², A. Yamaji¹, M. Yoshino¹, H. Sato²,
Y. Ohashi², K. Kamada^{2,3}, Y. Yokota² and A. Yoshikawa^{1,2,3}

¹Institute for Materials Research (IMR), Tohoku University, Sendai 980-8577, Japan

²New Industry Creation Hatchery Center (NICHe), Tohoku University, Sendai 980-8579, Japan

³C&A Corporation, Sendai 980-0811, Japan.

Neutron detectors can be used in several fields such as neutron diffraction for crystal structure, fusion physics [1,2]. Here, nuclear fusion technology is expected as next effective energy generation technology. In fusion reactors, neutrons are emitted from nuclear fusion reactions, and the monitoring these particles is an important technology to control fusion reactors and generate energy effectively.

Among several nuclei, the neutron cross section of hydrogen nucleus is the largest in higher energy range. ¹H has relatively higher cross section for the fast neutron than other materials. We focused on organic scintillators which contains many ¹H and have low detection efficiency for gamma rays as background noise.

Although the neutron detectors in fusion reactors can be exposed on higher temperature than 373 K, conventional organic scintillators cannot be used at high temperature. Plastic scintillators melt at around 343 K. Liquids evaporate at high temperature and are difficult to handle. Even crystals, only low-melting-point materials were developed. As a first step, we aimed to develop the organic scintillation crystals for such applications at over 373 K.

We grew the pure *p*-terphenyl crystal by the self-seeding vertical Bridgman method using an enclosed chamber [3]. Pulling down rate for growth was ~1 mm/h. The melting point of *p*-terphenyl is 485 K.

We measured the photoluminescence (PL) emission spectra of the samples under 13-300 K at the beamline BL3B of UVSOR Synchrotron Facility. The excitation and emission spectra of *p*-terphenyl are shown in Fig. 1 and Fig. 2, respectively. The excitation spectra were recorded with a cut filter for the shorter wavelength than 370 nm. The emission spectra were recorded for the *p*-terphenyl crystal excited by 280 nm photons.

In Fig. 1, absorption edge around 340 – 360 nm has been monotonically shifted to the lower energy side as the temperature rose, and the emission peaks of 375 and 390 nm were observed for *p*-terphenyl at 300 K (Fig. 2). The shapes of the spectra for *p*-terphenyl changed significantly between 300 K and others (200 K and less than 200 K), and relatively sharp peaks around 350 nm were observed at except 300 K. This is because of structural phase transition at 193.5 K by twisting in a molecule [4,5].

As future works, we study on the relationship between these results and temperature dependence of photo-luminescence decay time.

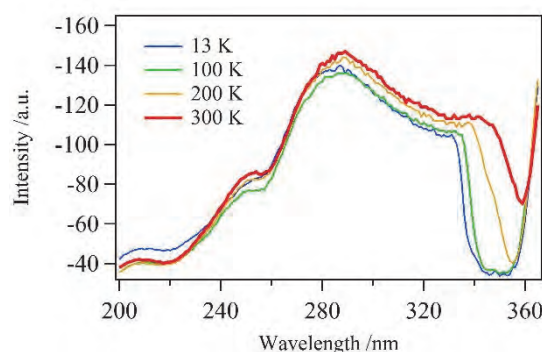


Fig. 1. Excitation spectra of *p*-terphenyl crystal at 13-300 K.

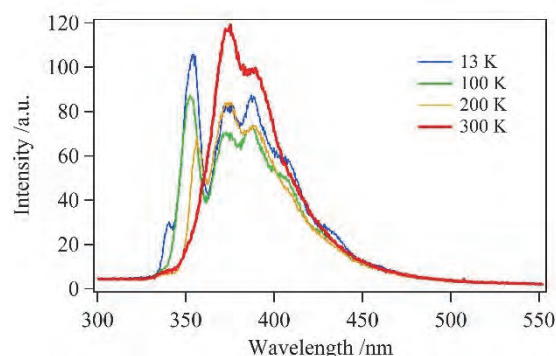


Fig. 2. Emission spectra of *p*-terphenyl crystal excited by 280 nm photons at 13-300 K.

- [1] H. K. Lee *et al.*, *J. Supercond. Novel Magn.* **31** (2018) 1677.
- [2] Y. K. Kim *et al.*, *J. Instrum.* **7** (2012) C06013.
- [3] A. Arulchakkaravarthi *et al.*, *J. Crystal Growth* **234** (2002) 159.
- [4] Y. Yamamura *et al.*, *J. Phys. Condens. Matter* **10 15** (1998) 3359.
- [5] Hervé Cailleau *et al.*, *Faraday Discuss. Chem. Soc.* **69** (1980) 7.

BL3B

Composition Dependence of 4f-4f Emission Spectra in Pr:SrZr_{1-x}Ti_xO₃

M. Yoshino, T. Kuyama and J. Sugiyama

Graduate School of Engineering, Nagoya University, Nagoya 464-8603, Japan

In this study, the excitation spectra and emission spectra of Pr³⁺ in SrZr_{1-x}Ti_xO₃ crystal have been measured and changes in the spectra with composition and temperature are examined.

The excitation spectra in $x = 0.6$ sample are shown in Fig. 1. The rising energy in excitation spectra is close to the band gap energy estimated from diffuse reflectance spectra. This is also the case in other composition. In order to excite host oxides, higher energies than band gap are selected for excitation. Fig. 2 shows the emission spectrum in $x = 0.6$ sample at 350 nm excitation. The sharp peaks around 500 nm (Greenish-blue) and 600-650 nm (Red) originate from 4f-4f transitions of Pr³⁺. The intensity ratios $R/(R+G)$ of Red emission (R) to sum of Red and Greenish-blue emission (G) in Pr:SrZr_{1-x}Ti_xO₃ are shown in Fig. 3. It is found that the ratios are large in the intermediate composition. As shown in Fig. 4 and Fig. 5, changes in the intensities of emission in $x = 0.6$ with temperature are different between excitation energy. Thermally activated process is included in 280 nm excitation.

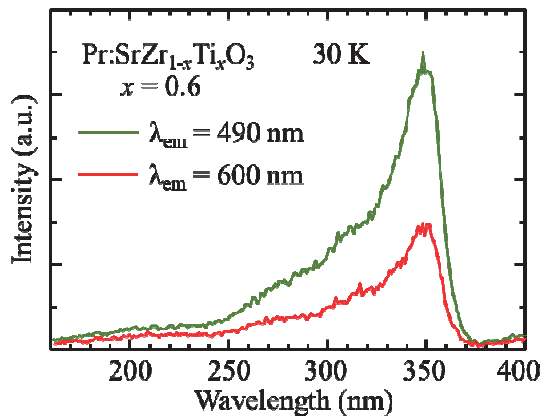


Fig. 1. Excitation spectra of Pr:SrZr_{0.4}Ti_{0.6}O₃ (30 K).

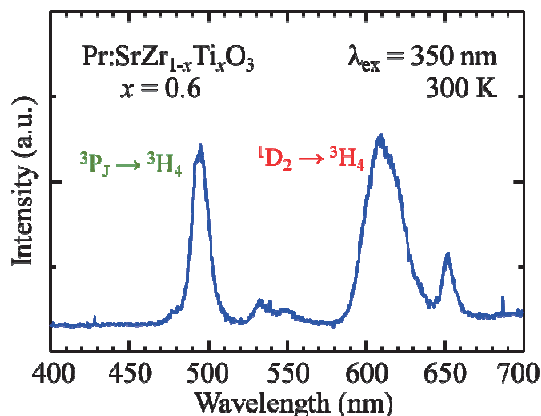


Fig. 2. Emission spectrum of Pr:SrZr_{0.4}Ti_{0.6}O₃ ($\lambda_{em} = 350$ nm, 300 K).

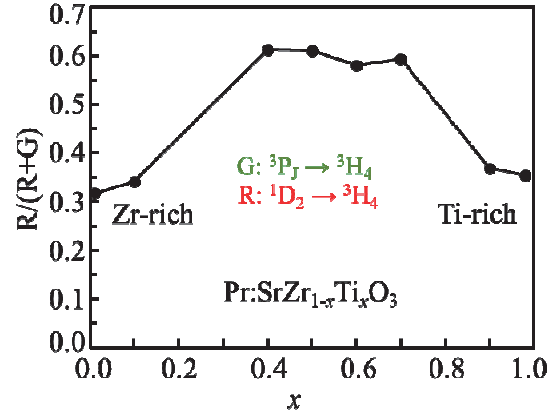


Fig. 3. The intensity ratios $R/(R+G)$ of Red emission (R) to sum of Red and Greenish-blue emission (G) in Pr:SrZr_{1-x}Ti_xO₃ (300 K).

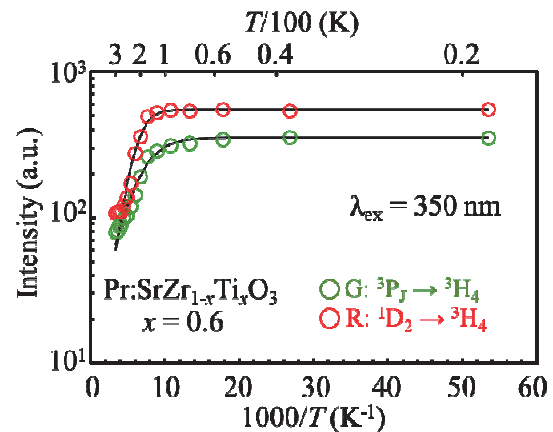


Fig. 4. Change in the intensities of Red emission and Greenish blue emission with temperature in Pr:SrZr_{0.4}Ti_{0.6}O₃ ($\lambda_{em} = 350$ nm).

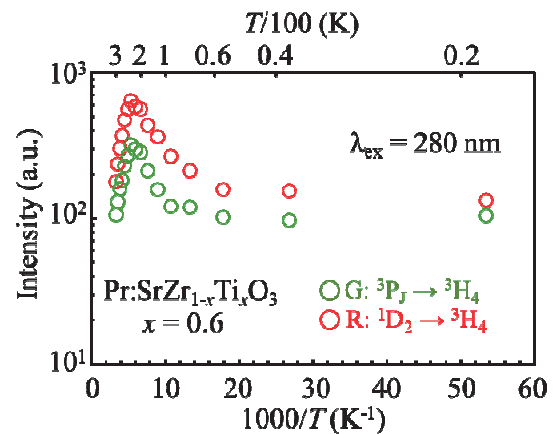


Fig. 5. Change in the intensities of Red emission and Greenish blue emission with temperature in Pr:SrZr_{0.4}Ti_{0.6}O₃ ($\lambda_{em} = 280$ nm).

III-2

BL3B

Excitation Process of Ce^{3+} Ions in La Doped $\text{Gd}_2\text{Si}_2\text{O}_7$ Crystals Caused by VUV Photons

R. Tarukawa¹, M. Kitaura¹, S. Kurosawa², T. Makino³ and A. Ohnishi¹¹Faculty of Science, Yamagata University, Yamagata 990-8560, Japan²New Industry Creation Hatchery Center, Tohoku University, Sendai 980-8579, Japan³Department of Electrical and Electronics Engineering, University of Fukui, Fukui 910-8507, Japan

Multiplication of electronic excitations (MEEs) in wide-gap oxides takes place when the energy of excitation photon exceeds several times of the band-gap energy. The fundamental process of MEEs is based on inelastic scattering of valence electrons with hot photoelectrons. On the other hand, the excitation process of luminescent ions doped in wide-gap oxides by vacuum ultraviolet (VUV) photons is complex, because a number of relaxation processes compete under excitation [1]. Studies on such VUV excitation processes of luminescent ions give us complementary information on impact excitation of luminescent ions by hot carriers, which is important in both sides of fundamental and applied physics.

Ce-doped and La-admixed gadolinium pyrosilicate ($(\text{La,Gd})_2\text{Si}_2\text{O}_7\text{:Ce}$, La-GPS:Ce) is known as an inorganic scintillator. Luminescence properties of La-GPS:Ce crystals have been investigated under excitation with VUV photons [2]. However, the process of MEEs in La-GPS has not yet been cleared. Furthermore, the excitation of Ce^{3+} ions by VUV photons still remains unknown.

In the present study, we have measured emission and excitation spectra of an undoped La-GPS and La-GPS:Ce crystals at 10 K. Experiment was performed at the BL3B beamline of UVSOR in the Institute for Molecular Science (IMS). The emission spectrum of an undoped La-GPS crystal exhibited an emission band peaking at 316 nm. This band is assigned to Gd^{3+} 4f-4f transition. The excitation spectrum for the 316 nm band is shown in Fig. 1 (a). In the region below 7.5 eV, one can see sharp peaks due to Gd^{3+} 4f-4f transitions. The stepwise structures are found around 14 and 20 eV. The band-gap energy was reported to be 6.6-6.8 eV. The former and latter are close to twice and treble of the band-gap energy, respectively. The fundamental process of MEEs in wide-gap oxides has to satisfy the conservation laws of energy and momentum. When hot photoelectrons and photoholes are created by VUV photons, the threshold energy for MEEs exceeds the twice of the band-gap energy [1]. Especially, it is expected that the threshold energy reaches the treble of the band-gap energy for La-GPS with the wide valence band. It is, therefore, likely that the MEEs in La-GPS occurs in the region above 20 eV.

The excitation spectrum of a La-GPS:Ce crystal showed an emission band at around 393 nm at 10 K. This band is assigned to the Ce^{3+} 5d-4f transition. The excitation spectrum for the 393 nm band is shown in Fig.

1 (b). In the region below 7.5 eV, one can see broad bands due to Ce^{3+} 4f-5d transitions. No sharp peaks are found in Fig. 1(b). This fact suggests the $\text{Gd}^{3+} \rightarrow \text{Ce}^{3+}$ energy transfer does not occur in La-GPS:Ce, and is contrast with $\text{Gd}_3\text{Al}_2\text{Ga}_3\text{O}_{12}\text{:Ce}$ (GAGG:Ce) [3]. In the region above 7.5 eV, the excitation spectra in Figs. 1(a) and 1(b) are almost the same with each other. This fact explains as follows. Hot photoelectrons and photoholes created by VUV photons relax into the conduction band minimum and valence band maximum, respectively. They are immediately captured by Ce^{3+} ions, and form the excited state of Ce^{3+} ions. Consequently, it is reasonable that the excitation spectrum for the 393 nm band reflects that for the 316 nm band.

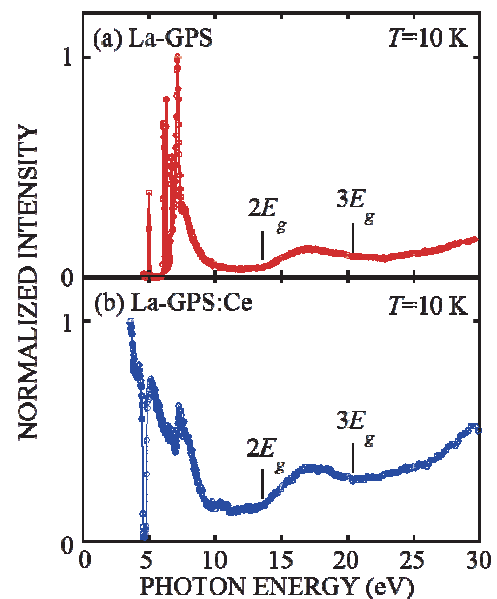


Fig. 1. (a): Excitation spectrum for the 316 nm band of an undoped La-GPS crystal. (b): Excitation spectrum for the 393 nm band of a La-GPS:Ce crystal. These spectra were measured at 10 K.

- [1] M. Kitaura *et al.*, *J. Lumin.* **172** (2016) 243.
 [2] M. Koshimizu *et al.*, *J. Rare Earths* **34** (2016) 782.
 [3] M. Kitaura *et al.*, *J. Appl. Phys.* **115** (2014) 083517.

BL3B

Dynamical Behaviors of the Localized Exciton in NaCl:I⁻ Crystals

T. Kawai

Graduate School of Science, Osaka Prefecture University, Sakai 599-8531, Japan

When alkali chloride crystals are doped with heavier hetero-halogen ions, the absorption bands due to the heavier hetero-halogen ions are observed in the lower energy region than the fundamental absorption edge of the host crystals. The photo-excitation on the absorption bands induces various kinds of relaxed excitons localized to the heavier hetero-halogen ions and the luminescence bands called BG, B, UV, and NE are observed [1-3]. Though the BG, B, UV, and NE luminescence bands are observed in many alkali chloride crystals doped with heavier hetero-halogen ions, NaCl:I⁻ crystals exhibit only the NE luminescence band in the wide temperature range from a low temperature to room temperature. The NE luminescence is attributed to the radiative transition from the relaxed excited states of the one-center-type relaxed exciton, which consists of a hole localized on a hetero-halogen anion and a bound electron. We have investigated the dynamical behaviors of the one-center-type relaxed exciton in the NaCl:I⁻ crystals at the BL3B line of UVSOR.

In the NaCl:I⁻ crystals, the absorption band due to the localized exciton and the NE luminescence are observed around 6.95 and 5.7 eV, respectively, as shown in Fig. 1. Figure 2 shows the temporal profiles of the NE luminescence under various excitation energies around the absorption band. Under the excitation near peak energy of the absorption band, the NE luminescence exhibits the almost single exponential decay profile. On the other hand, it seems that there are two exponential components under the excitation at the off-peak energy of the absorption band. The decay time constants of the fast and slow components are about 2.6 ns and 120 ns, respectively. The decay time constant of 2.6 ns is almost equal to that of the fast component of the intrinsic type I self-trapped exciton (STE) luminescence in pure NaCl crystals [4]. The intrinsic type I STE exhibits the broad luminescence band around 5.2 eV and the luminescence overlaps with the NE luminescence band.

The exciting light with the off-peak energy penetrates deeper into the crystal than that with the peak energy of the absorption band. Thus, the excitation at the off-peak energy of the absorption band would create the one-center-type relaxed exciton inside the crystals. Then, the intrinsic type I STE may be formed from the one-center-type relaxed exciton. Further studies will probably be necessary.

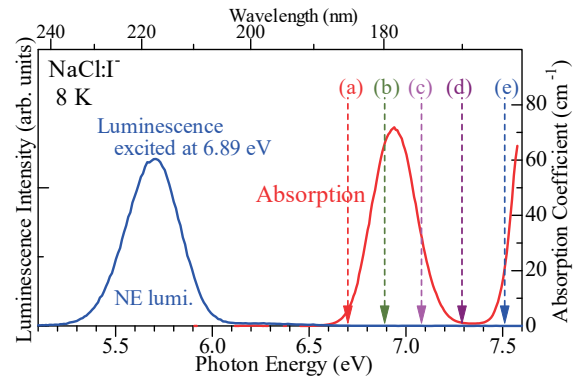


Fig. 1. Luminescence and absorption spectra of NaCl:I⁻ crystals at 8 K.

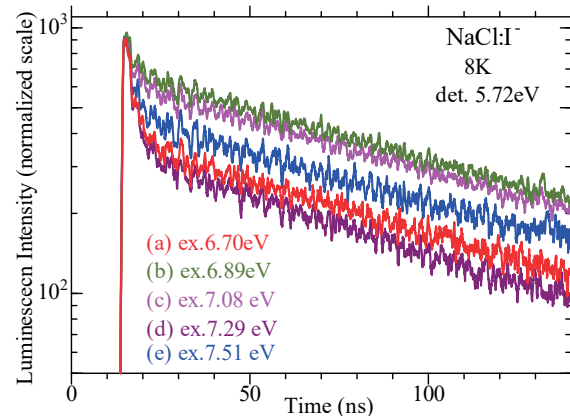


Fig. 2. Temporal profiles of the NE Luminescence under various excitation energies around the absorption band at 8 K. The excitation energies are shown by the down arrows in Fig. 1.

- [1] T. Higashimura *et al.*, J. Phys. Soc. Jpn. **53** (1984) 1878.
- [2] K. Kan'no *et al.*, J. Phys. Soc. Jpn. **55** (1986) 2443.
- [3] I. Akimoto *et al.*, Phys. Status Solidi C **6** (2009) 342.
- [4] T. Matsumoto *et al.*, J. Phys. Soc. Jpn. **61** (1992) 4229.

BL3B

VUV Spectroscopy of Magnesium Oxide Treated with Hydrogen Reduction

E. Kobayashi¹, K. K. Okudaira², M. Imamura³, K. K. Bando³, H. Kakiuchida³,
S. Yoshioka⁴ and O. Takahashi⁵

¹Kyushu Synchrotron Light Research Center, Tosu 841-0005, Japan

²Chiba University, Chiba, Chiba 263-8522, Japan

³National Institute of Advanced Industrial Science and Technology, Tsukuba 305-8565, Japan

⁴Graduate School of Engineering, Kyushu University, Fukuoka 819-0395 Japan

⁵ Graduate School of Science, Hiroshima University, Higashi-Hiroshima 739-8526, Japan

Magnesium oxide (MgO) is a typical wide electronic band gap insulator and is used in devices such as optical, electrical and catalytic. Characteristics such as light transmission and thermal insulation are greatly affected by defects generated in the production process of crystals and thin films and practical materials. In compounds such as oxide, various types of defects such as point, line and planar defects exist, and the electronic state derived from the defect causes electrical, optical, or magnetic functions. For this reason, many point defects of metal oxides have been studied. MgO defects are generated by methods such as X-ray irradiation [1], UV irradiation [2], neutron scattering [3], electron beam irradiation [4,5], and heat treatment [6,7].

This study focused on magnesium oxide heated in a hydrogen atmosphere and the correlation between the amount of defects and optical properties was investigated using UV absorption spectroscopy. In addition, the plane orientation dependence of the MgO crystal was investigated.

The MgO (100) and MgO (111) were annealed at several temperatures at 473 K ~1173 K in a hydrogen atmosphere for 4 hours. The samples were gradually cooled to room temperature, exposed to the air, then introduced into a vacuum apparatus, and the spectrum was measured. UV spectra of MgO single crystal were measured at the BL3B of UVSOR in the Institute of Molecular Science.

Figure 1 shows UV spectra of MgO(100) and MgO(111). A distinct increase in absorption from 5.6 eV to 7.0 eV in MgO(100) was observed for the treated under hydrogen, compared to an untreated one. This result indicated that a new electronic state was formed in the conduction band due to the oxygen defect produced by the hydrogen reduction treatment, which made the band gap narrower. On the other hand, a decrease in absorption in MgO(111) was observed for the treated under hydrogen. This suggests that the interaction with hydrogen depends on the crystal plane. The spectrum changes because MgO (111) is an unstable polar surface, whereas MgO (100) is electrically neutral. The exact cause has been investigated using other techniques.

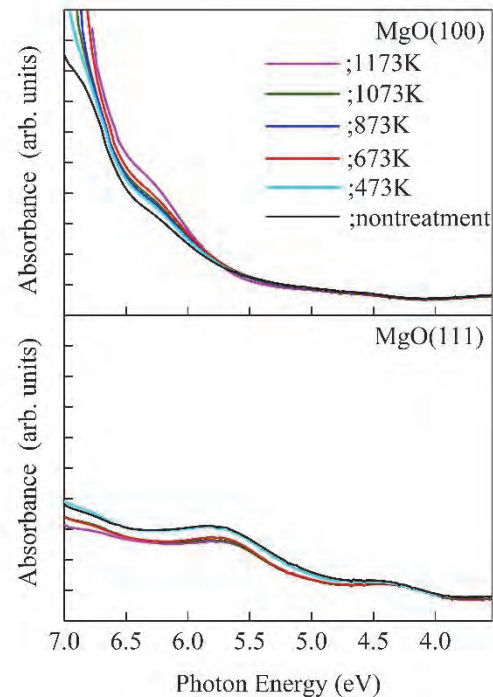


Fig. 1. UV spectra of MgO single crystal.

- [1] J. P. Molnar *et al.*, Phys. Rev. **79** (1950) 1015.
- [2] Y. Chen *et al.*, Phys. Rev. **182** (1968) 960.
- [3] H. R. Day, Phys. Rev. **91** (1953) 822.
- [4] V. E. Henrich *et al.*, Phys. Rev. B **22** (1980) 4764.
- [5] P. R. Underhill *et al.*, Solid State Commun. **43** (1982) 9.
- [6] M. Wu *et al.*, Phys. Rev. B **19** (1992) 12688.
- [7] L. A. Kappers *et al.*, Phys. Rev. B **1** (1970) 4151.

BL3B

Luminescence Characteristics of Cs₂BaCl₄

K. Takahashi¹, M. Koshimizu¹, Y. Fujimoto¹, T. Yanagida² and K. Asai¹

¹Department of Applied Chemistry, Graduate School of Engineering, Tohoku University, Sendai 980-8579, Japan

²Division of Materials Science, Nara Institute of Science and Technology, Ikoma 630-0192, Japan

Auger-free luminescence (AFL) is caused by the radiative transition of a valence electron to a core hole state. The transition is competitive with the Auger process, which is a much faster process, efficient AFL cannot be observed in many compounds. In other words, efficient AFL has been observed in limited compounds such as alkaline- or alkaline-earth fluorides or CsCl-based compounds.

AFL has been applied to fast scintillators owing to its fast decay. A representative one is BaF₂; however, CsCl-based compounds have an advantage of long emission wavelength appropriate for detection with a photomultiplier tube. Thus far, we have developed fast scintillators based on ternary CsCl-based compounds [1,2]. In this study, we developed fast scintillators based on Cs₂BaCl₄.

Crystal samples of Cs₂BaCl₄ were fabricated using a self-seeding solidification method and the Bridgman method. Powders of CsCl (99.99 %, Mitsuwa Chemical Co. Ltd., Japan) and BaCl₂ (99.9 %, Kojundo Chemical Laboratory Co Ltd., Japan) were mixed in a stoichiometric ratio. The mixed powders were poured into quartz ampoules and heated at 350 °C in vacuum for 1 day to remove adsorbed water. For the self-seeding solidification method, the quartz ampoule was set in a tubular furnace, and the furnace was heated to 950 °C for 12 h and subsequently cooled to room temperature over 72 h. For the Bridgman method, the ampoule was set in a Bridgman furnace. The temperatures of the upper and lower heaters in the furnace were set at 950 °C and 750 °C, respectively, during crystal growth, and the ampoules were lowered at a rate of 1.5 mm/h.

The luminescence properties were characterized with vacuum ultraviolet (VUV) light as an excitation source. Measurements were performed at BL7B for the steady state spectra and at BL3B for temporal profiles at the UVSOR Synchrotron Facility at the Institute for Molecular Science, Japan. Synchrotron radiation being monochromatized with a 3-m normal-incidence monochromator was used for the excitation. The luminescence spectra were measured at different excitation wavelengths, and the excitation spectra were obtained from the luminescence spectra. The luminescence temporal profiles were observed using a time-correlated single photon counting method. The single-bunch operation mode was used, and the period between successive pulses was 176 ns.

Figure 1 shows the luminescence spectra with VUV excitation at 150 nm, 180 nm, and 84 nm. For the excitation at 150 nm and 180 nm, the bands at 430 nm and 480 nm were observed, respectively. For the excitation at 84 nm which corresponds to the excitation

for the outermost core level of Cs, broad band at 450 nm was observed, but clear bands at 250–320 nm, which corresponds to the expected AFL wavelength, was not observed. Considering that the band gap energy of CsCl is 8.3 eV, that of Cs₂BaCl₄ is possibly located at the energy corresponding to 150–180 nm. Therefore, the bands at 430 nm and 480 nm can be attributed to STEs though it is required to clarify the band structure of Cs₂BaCl₄.

Figure 2 shows the excitation spectrum for the luminescence at 270 nm. A steep rise at approximately 87 nm was observed for the luminescence at 270 nm. This excitation spectrum was quite similar to those of CsCl-based compounds [2,3], and the result clearly indicates that Cs₂BaCl₄ exhibits AFL though clear bands were not observed in the photoluminescence spectrum with the excitation at 84 nm.

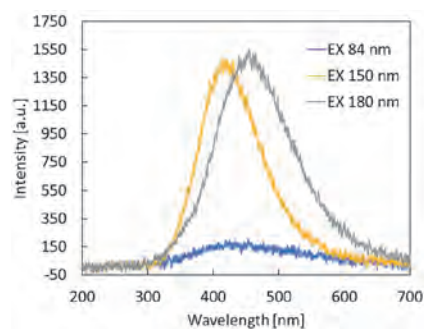


Fig. 1. Luminescence spectra of Cs₂BaCl₄ for the excitation at 84 nm, 150 nm, and 180 nm.

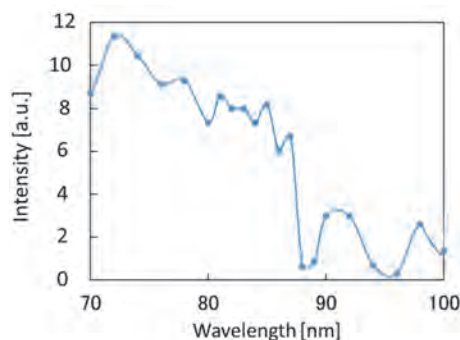


Fig. 2. Excitation spectra of Cs₂BaCl₄ for monitored wavelength of 270 nm.

[1] N. Yahaba *et al.*, Appl. Phys. Express **7** (2014) 062602.

[2] M. Koshimizu *et al.*, Opt. Mater. **36** (2014) 1930.

[3] A. Ohnishi *et al.*, J. Phys. Soc. Jpn. **72** (2003) 2400.

BL3B

Evaluation of Achromatic Vacuum-ultraviolet Lens

T. Shimizu, Y. Minami, K. Kuroda, K. Shinohara, D. Umeno and N. Sarukura
Institute of Laser Engineering, Osaka University, Suita 565-0875, Japan

Vacuum ultraviolet (VUV) has numerous scientific and technological applications including spectroscopy, environmental monitoring, surface micromachining, sterilization and so on. In the study of VUV materials, it has been found that fluoride materials can be applied as new VUV optics including lenses. For VUV lenses, the material must be transparent to the light in the VUV region, have chemical stability, have a high melting point, and be uniform and of good quality. In this study, an achromatic lens made of two materials was fabricated based on a design that minimizes chromatic aberration in the 150-300 nm range using fluoride crystals with high VUV transmittance.

A combination of LiCaF_6 and BaLiF_3 was used as materials for the convex and concave lenses of the VUV achromatic lens because it has the lowest chromatic aberration in combinations of fluoride crystals with high transmittance in the vacuum ultraviolet region. Chromatic aberration at 150 nm and 300 nm is corrected for in this design. In addition, since there is no lens adhesive that can transmit vacuum ultraviolet light, there is a gap between the convex and concave lenses, which is fixed by sandwiching them with a lens folder. The coating agent used for the anti-reflection coating, which suppresses reflections on the lens surface, is not applied because it cannot penetrate VUV light and may reduce the transmittance and degrade the vacuum due to vaporization.

The performance of VUV achromatic lenses is evaluated in the following three areas: transmittance, chromatic aberration, and focusing performance. In the first half of the year, measurements of transmittance were carried out using BL7B. The evaluation of chromatic aberration was carried out in the second half of the experiment using BL3B. The chromatic aberration is evaluated by measuring the focal length of the light in the range of 150 to 300 nm and comparing them. The results are shown in Fig. 1. The color of the lines indicates the difference in wavelength. Although the complete analysis is not yet complete, there is not much difference in the light-focusing trend for each wavelength.

From the experimental results, it was confirmed that the VUV achromatic lens is practical for the measurement system with a certain beam intensity. In addition, it was confirmed that the design policy of the previous study is useful for the design of achromatic lenses in the VUV region. In order to improve the performance, it is necessary to develop AR coating materials that suppress the reflected light and transmit vacuum ultraviolet light, and to improve the purity and uniformity of the lens materials.

In the future, a rigorous evaluation is required, and it is important to further increase the knowledge of achromatic lenses in the vacuum ultraviolet region. In addition, the development of an imaging spectrometer with a VUV achromatic lens is expected to be carried out in parallel for practical use.

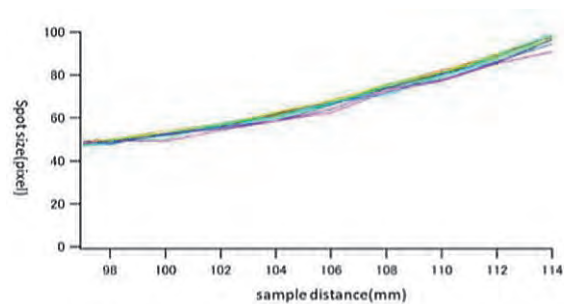


Fig. 1. Chromatic aberration measurement results.

- [1] K. Shimamura, H. Sato, A. Bensalah, H. Machida, N. Sarukura and T. Fukuda, *J. Alloys Compds.* **343** (2002) 204.
- [2] M. V. Luong, M. J. F. Empizo, M. Cadatal-Raduban, R. Arita, Y. Minami, T. Shimizu, N. Sarukura, H. Azechi, M. H. Pham, H. D. Nguyen, Y. Kawazoe, K. G. Steenbergen and P. Schwerdtfeger, *Opt. Mater.* **65** (2017) 15.
- [3] R. Arita, Y. Minami, M. Cadatal-Raduban, M. H. Pham, M. J. F. Empizo, M. V. Luong, T. Hori, M. Takabatake, K. Fukuda, K. Mori, K. Yamanoi, T. Shimizu, N. Sarukura, K. Fukuda, N. Kawaguchi, Y. Yokota and A. Yoshikawa, *Opt. Mater.* **47** (2015) 462.
- [4] T. Shimizu, M. V. Luong, M. Cadatal-Raduban, M. J. F. Empizo, K. Yamanoi, R. Arita, Y. Minami, N. Sarukura, N. Mitsuo, H. Azechi, M. H. Pham, H. D. Nguyen, K. Ichianagi, S. Nozawa, R. Fukaya, S. Adachi, K. G. Nakamura, K. Fukuda, Y. Kawazoe, K. G. Steenbergen and P. Schwerdtfeger, *Appl. Phys. Lett.* **110** (2017) 141902.
- [5] M. V. Luong, M. Cadatal-Raduban, M. J. F. Empizo, R. Arita, Y. Minami, T. Shimizu, N. Sarukura, H. Azechi, M. H. Pham, H. D. Nguyen and Y. Kawazoe, *Jpn. J. Appl. Phys.* **54** (2015) 122602.
- [6] K. Yamanoi, T. Murata, Y. Arikawa, T. Nakazato, M. Cadatal-Raduban, T. Shimizu, N. Sarukura, M. Nakai, T. Norimatsu, H. Nishimura, H. Azechi, S. Fujino, H. Yoshida, A. Yoshikawa, N. Satoh and H. Kan, *Opt. Mater.* **35** (2013) 1962.

BL3B

Electronic States and Charge Dynamics of $\text{Sm}_{1-x}\text{Ce}_x\text{S}$

Y. Yokoyama¹, H. Hasegawa¹, J. Shibutani¹, Y. Kadowaki¹, Y. Okamoto¹, H. S. Suzuki²,
K. Takehana³, Y. Imanaka³ and K. Takenaka¹

¹Department of Applied Physics, Nagoya University, Nagoya 464-8603, Japan

²The Institute of Solid State Physics, The University of Tokyo, Kashiwa 277-8581, Japan

³National Institute for Materials Science (NIMS), Tsukuba 305-0003, Japan

Samarium monosulfide (SmS), in which two electronic configurations ($(4f)^6$ and $(4f)^5(5d)^1$) of Sm are energetically competed, is known as a valence fluctuation materials. The electronic state of Sm undergoes transition to $(4f)^5(5d)^1$ by applying pressure and chemical doping, while the $(4f)^6$ state is stable under ordinary pressure and temperature condition [1]. It is promising to be applied to materials for negative thermal expansion (NTE) and actuators by controlling these electronic states [2], because this phenomenon is accompanied with a large volume change up to 10 %. To study changes in the electronic states due to the valence transition, we recently conducted systematic optical reflectivity measurements toward $\text{Sm}_{1-x}\text{Y}_x\text{S}$ single crystalline samples, covering wide energy and compositional region [3]. Consequently, it is clarified that a characteristic structure, which showed the changes in electronic states induced by the valence transition, became appeared in the optical spectra at Y composition of 0.28 [3].

In this study, to investigate the changes in the electronic states by the other dopant, we measured the optical reflectivity $R(\omega)$ spectra of $\text{Sm}_{1-x}\text{Ce}_x\text{S}$ single crystalline samples in the wide (from far-IR to vacuum-UV) energy regions. Normal incident reflectivity spectra were collected at 295 K by using a Fourier-type interferometer (0.005–1.6 eV) and a grating spectrometer (1–3 eV) installed with a microscope. For the measurements from visible to vacuum-UV region (2–30 eV), we used a synchrotron radiation at BL3B of UVSOR, Institute for Molecular Science. Then, optical conductivity $\sigma(\omega)$ was deduced from the $R(\omega)$ using the Kramers-Kronig relation.

Figure 1 shows the $R(\omega)$ spectra of $\text{Sm}_{1-x}\text{Ce}_x\text{S}$ taken at 295 K. The corresponding spectra of $\text{Sm}_{1-x}\text{Y}_x\text{S}$ [3] are shown in the right column for the comparison. As the Ce doping proceeds to $x = 0.20$, reflectivity edge moves to higher energy and the characteristic structure around 1 eV appears, in common with the Y-doped case. However, it seems that the spectral changes occur at lower Ce doping level comparing to the Y-doped case. The $\sigma(\omega)$ spectra (Fig. 2) show that the Ce doping also generates a significant structure in the IR region, which is not characterized by a simple Drude response, at lower dopant composition than the Y-doped case.

The recent works of the NTE function of the $\text{Sm}_{1-x}\text{R}_x\text{S}$ (R : rare-earth elements) reported the steep changes in the lattice parameter induced by the doping; $0.2 < x < 0.3$ for the Y-doping and $0.1 < x < 0.2$ for the Ce-doping

[2,4]. Considering these facts together with the present results, it is strongly suggested that the characteristic structure in the IR region of the $\sigma(\omega)$ spectra reflects the valence fluctuating states. The findings in the present study raise a new question: why the valence transition occurred at lower Ce composition level? To answer this question precisely, it is useful that the differences in the electronic states between Y and Ce are elucidated by other methods such as the photoelectron spectroscopy.

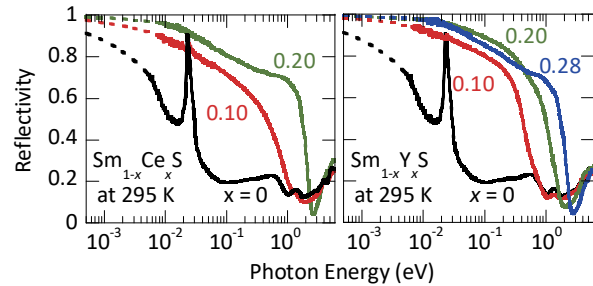


Fig. 1. Reflectivity spectra of $\text{Sm}_{1-x}\text{R}_x\text{S}$ ($R=\text{Ce}$ (left), Y (right) [3]) single crystallines at 295 K. Broken lines represents the Hagen-Rubens extrapolation.

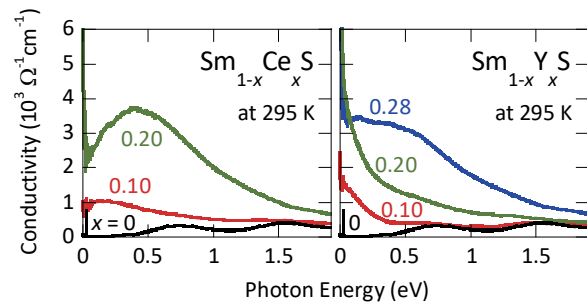


Fig. 2. Optical conductivity spectra of $\text{Sm}_{1-x}\text{R}_x\text{S}$ ($R=\text{Ce}$ (left), Y (right) [3]) at 295 K.

- [1] A. Jayaraman *et al.*, Phys. Rev. B **11** (1975) 2783.
- [2] K. Takenaka *et al.*, Sci. Rep. **9** (2019) 122.
- [3] Y. Yokoyama *et al.*, Phys. Rev. B **100** (2019) 245143.
- [4] D. Asai *et al.*, Appl. Phys. Lett. **114** (2019) 141902.

BL4U

Analysis of Lithium Insertion/Extraction Process in One-dimensional Single-crystalline Active Materials by Scanning Transmission X-ray Microscopy

E. Hosono^{1,2,3}, D. Asakura^{1,2}, H. Yuzawa⁴ and T. Ohigashi^{4,5}¹Research Institute for Energy Conservation, National Institute of Advanced Industrial Science and Technology, Tsukuba 305-8568, Japan²AIST-UTokyo Advanced Operando-Measurement Technology Open Innovation Laboratory (OPERANDO-OIL), National Institute of Advanced Industrial Science and Technology (AIST), Kashiwa 277-8565, Japan.³Global Zero Emission Research Center, National Institute of Advanced Industrial Science and Technology, Tsukuba 305-8568, Japan⁴UVSOR Synchrotron Facility, Institute for Molecular Science, Okazaki 444-8585, Japan⁵School of Physical Sciences, The Graduate University for Advanced Studies, SOKENDAI, Okazaki 444-8585, Japan

Innovative technologies for clean energy devices are desired for the realization of sustainable society by preventing global warming. Development of high-performance Li-ion batteries (LIBs) for electric vehicles and large-scale power storage in renewable energy power plants is attracting much attention.

We have studied the morphology control method of materials, because the properties of materials depend on crystal direction and facet of materials [1]. In addition, we have been studying the charge-discharge mechanism of LIBs. Nevertheless, there are many unsolved mechanisms in the research field of LIBs.

Soft X-ray spectroscopy is a powerful technique to understand the electronic structures of transition-metal oxides used for active materials of LIBs. Moreover, by using scanning transmission X-ray microscope (STXM), we can get the electronic structural information with special information. For the single-crystalline active materials of LIBs, position-dependent Li insertion/extraction reaction is expected to be observed by STXM. Especially, single-crystalline nanowire materials have diffusion paths with limited direction based on the crystal structure. In the case of $\text{LiFe}_x\text{Mn}_{1-x}\text{PO}_4$ single-crystalline nanowire materials, the diffusion path is limited to one direction.

Here, we exhibit a result of *ex situ* STXM for $\text{LiFe}_x\text{Mn}_{1-x}\text{PO}_4$ single-crystalline nanowire. Figure 1 shows the STXM image measured with an excitation energy of 700 eV. Nanowire image of $\text{LiFe}_x\text{Mn}_{1-x}\text{PO}_4$ is obtained by STXM. The Fe $L_{3,2}$ -edge absorption spectra of selected regions are shown in Fig. 2. Each spectrum is ascribed to Fe^{3+} state compared with previous X-ray absorption result [2]. Now, we are analyzing the Fe $L_{3,2}$ -edge, Mn $L_{3,2}$ -edge, and O K -edge results for the $\text{LiFe}_x\text{Mn}_{1-x}\text{PO}_4$.

In the near future, we will establish *operando* STXM measurement system.

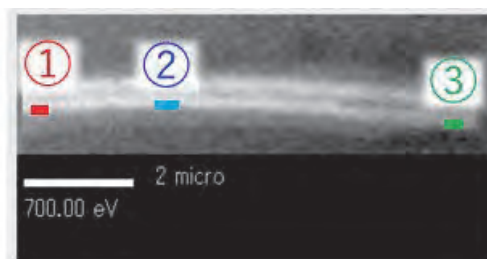


Fig. 1 A STXM image of the $\text{LiFe}_x\text{Mn}_{1-x}\text{PO}_4$ single-crystalline nanowire

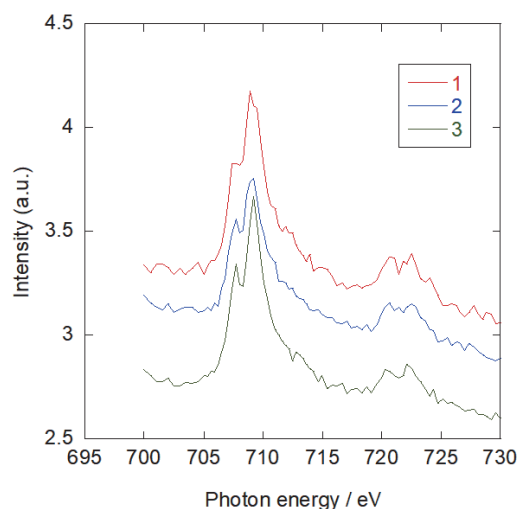


Fig. 2. Fe $L_{3,2}$ -edge absorption spectra of selected regions. The numbers correspond to the regions in Fig. 1.

[1] E. Hosono, J. Ceram. Soc. Japan **120** (2012) 47.

[2] D. Asakura, E. Hosono, M. Okubo, Y. Nanba, H. S. Zhou, P. A. Glans and J. H. Guo, ChemPhysChem **17** (2016) 4110.

BL4U

Elucidation of Mechanisms of Nucleation and Crystal Growth for Clean Energy Materials in Aqueous Solutions by Scanning Transmission X-ray Microscope

Y. Miseki^{1,2}, E. Hosono^{1,3,4}, D. Asakura^{3,4}, H. Yuzawa⁵ and T. Ohgashi^{5,6}

¹Global Zero Emission Research Center, National Institute of Advanced Industrial Science and Technology, Tsukuba 305-8568, Japan

²Research Center for Photovoltaics, National Institute of Advanced Industrial Science and Technology, Tsukuba 305-8565, Japan

³Research Institute for Energy Conservation, National Institute of Advanced Industrial Science and Technology, Tsukuba, 305-8568, Japan

⁴AIST-UTokyo Advanced Operando-Measurement Technology Open Innovation Laboratory (OPERANDO-OIL), National Institute of Advanced Industrial Science and Technology (AIST), Kashiwa 277-8565, Japan.

⁵UVSOR Synchrotron Facility, Institute for Molecular Science, Okazaki 444-8585, Japan

⁶School of Physical Sciences, The Graduate University for Advanced Studies, SOKENDAI, Okazaki 444-8585, Japan

We have studied the clean energy devices including lithium ion batteries [1,2] and photocatalytic devices [3] by controlling the morphology and crystal growth. Ceramics materials such metal oxides are main materials to construct many kinds of clean energy devices. The properties of metal oxide materials are depended in large part on crystal direction and facet of materials. Thus, nanostructural control methods have been studied by many researchers to improve each device performance.

For sophistication of nanostructural control techniques, understanding of crystal growth is very important. Especially, the surface and interface between materials and solution is active site for the catalytic reaction in the case of photocatalytic devices. Accurate design of crystal direction and facet and fabrication techniques are needed to create ideal reaction places.

To establish the high-level crystal growth techniques and morphology control methods, we considered that theoretical understanding from electronic structure level by using synchrotron radiation soft X-ray is necessary. A Scanning Transmission X-ray Microscope (STXM) exhibits electronic structure information with spatial information (minimum spatial resolution is ca. 30 nm). We tried the preparation of *operando* measurement system for crystal growth in STXM.

Figure 1 shows the optical microscope image of Fe²⁺ solution sandwiched by Si chips with Si₃N₄ windows.

One of the major features of STXM is that it is possible to obtain a spectrum of the solution by sandwiching it between the Si₃N₄ windows.

Figure 2 shows the spectrum of Fe from other sandwich cell constructed by photocatalytic materials and Fe solution.

In near future, we will establish in-situ measurement system.

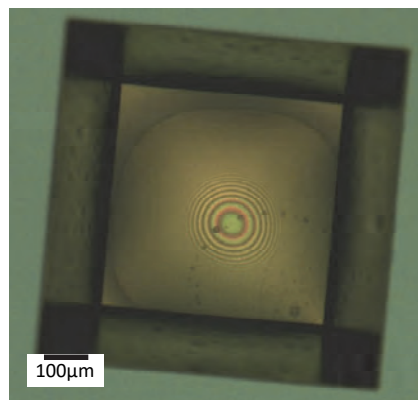


Fig. 1. Optical microscope image of Fe solution

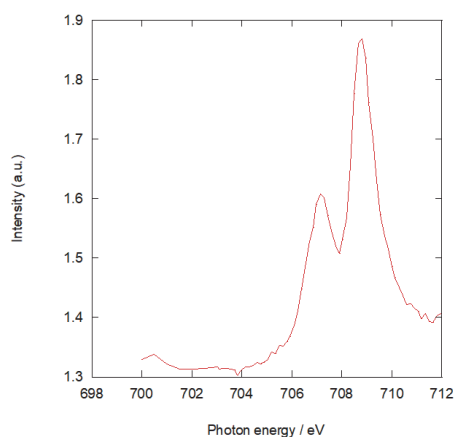


Fig. 2. Absorbance spectrum of Fe.

- [1] E. Hosono, J. Ceram. Soc. Jpn. **120** (2012) 47.
 [2] D. Asakura, E. Hosono, M. Okubo, Y. Nanba, H. S. Zhou, P. A. Glans and J. H. Guo, ChemPhysChem **17** (2016) 4110.
 [3] Y. Miseki and K. Sayama, Chem. Commun. **54** (2018) 2670.

BL4U

Characterization of Network-Domain of Sulfur Cross-linked Isoprene Rubber

K. Miyaji¹, Y. Sakaki¹ and Y. Ikeda²¹Graduate School of Science and Technology, Kyoto Institute of Technology, Kyoto 606-8585, Japan²Faculty of Molecular Chemistry and Engineering, Kyoto Institute of Technology, Kyoto 606-8585, Japan

Nowadays, rubber materials have become indispensable to applications such as automobile and airplane tires as well as seismic isolation materials. Many of these products are produced by cross-linking raw rubbers, which forms a three-dimensional network structure with good rubber elasticity. Among conventional cross-linking reactions, sulfur cross-linking reaction, known as “vulcanization” is most widely used all over the world. Despite the progress achieved in this field, controlled formation of rubber networks is generally very difficult and complicated in the rubber industry primarily because of the heterogeneous nature of the cross-linking reactions resulting from various factors such as the influence of cross-linking reagents, fillers, and processing methods. Therefore, the rational design of rubber network structures to produce sturdier and more stable rubber materials is still a challenge. Consequently, a deeper understanding of the rubber network structures is important for the development of rubber science and technology. In 2009, our group revealed the effects of the combination and composition of sulfur cross-linking reagents on the formation of an isoprene rubber network by using small-angle neutron scattering (SANS) [1]. The results showed that the combination of ZnO with other reagents was crucial for controlling the structural network inhomogeneity in the *N*-(1,3-benzothiazol-2-ylsulfanyl)cyclohexanamine (CBS)-accelerated vulcanization system. This specific morphology was found to be controlled by changing the amount of cross-linking reagents. There are several analytical methods to investigate the morphology of rubber vulcanizates. Scanning transmission X-ray microscopy (STXM) is one of methods which provides chemical mapping in nanometer scales. Also, both spatial and compositional chemical information are provided at the same time. In this study, STXM was used to confirm the two network-domain of isoprene rubber vulcanizate in terms of the distribution of sulfur.

The rubber compound was prepared by conventional mixing at room temperature on a two-roll mill with a water cooling system; isoprene rubber was mixed with zinc oxide, CBS and sulfur. Rubber vulcanizate was prepared by conventional pressing method. This rubber vulcanizate was extracted by tetrahydrofuran (THF) to remove the un-reacted sulfur. The vulcanized rubber sheet after THF extraction was cut by an ultra-microtome to prepare a smooth and flat surface with a thickness of approximately 100 nm for STXM measurement.

Figure 1 shows the STXM image of the vulcanized isoprene rubber at 165.4 eV. The intensity of the absorption indicates the concentrations of sulfur. Thus, the green to red regions shown in Figure 1 are the network-domains of the vulcanized isoprene rubber. As predicted by the SANS results, the network domains were formed by the absorption of sulfur and the accelerator, CBS on the ZnO clusters, and followed by sulfur cross-linking on the surface of ZnO clusters [1]. Furthermore, it was also found that the region of strong absorption and the mechanical properties of the vulcanizates increased linearly with the amount of the reagents.

This STXM image successfully confirmed the network-domains in the vulcanized isoprene rubber from the view point of sulfur distribution. The amount of ZnO was clearly suggested to be a key to control the total fraction of network domain phases in the vulcanizates.

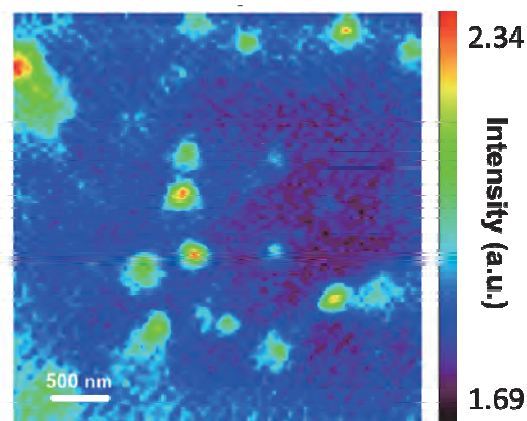


Fig. 1. STXM image of the vulcanized isoprene rubber at 164.5eV.

[1] Y. Ikeda *et al.*, *Macromolecules* **42** (2009) 2741.

BL4U

Single-Atom Nickel Decorated Graphitic Carbon Nitride for Efficient Water Splitting

Y. C. Huang^{1,2}, Y. R. Lu^{1,2}, C. H. Chuang¹, Y. Li³, S. Shen³, W. C. Chou², C. L. Dong¹,
W. F. Pong¹, T. Ohgashi⁴ and N. Kosugi⁴

¹Department of Physics, Tamkang University, Tamsui 251, Taiwan

²Department of Electrophysics, National Chiao Tung University, Hsinchu 30010, Taiwan

³International Research Center for Renewable Energy, State Key Laboratory of Multiphase Flow in Power Engineering, Xi'an Jiaotong University, Xi'an 710049, China

⁴UVSOR Synchrotron Facility, Institute for Molecular Science, Okazaki 444-8585, Japan

Incorporation of single atomic metals on graphite carbon nitride (g-C₃N₄) has been a promising strategy for designing advanced energy materials over the past decade. The single atom has the ability to separate charge in an aromatic conjugated ring by disrupting the coordination bonds in the microstructure. However, the relative polymerization based on metal ions and its subsequent charge separation are rarely reported. Here, single atomic nickel is used as a polymerization capping agent, which is synthesized by a chemisorption route to control the interface free energy. Scanning transmission X-ray microscope (STXM) and near-edge X-ray absorption fine structure (NEXAFS) were performed to study the chemically imaged K-edge of carbon, nitrogen and oxygen.

In order to hinder the recombination of photogenerated electrons and holes, a novel coordinated structure is proposed to insert an in-gap intermediate state. By adjusting the sp² coordination, efficient charge separation and charge transfer can be achieved to enhance photocatalytic ability. These results provide important insights into single-atom Ni/g-C₃N₄ which is of great importance for future overall water decomposition from atomic and electronic perspectives. It is likely that the capping agent Ni can terminate the growing of heptazine chain and build an extra energy state in the gap of the conduction and valence band, which is critical efficient separation of photogenerated electrons and holes.

The optical density images and corresponding stack mapping STXM images for C K-edge and N K-edge of bare ((a) and (b)) and Ni decorated g-C₃N₄ ((c) and (d)) are shown in the Fig. 1. The stack mappings display yellow, red and green areas, corresponding to the different regions that are associated with different regions and chemical properties of the nanorods which is revealed by the NEXAFS spectra. Notably, the incorporation of single atom Ni alters significantly the electronic structure both at C and N sites. Shortly, the increased intensity of N_A resonance suggests the coordination with metal Ni; the decreased intensity of N_B resonance indicates a structure breaking of bridge nitrogen, possibly is caused by the capping agent atomic Ni during the polymerization reaction. This results is consistent with the fact that the atom- distribution Ni could be coordinated with N atom in the heptazine units. Consequently, the strategy to synthesis single-atom Ni

incorporated g-C₃N₄ photocatalysis for spontaneous overall water splitting is promising. The single-atom Ni act as the capping agent for polymerization reaction, building novel coordinated structure with a mid-gap state for increasing the photogenerated electrons and holes separation.

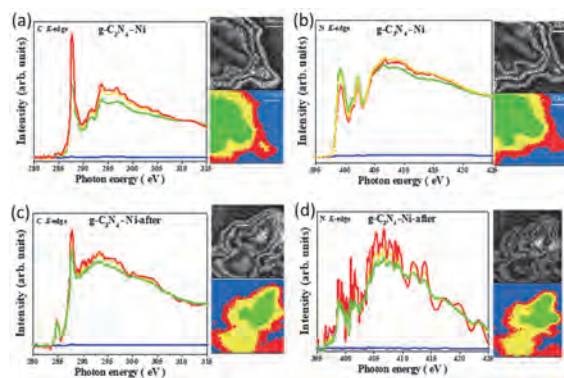


Fig. 1. Optical density images, stack mapped STXM images and corresponding NEXAFS at C and K-edge of pure g-C₃N₄ ((a), (b)) and single atom Ni decorated g-C₃N₄ ((c), (d)).

- [1] A. Wang *et al.*, Nat. Rev. Chem. **2** (2018) 65.
[2] L. Cao *et al.*, Nat. Catal. **2** (2019) 134.
[3] H. Yang *et al.*, Nat. Commun. **10** (2019) 4585.

BL4B

Electronic Structure of AlFeN Films Grown on Various Substrates

S. Imada and N. Tatemizo

Faculty of Electrical Engineering and Electronics, Kyoto Institute of Technology, Kyoto 606-8585, Japan

Wurtzite AlN is a wide- and direct-band-gap semiconductor that is a promising material for deep-ultraviolet (DUV) optoelectronic devices, such as light-emitting diodes (LEDs) or laser diodes (LDs). As the energy of deep ultraviolet light is high enough to sterilize and decompose toxic molecules, it is useful in the fields of medicine and healthcare. At present, DUV light sources are mercury lamps and metal halide lamps, which require a measurable amount of power, have a short life-span, and are large in size. To replace the lamps with LED systems that will be energy-saving, long-lasting, and small, the design and development of DUV-LEDs have been sped up around the world.

In the course of the studies, however, it became evident that AlN and related materials have difficult issues in realizing high efficiency devices owing to some electronic properties in the form of thin films, which are traced back to the crystal axis orientation of AlN, *i.e.* the polar-axis orientation. Therefore, non-polar-axis oriented AlN films have generated a lot of interest, because they can avoid these problems.

We have succeeded in growing non-polar-axis oriented wurtzite films by heavy-doping of Fe in AlN films on SiO₂ glass substrates [1] and found that the Fe-doping raised large gap states in the gap of AlFeN *via* Fe-*d* and N-*p* hybridization [2]. To remove the gap states, we conducted annealing of the films and succeeded in desorption of Fe atoms from the AlFeN lattice, resulting in a drastic decrease of the gap states while maintain the non-polar axis orientation [2].

To increasing the crystallinity of the annealed films, Si is more favorable as a substrate because its linear expansion coefficient is similar to that of AlN. Thus, we have grown AlFeN films on Si(100) substrates and investigated the crystallographic orientation and electronic structures. It was found that the AlFeN films with Fe concentrations higher than 10 % have *a*-axis orientation and similar electronic structure to that of the films grown on SiO₂ glass substrates. As representative data, N K-edge XANES spectra grown on Si(100) and SiO₂ glass substrates with 18 % Fe are shown in Fig. 1. The main structure between 400 eV and 409 eV and the pre-edge peak at around 397 eV of the film on a Si(100) substrate are coincident with those of the films on a SiO₂ glass substrate. This result also implies that the *a*-axis oriented growth by heavy Fe doping can proceed as self-nuclear formation. We are attempting to obtain growth-time dependences of the crystallographic orientation and electronic structures of as-grown AlFeN films. The results from these efforts are expected to be reported in our future publications.

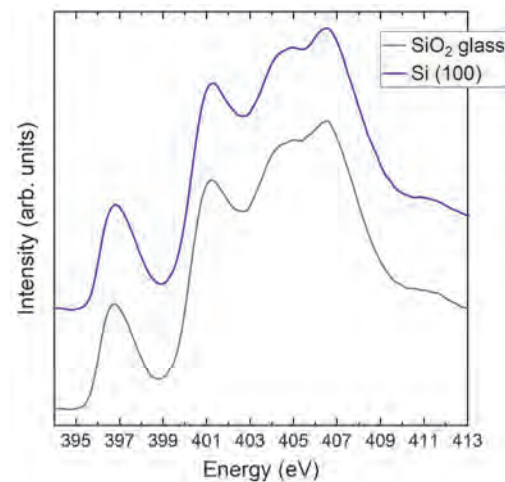


Fig. 1. N K-edge XANES spectra of AlFeN (Fe: 18 %) films deposited on SiO₂ glass and Si(100) substrates. The electric field vectors E of the incident X-rays were parallel to the film plane. The measurements were performed in vacuum $\sim 10^{-6}$ Pa at RT in the fluorescence-detection mode.

[1] N. Tatemizo, S. Imada, K. Nishio and T. Isshiki, *AIP advances* **8** (2018) 115117.

[2] N. Tatemizo, S. Imada, K. Okahara, H. Nishikawa, K. Tsuruta, T. Ina, Y. Miura, K. Nishio and T. Isshiki, *Scientific Reports* **10** (2020) 1819.

BL4B

Valence State Analysis of Mn Ions in SnO₂T. Yamamoto^{1,2,3}¹Department of Materials Science, Waseda University, Tokyo 169-8555, Japan²Institute of Condensed-Matter Science, Waseda University, Tokyo 169-8555, Japan³Kagami Memorial Research Institute for Materials Science and Technology, Waseda University, Tokyo 169-0051, Japan

Dilute magnetic materials (DMMs) have been extensively studied after a discovery of ferromagnetism in InAs doped with dilute amount of Mn ions [1], since such materials have a potential to be applied in spintronics. At early stage, a Currie temperature, T_C , was low in this type of DMMs. Hence a lot of attempts have been devoted to increase T_C for the application in industrial uses. Recently, it was reported that some DMMs show ferromagnetism beyond room temperature, e.g., Mn-doped GaN, Co-doped TiO₂ and Mn, Fe co-doped In₂O₃. However, the mechanism of appearance of ferromagnetism in DMMs have not yet been understood. Although it is essential to know a local environment of doped magnetic ions in host materials, such analysis has not often been done due to a difficulty to analyze it for dilute dopants. It was proposed that two types of local environments of doped magnetic ions exist in DMMs, i.e., substitution and precipitate types. In the former, doped magnetic ions substitute at one of the cation site in the host material, while in the later doped magnetic ions precipitate as small particles. For such analysis, X-ray absorption spectroscopy (XAS) is quite powerful. We have successfully determined the local environment of doped Mn and Fe ions in In₂O₃ by using the XAS analysis [2,3].

In the current study, valence state of Mn ions in SnO₂ was investigated by the Mn-L₃ XAS. Samples were prepared with conventional solid-state reaction method changing a concentration of doped Mn ions. Crystal structures of the synthesized samples were examined by powder X-ray diffraction, which suggest all the samples were in singular phase of rutile structured SnO₂. Mn-L₃ XAS were recorded at BL4B in UVSOR by total electron yield mode using electron multiplier. Sample powders were placed on the carbon adhesive tape, which were attached on the first dinode of the electron multiplier.

Observed Mn-L₃ XAS of Mn(1 %) doped SnO₂ is shown in Fig. 1 together with the representative spectra of Mn²⁺, Mn³⁺ and Mn⁴⁺ for comparison. Most intense peak in XAS of Mn-doped SnO₂ coincides with that of Mn²⁺ and the second overlaps that of Mn³⁺. This result suggests that the major component of Mn ions is 2+ and Mn³⁺ exists as minor one in SnO₂. In the carrier mediated type of the models for DMMs, mixed valence is a key to make the material ferromagnetic as suggested in our earlier work [3]. From our current analysis, it has been suggested that Mn-doped SnO₂ has a possibility to be a ferromagnetic DMM.

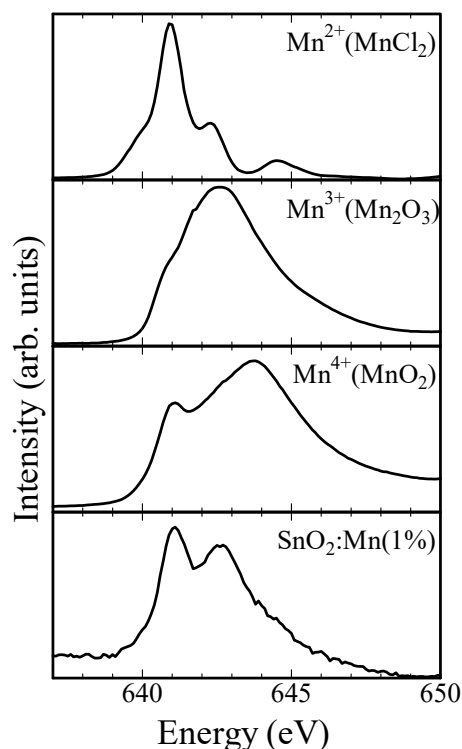


Fig. 1. Mn-L₃ X-ray absorption spectra of MnCl₂, Mn₂O₃, MnO₂ and Mn-doped SnO₂.

- [1] H. Ohno *et al.*, Phys. Rev. Lett. **68** (1992) 2664.
 [2] T. Yamamoto *et al.*, J. Phys.:Condens. Matter **21** (2009) 104211.
 [3] T. Okazaki *et al.*, Solid State Comm. **151** (2011) 1749.

BL4B

XAFS Measurements of 1-nanometer Indium-tin Oxide Particles Focusing on O K-edge

T. Tsukamoto^{1,2}, H. Iwayama³, M. Nagasaka³, A. Kuzume² and K. Yamamoto^{1,2}

¹Laboratory for Chemistry and Life Science, Institute of Innovative Research, Tokyo Institute of Technology, Yokohama 226-8503, Japan

²ERATO, JST, Kawaguchi 332-0012, Japan

³Institute for Molecular Science, Okazaki 444-8585, Japan

Sub-nanoparticles (SNPs) with extremely small size reaching 1 nm recently attract attention because they often exhibit unique properties not seen in bulk or general nanoparticles (NPs). One of the interesting behavior in this size range is the change in the chemical states of oxygen atoms in metal oxide SNPs. They don't have crystal structures but amorphous ones with many defects due to their extremely small structures. Additionally, they tend to substitute their lack of oxygen atoms (O^{2-} state) to low-valent hydroxyl groups (OH^- state). Actually, it is reported that tin oxide SNPs and copper oxide SNPs contain many OH^- species in contrast to the bulk and NPs [1,2].

In this study, we newly investigated the effect of the hybridization of different metals in the SNPs for the chemical states of oxygen atoms. We chose indium and tin as two metal elements with different valence electrons in the same period in the periodic table. The oxygen species in indium-tin oxide SNPs were observed and analyzed by XAFS measurements focusing on the O K-edge using BL4B beamline in UVSOR. As a bulk of metal oxides, indium oxide (In_2O_3) and tin oxide (SnO_2) purchased from Sigma-Aldrich Co. LLC. were used. As NPs, indium oxide (100 nm), tin oxide (100 nm), and indium-tin oxide (50 nm, $In_2O_3/SnO_2 = 9:1$) purchased from Sigma-Aldrich Co. LLC. were used. As SNPs, indium oxide (1 nm, $In_{28}O_x$), tin oxide (1 nm, $Sn_{28}O_x$), and indium-tin oxide (1 nm, $In_{12}Sn_{16}O_x$) synthesized by the atom-hybridization method [3] were used. All the samples were cast on the silicon substrate and dried in vacuo in the instrument overnight. The XAFS spectra were recorded according to both the total electron yield and the partial fluorescence yield. The O K-edge XAFS spectra of samples were standardized using the oxide layer on the surface of the reference Si substrate.

In comparison among the bulks, NPs, and SNPs composed of a single metal element, it was suggested that only the SNPs contain OH^- species in contrast to their bulks or NPs, judging from the XAFS spectra in O K-edge region [4,5] (Fig. 1). Moreover, the indium-tin bimetallic oxide SNPs showed remarkably higher peak intensity than the monometallic ones (Fig. 2). This result indicated that the indium-tin oxide SNP has more OH^- species. On the other hand, in the case of the indium-tin oxide NP, the peaks corresponding to OH^- species were not observed. Therefore, the increase in the amount of OH^- species in such binary systems would be a specific phenomenon in the SNPs

with 1 nm particle size.

In conclusion, it was suggested that the hybridization of two metal elements in metal oxide SNPs with quantum-sized structure produces more defect structures, leading to the unique chemical states of metal oxides.

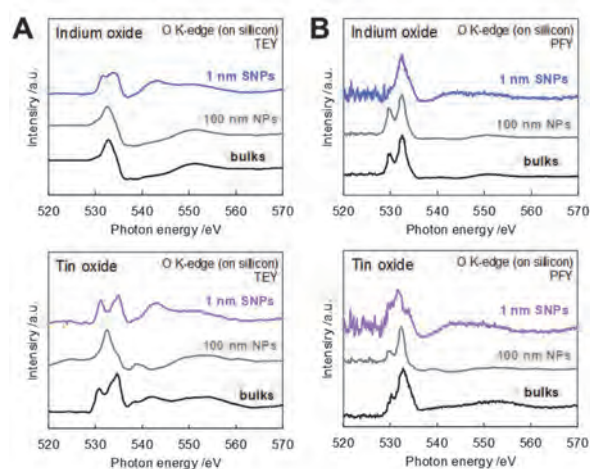


Fig. 1. O K-edge XAFS spectra of bulks, NPs, and SNPs of metal oxides on Si substrate by (A) total electron yield and (B) partial fluorescence yield. Only for the SNPs, signals originating OH^- species at 534 and 542 eV were superimposed on those of O^{2-} one.

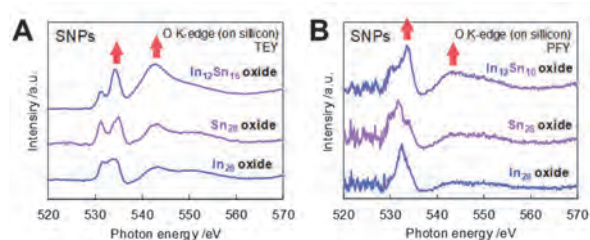


Fig. 2. O K-edge XAFS spectra of indium oxide, tin oxide, and indium-tin oxide SNPs on Si substrate by (A) total electron yield and (B) partial fluorescence yield. For the bimetallic oxide SNPs, signals originating OH^- species at 534 and 542 eV were superimposed on those of O^{2-} one.

- [1] A. Kuzume *et al.*, *Sci. Adv.* **5** (2019) eaax6455.
- [2] K. Sonobe *et al.*, *ACS Nano* **14** (2020) 1804.
- [3] T. Tsukamoto *et al.*, *Nat. Commun.* **9** (2018) 3873.
- [4] M. Yoshida *et al.*, *J. Phys. Chem. C* **119** (2015) 19279.
- [5] M. Nagasaka *et al.*, *Chem. Phys. Lett.* **375** (2003) 419.

BL4B, BL3B

Soft X-ray Excitation Impurity Luminescence of Aluminum Nitride

Y. Maegawa¹, T. Banno¹, K. Fukui¹ and K. Yamamoto²

¹Department of Electrical and Electronics Engineering, University of Fukui, Fukui 910-8507, Japan

²Far-infrared region Development Research Center, University of Fukui, Fukui 910-8507, Japan

AlN is a material having the largest band gap energy ($E_g = 6.2$ eV) among group III-V nitride semiconductors, and is important as a key material of an ultraviolet (UV) region light emitting device (LED). For LED study, impurity luminescence (IL) that is due to the existence of the state of impurity and/or defect in the band gap gives important information about the impurity atoms. In the case of our bulk AlN sample, visible (VIS) - UV region excitation photoluminescence measurements, three kinds of IL bands (B_L around 2.6 eV, B_H around 2.8 eV, UV around 4.0 eV) were observed [1]. These IL bands were only observed in the excitation region up to E_g . Band to band excitation ($> E_g$) is not able to contribute to these IL. Our results are quite similar to those of Alder *et al.* and are considered that B_H and UV bands may be due to carbon (C) defects [2]. Then, we performed soft X-ray excitation IL measurements, because the inner-shell excitation by using soft X-ray shows C, nitrogen (N), and oxygen (O) 1s electron contributions to those IL.

A bulk AlN sample is commercially available disk-shaped one and manufactured by physical vapor transport method. Excitation photon energy regions were around C K-edge (270 - 298 eV), N K-edge (400 - 415 eV), O K-edge (538 - 550 eV) and 4.0 - 6.8 eV (BL3B). All measurement were carried out at 10 K.

Figure 1 shows an emission spectrum at an excitation energy of 292 eV (black) and a result of component decomposition. The IL spectrum due to soft X-ray excitation consists of a main peak around 2.7 eV with tail shape on the higher energy side and is different from that due to under E_g energy excitation, which has no tail feature. However, main peak and tail shape of the IL spectrum due to soft X-ray excitation are able to decompose into B_L , B_H , and V_L , V_H emission bands, respectively, where V_L band corresponds to the emission band observed under electron beam excitation [3]. Since the energy region of V_H band matches that of UV emission, V_H band probably includes UV band. Figure 2 shows the excitation spectrum of each band near each absorption edge. The characteristic spectrum shape at C K-edge and the flat-like spectrum shape at O K-edge clearly suggest that C impurity is corresponding to those IL and O impurity is not. The intensity decrease above N K-edge is caused by the decrease of penetration depth of excitation light.

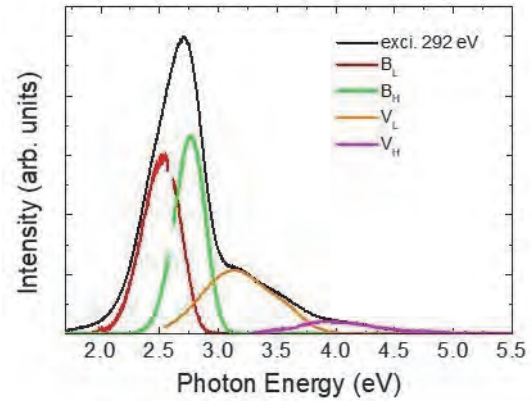


Fig. 1. Emission spectrum (exci. at 292 eV) and component decomposition results

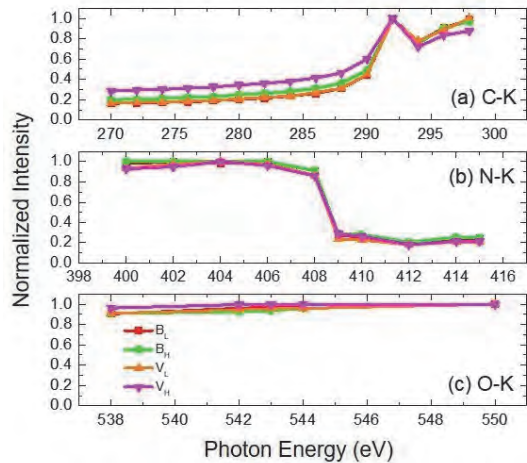


Fig. 2. Excitation spectrum of each emission band around (a) C-, (b) N-, (c) O-K edge, respectively.

[1] W. Kamihigoshi *et al.*, UVSOR Activity Report 2018 **46** (2019) 103.

[2] D. Alden *et al.*, Phys. Rev. Appl. **9** (2018) 054036.

[3] M. Morita *et al.*, Jpn. J. Appl. Phys. **21** (1982) 7.

BL5U

Electronic States of Antiferromagnetic Half-heusler GdPtBi Studied by High-resolution ARPES

D. Takane¹, T. Suzuki², S. Souma^{3,4}, K. Nakayama¹, K. Hori¹, Y. Kubota¹, T. Ren¹,
K. Sugawara^{1,3,4}, T. Takahashi^{1,3,4}, J. G. Checkelsky² and T. Sato^{1,3,4}

¹Department of Physics, Tohoku University, Sendai 980-8578, Japan

²Department of Physics, Massachusetts Institute of Technology, Cambridge, MA 02139, USA

³Center for Spintronics Research Network, Tohoku University, Sendai 980-8577, Japan

⁴WPI Research Center, Advanced Institute for Materials Research, Tohoku University, Sendai 980-8577, Japan

Topological insulators are a novel quantum state of matter in which an inverted nontrivial bulk-band structure leads to gapless edge or surface states protected by the time-reversal symmetry [1-3]. The discovery of topological insulators triggered the search for new types of topological materials, as represented by the experimental discoveries of topological crystalline insulators with gapless surface states protected by the mirror symmetry of the crystal [4] and topological Dirac semimetals with three-dimensional bulk Dirac fermions protected by the rotational symmetry of the crystal [5].

Recent theoretical studies predicted exotic topological phases originating from the interplay between nontrivial band topology and long-range order, e.g. magnetism and superconductivity. A leading platform for exploring such novel topological states is the rare-earth half-Heusler $RePtBi$ (Re : rare-earth) which exhibits various ordered phases depending on the rare-earth [see Fig. 1(a) for crystal structure]. Among them, antiferromagnet GdPtBi (Néel temperature $T_N = 9\text{K}$) is attracting particular interests because it exhibits the peculiar physical properties including the large anomalous Hall effect and chiral anomaly [6,7]. It is thus highly desirable to experimentally establish the electronic band structure of GdPtBi and clarify its topological character and relationship with unconventional physical properties.

In this study, by using high-resolution angle-resolved photoemission spectroscopy (ARPES), we determined the fine electronic structure on the GdPtBi (111) surface [see Fig. 1(b) for corresponding bulk and surface Brillouin zones]. High-resolution ARPES measurements have been performed at BL5U. The sample was cleaved *in situ* under an ultrahigh vacuum of 1.0×10^{-10} Torr.

Figure 1(c) displays the valence-band dispersion in the paramagnetic phase measured along a momentum cut crossing the Brillouin-zone center. We observed highly dispersive holelike bands which cross the Fermi level to form Fermi surfaces. The Fermi surfaces are three-fold symmetric, in agreement with the rotational symmetry of the crystal. Also, the observed band dispersions are qualitatively consistent with the first-principles band-structure calculations, confirming their bulk-band nature which was further corroborated by the $h\nu$ -dependent ARPES measurements. Furthermore, we have performed high-resolution ARPES measurements to search for the topological surface states as well as the

electronic reconstruction induced by the antiferromagnetic transition. Our results provide important insights into the origin of exotic physical properties and also into the topological property of GdPtBi.

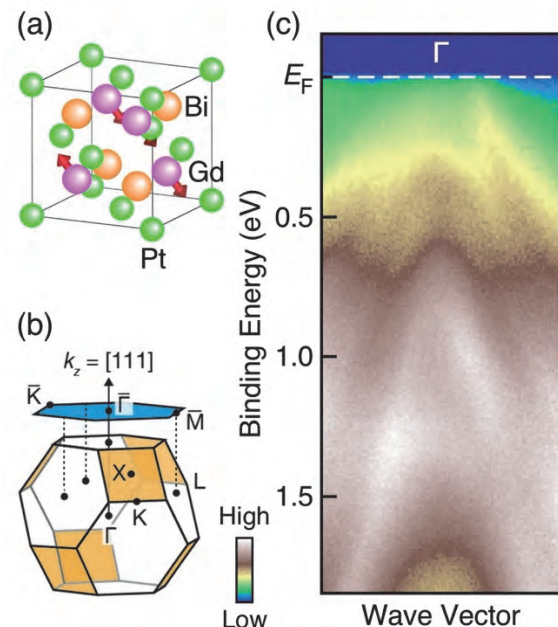


Fig. 1. (a) and (b) Crystal structure and corresponding bulk (bottom) and surface (top) Brillouin zones of GdPtBi, respectively. (c) ARPES intensity plotted as a function of binding energy and wave vector, measured at $T = 40$ K.

- [1] Y. Ando, J. Phys. Soc. Jpn. **82** (2013) 102001.
- [2] X.-L. Qi and S.-C. Zhang, Rev. Mod. Phys. **83** (2011) 1057.
- [3] M. Z. Hasan and C. L. Kane, Rev. Mod. Phys. **82** (2010) 3045.
- [4] Y. Tanaka *et al.*, Nature Phys. **8** (2012) 800.
- [5] Z. K. Liu *et al.*, Science **343** (2014) 864.
- [6] T. Suzuki *et al.*, Nature Phys. **12** (2016) 1119.
- [7] M. Hirschberger *et al.*, Nature Mater. **15** (2016) 1161.

BL5U

Electronic Structure Study on WSe₂ / hBN Heterostructure Using Micro-ARPES

 D. J. Oh^{1,2}, S. Lee^{1,2}, H. Park^{1,2}, K. Tanaka³, S. R. Park⁴ and C. Kim^{1,2}
¹Department of Physics and Astronomy, Seoul National University (SNU), Seoul 08826, Republic of Korea

²Center for Correlated Electron Systems, Institute for Basic Science (IBS), Seoul 08826, Republic of Korea

³Editorial Board, UVSOR Synchrotron Facility, Institute for Molecular Science, Okazaki 444-8585, Japan

⁴Department of physics, Incheon National University, Incheon 406-772, Korea

Eccentric properties ensue from moiré superlattices formed by constituent layers in van der Waals (vdW) heterostructures. For example, the Hofstadter butterfly pattern stemming from the interplay between the moiré superlattice and an applied magnetic field was measured in monolayer (ML) graphene / h-BN heterostructures [1]. An essential step towards understanding novel properties of these heterostructures is to have electronic structure information. In that respect, direct electronic structure measurement of the ML graphene / h-BN heterostructure by using ARPES was an important development [2]. Recently, mini bands induced by moiré superlattice were observed in graphene / WS₂ heterostructures [3]. These developments open the possibility that a similar scheme may be applied to transition metal dichalcogenide (TMD)-based heterostructures. Since a plethora of intriguing physical properties such as superconductivity, Weyl physics and charge density waves exist in TMDs, even more exciting phenomena may arise in vdW heterostructures constructed from these materials.

Among variety of TMDs, group VI TMDs (MX₂, M= Mo, W, X= S, Se) have been extensively studied due to their valley and spin degrees of freedom induced by large spin-orbit interaction and Berry curvature [4]. In addition, MX₂'s are stable in atmosphere, making them suitable for surface-sensitive experiments as well as applications in optoelectronic devices. In order to study electronic structure of TMD-based heterostructures, the samples are fabricated using the following procedures. First, Pt was evaporated into an inverse-T shape on Nb doped TiO₂ or degenerately doped SiO₂ / Si substrates, such that Pt comes into contact with the metal strip and makes a conducting channel for electrons (Fig. 1a). Using the dry-transfer method, mechanically exfoliated h-BN and 1ML WSe₂ are sequentially transferred, so that they make partial contact with a corner of the Pt pattern (Figs. 1b-1d). Thus, we could effectively avoid sample charging at low temperatures (~100 K) even though samples are placed on insulating substrates. In order to efficiently find the precise position of the sample, we mapped out photoemission intensity at the Fermi level (Figs. 1e-1f) and W 4f_{7/2} core (Fig. 1g) near the Pt corner by utilizing the micro beam (~30 μm). The so-obtained spatial map was found to be consistent with an optical image of the sample. Then, we moved to the region of interest (1ML WSe₂ region) and obtained the electronic structure of 1ML WSe₂ / h-BN over the

Brillouin zone (BZ) (Fig. 2). Here, we did not have to rotate the sample for the BZ mapping because we used a photoelectron analyser equipped with deflectors. By following the procedure, we were able to attain ARPES data with a relatively high success rate.

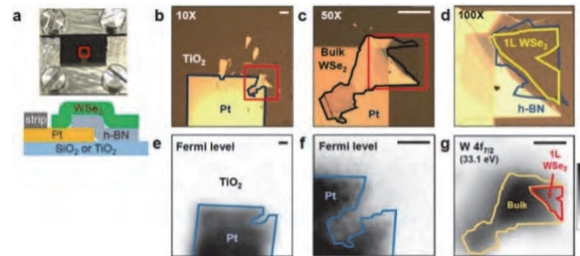


Fig. 1. Optical image (a~d) and spatial map of photoemission intensity (e~g) of the monolayer WSe₂ / h-BN heterostructure. Scale bar, 100 μm.

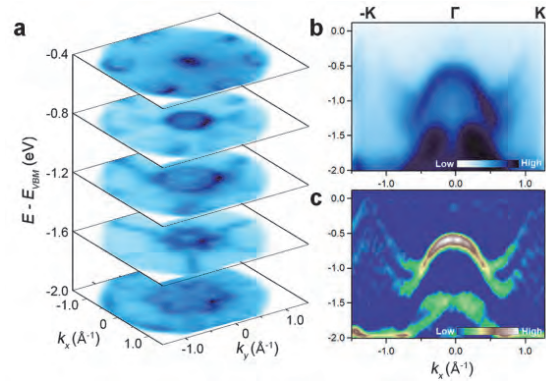


Fig. 2. Electronic structure of monolayer WSe₂ / h-BN heterostructure.

[1] B. Hunt *et al.*, *Science* **340** (6139) (2013) 1427.

[2] E. Wang *et al.*, *Nat. Phys.* **12** (2016) 1111.

[3] S. Ulstrup *et al.*, arXiv : 1904.06681 (2019).

[4] X. Xu *et al.*, *Nat. Phys.* **10** (2014) 343.

[5] Q. Zhu *et al.*, *Sci. Adv.* **5** (1) (2019) eaau6120.

BL5U

Three-dimensional Angle-resolved Photoemission Study of Ullmannite NiSbS with the Cubic Chiral Crystal Structure

T. Ito^{1,2}, T. Hosoya², M. Nakatake³, S. Ideta^{4,5}, K. Tanaka^{4,5}, M. Kakihana⁶, D. Aoki⁷,
A. Nakamura⁷, T. Takeuchi⁸, H. Harima⁹, M. Hedo¹⁰, T. Nakama¹⁰ and Y. Ōnuki¹⁰

¹Nagoya University Synchrotron radiation Research center (NUSR), Nagoya University, Nagoya 464-8603, Japan

²Graduate School of Engineering, Nagoya University, Nagoya 464-8603, Japan

³Aichi Synchrotron Research Center, Seto, 489-0965, Japan

⁴UVSOR Synchrotron Facility, Institute for Molecular Science, Okazaki 444-8585, Japan

⁵The Graduate University for Advanced Studies, SOKENDAI, Okazaki 444-8585, Japan

⁶Graduate School of Engineering and Science, University of the Ryukyus, Nishihara-cho 903-0213, Japan

⁷Institute for Materials Research, Tohoku University, Sendai 980-8577, Japan

⁸Low Temperature Center, Osaka University, Toyonaka 560-0043, Japan

⁹Graduate School of Science, Kobe University, Kobe 657-8501, Japan

¹⁰Faculty of Science, University of the Ryukyus, Nishihara-cho 903-0213, Japan

Non-centrosymmetric compounds have attracted much attention due to their interesting phenomena relating with inversion symmetry breaking. The ullmannite type NiSbS with the non-centrosymmetric cubic chiral structure has recently been suggested to be a possible candidate of Weyl semimetal [1]. Indeed, split Fermi surface topologies reflecting the cubic chiral crystal structure and the spin-orbit interactions have been reported [2]. In this study, we have performed angle-resolved photoemission spectroscopy (ARPES) on NiSbS to directly investigate the electronic band structure of this system.

ARPES measurements were performed at the UVSOR-III BL5U. Data were acquired at $T = 25$ K with $h\nu = 40 - 96$ eV. To directly trace the Γ R high-symmetry line with using photon energy dependent ARPES at the normal emission angle ($\theta = 0^\circ$), clean sample surfaces were obtained by *in situ* cleaving on (111) plane.

Figures 1(a) and (b) show the k_x - k_z constant energy image at the Fermi level E_F (a) and 400 meV (b) on Γ XRM plane of NiSbS. We have clearly found the inclined shape of the obtained images. The observed inclined shape is consistent with the tetragonal shape of Γ XRM plane where k_z axis corresponds to the diagonal Γ R line (Fig.1(c)). From the symmetry of the obtained images, we have estimated the inner potential of $V_0 = 33$ eV which is relatively larger than one of (001) cleaved surface ($V_0 = 24.7$ eV) [3].

Figure 1(c) shows the band structure along Γ R line obtained from the normal emission ARPES spectra. From the comparison with the band structure calculation (solid lines), we have found slight narrowing of the dispersive features relative to the calculation, while the rough tendency seems to be similar. According to the band calculation, existence of Weyl point (WP) has been expected around $k_z = 5.2 \text{ \AA}^{-1}$, where we found no band crossing except for the broad distribution between the non dispersive feature around 400 meV and the dispersive feature approaching E_F . To understand the relation between the electronic structure and the chiral crystal structure,

we are going to perform linear and circular polarization dependent ARPES on this system in near future.

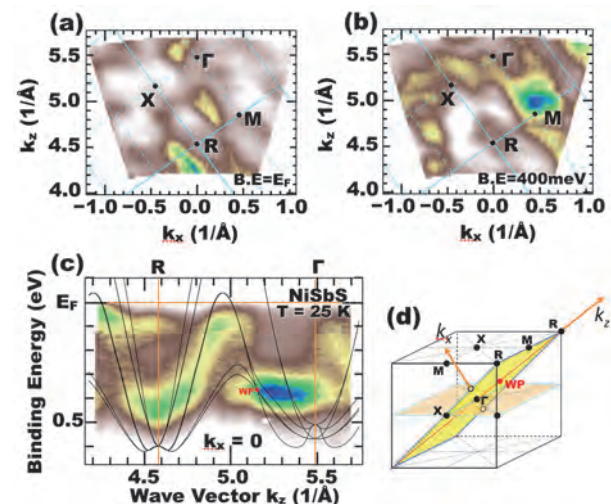


Fig. 1. (a,b) k_x - k_z constant energy image at E_F (a) and 400 meV (b) on Γ XRM plane of NiSbS. (c) Band structure along Γ R line. Solid lines are band calculation [2]. (d) Cubic Brillouin zone shown with k_x and k_z axis defined for the sample surface obtained by cleaving on (111) plane.

[1] A. Furusaki, Sci. Bulletin **62** (2017) 788.

[2] M. Kakihana *et al.*, J. Phys. Soc. Jpn. **84** (2015) 084711.

[3] T. Ito *et al.*, UVSOR Activity Report 2018 **46** (2019) 96.

BL5U

Electronic Band Structure of Sn_4Sb_3

 W. Wen^{1,2}, C. Y. Hong^{1,2}, G. Zhao^{1,2}, Z. Song^{1,2} and R. -H. He²
¹Department of Physics, Fudan University, Shanghai 200433, China

²School of Science, Westlake Institute for Advanced Study, Westlake University, Hangzhou 310064, China

Recently, alloys consisting of heavy elements have received much attention because of their strong spin-orbit coupling (SOC), which could give rise to a variety of topological phases [1,2], including topological semimetals (TSM), topological (crystalline) insulators and Topological superconductors (TSC). Topological superconductors (TSC) are the superconducting analogues of TI, and have potential applications in fault-tolerant quantum computing [2-4]. The superconducting binary compound Sn_4Sb_3 has been proposed to be a candidate for TSC [5].

To study the electronic band structure of Sn_4Sb_3 , we performed systematic ARPES measurements on its cleaved (001) surface, and a series of Fermi surface intensity maps were measured with linearly-horizontally (LH) polarized photons of photon energy ($h\nu$) from 60 eV to 140 eV and $T=7.0$ K. Figures 1(a) and (b) are two Fermi surface maps obtained with $h\nu=70$ eV and $h\nu=115$ eV. Figures 1 (c) and (d) show the Fermi surface obtained with first-principles calculations in the k_x - k_y plane at $k_z=0$ and $k_z=\pi$. Through comparison, we can see the experimental Fermi surface of $h\nu=70$ eV agrees with the calculated one at $k_z=0$, and that of $h\nu=115$ eV agrees with that at $k_z=\pi$. A good overall agreement on the Fermi surface between the measured photon energy dependence and the calculated k_z dependence can be obtained by assuming an inner potential $V_0 = 12.8$ eV (and the c -axis lattice constant 24.85 Å as determined from x-ray diffraction).

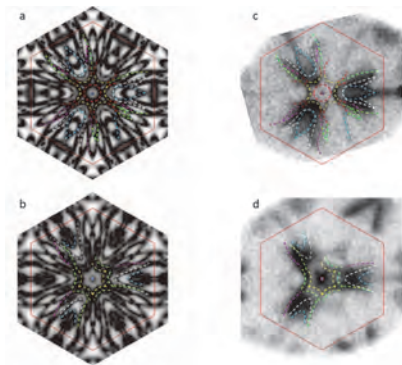


Fig. 1. ARPES measurements of the Fermi surface with LH polarized light with (a) $h\nu = 70$ eV and (b) $h\nu = 115$ eV. (c) and (d) show the Fermi surfaces in the k_x - k_y plane at $k_z = 0$ and $k_z = \pi$ respectively. Dashed curves in different colors identify features observable in both the experiment and calculation.

Nevertheless, there are some states observed in the experiment but absent in the calculations. These states are marked as rounded dashed curves around the K points (corners of the hexagonal Brillouin zone) in Fig. 2 where the k_x - k_y energy contours at binding energy -0.3 eV measured with different photon energies are shown.

These states exhibit linear dispersions extending toward the Fermi level (Fig. 3). This appears to be consistent with the presence of Weyl points in the bulk band structure. Further analyses and comparison with first-principles calculations based on the slab model are necessary in order to establish this plausible connection before one can draw a conclusion on the Weyl nature of Sn_4Sb_3 .

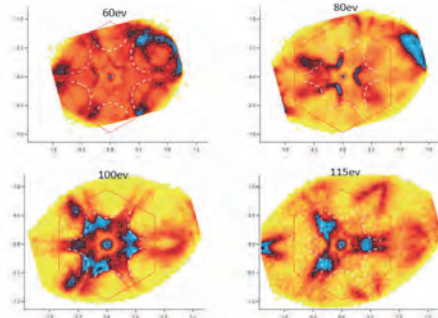


Fig. 2. Observation of surface states with $h\nu=60$ eV, 80 eV, 100 eV and 115 eV. k_x - k_y energy contours are shown at binding energy -0.3 eV, with the surface states eyeguided by the white dashed curves.

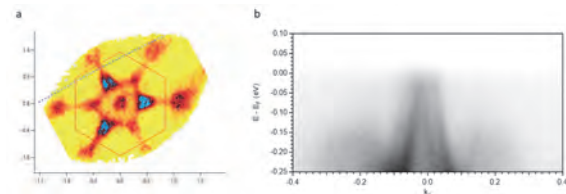


Fig. 3. Bulk-band structure and observation of the Weyl point. (a) Fermi surface maps measured with $h\nu=105$ eV. (b) Band dispersion along the blue dashed line in (a).

- [1] M. Z. Hasan and C. L. Kane, *Rev. Mod. Phys.* **82** (2010) 3045.
- [2] X. L. Qi and S. C. Zhang, *Rev. Mod. Phys.* **83** (2011) 1057.
- [3] J. Alicea, *Rep. Prog. Phys.* **75** (2012) 076501.
- [4] M. Sato and Y. Ando, *Rep. Prog. Phys.* **80** (2017) 076501.
- [5] B. Liu *et al.*, *Phys. Rev. Mater.* **3** (2019) 084603.

BL5U

High-resolution ARPES Study of Antiferromagnetic Topological-insulator Candidate CeBi

S. Souma^{1,2}, K. Nakayama³, D. Takane³, Y. Kubota³, T. Kawakami³, K. Sugawara^{1,2,3},
M. Yoshida⁴, A. Ochiai³, T. Takahashi^{1,2,3} and T. Sato^{1,2,3}

¹Center for Spintronics Research Network, Tohoku University, Sendai 980-8577, Japan

²WPI Research Center, Advanced Institute for Materials Research, Tohoku University, Sendai 980-8577, Japan

³Department of Physics, Tohoku University, Sendai 980-8578, Japan

⁴Max-Planck-Institute for Solid State Research, Heisenbergstrasse 1, 70569 Stuttgart, Germany

Cerium monopnictides CeX_p ($X_p = P, As, Sb,$ and Bi) are a typical example of heavy-fermion systems showing an exotic and complicated magnetic phase diagram as a function of temperature, pressure, and magnetic field, known as a “devil’s staircase” [1-4]. Recently, it was predicted that isostructural material LaX_p becomes a topological insulator due to the band inversion at the X point of bulk Brillouin zone [5]. The proposal of the non-trivial electronic bands has renewed the interest for RX_p ($R = La$ and Ce) systems, and has triggered intensive theoretical and experimental investigations, resulting in the discovery of extremely large magnetoresistance and unusual resistivity plateau in $LaSb$ and $LaBi$, as well as the observation of Dirac-cone-like energy band in some RX_p compounds. Taking into account such topological aspects of RX_p family, one would naturally expect that $CeBi$ is an excellent candidate to study the interplay between magnetism and topological properties, since it shows interesting magnetic phases characterized by a two-step antiferromagnetic (AF) transition at $T = 25$ and 14 K under zero-magnetic field [3, 4], in addition to the expected topological nature. In a broader perspective, it is of great importance to experimentally clarify the role of antiferromagnetism to the topological properties, which is currently a target of intensive debates in theories while no concrete experimental data have been hitherto reported.

In this study, we performed high-resolution angle-resolved photoemission spectroscopy (ARPES) of $CeBi$ to determine the bulk and surface electronic states and their evolution across the Néel temperatures. For this sake, we utilized high- energy-resolution and low-accessible-temperature capabilities of BL5U. Single crystalline samples were cleaved *in situ* in an ultrahigh vacuum of 1×10^{-10} Torr along the (100) crystal plane [see Fig. 1(a) for corresponding bulk and surface Brillouin zones].

Figures 1(b) and 1(c) show the ARPES intensity plots along the $\bar{\Gamma}\bar{M}$ cut measured in the paramagnetic (PM) and AF states, respectively. In the PM phase, we observed several bulk bands displaying the holelike and electronlike dispersions centered at the $\bar{\Gamma}$ and \bar{M} points, respectively. In addition, we found the surface states with a Dirac-cone-like dispersion at the \bar{M} point. In the AF phase, the overall bulk band dispersions are

similar to those in the PM phase. However, the surface states show a drastic change across T_N ; linearly-dispersive Dirac-like band appears at the $\bar{\Gamma}$ point. This finding suggests an intricate interplay between antiferromagnetism and topological surface states in $CeBi$.

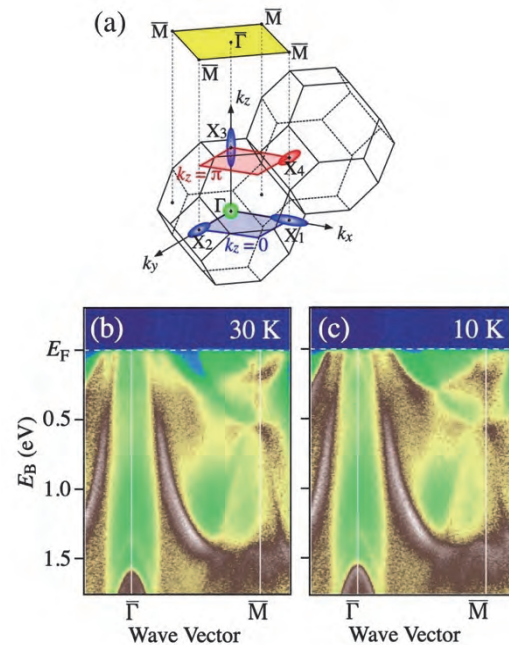


Fig. 1. (a) Bulk and surface Brillouin zones of $CeBi(111)$. (b) and (c) ARPES intensity plots at $T = 30$ K and 10 K, respectively, measured with $h\nu = 53$ eV along the $\bar{\Gamma}\bar{M}$ cut.

[1] J. Rossat-Mignod *et al.*, Phys. Rev. B **16** (1977) 440.

[2] J. Rossat-Mignod *et al.*, J. Magn. Magn. Mater. **31-34** (1983) 398.

[3] H. Bartholin *et al.*, Le J. Phys. Colloq. **40** (1979) C5.

[4] M. Kohgi *et al.*, Physica B **281-282** (2000) 417.

[5] M. Zeng *et al.*, arXiv:1504.03492 (2015).

BL5U

ARPES Studies of the Superconductors with Row-carrier-density

Y. Akimoto¹, K. Kuroda¹, K. Kawaguchi¹, S. Sakuragi¹, Y. Arai¹, Y. Wan¹, K. Kurokawa¹,
H. Tanaka¹, S. Ideta², K. Tanaka², D. Hirai¹, Z. Hiroi¹, T. Yamada³ and T. Kondo¹

¹ISSP, The University of Tokyo, Kashiwa 277-8581, Japan

²UVSOR Synchrotron Facility, Institute for Molecular Science, Okazaki 444-8585, Japan

³IMRAM, Tohoku University, Sendai, 980-0812, Japan

NaAlSi is a three-dimensional superconducting material with $T_c \sim 7$ K [1]. Previous first-principles calculations indicate that the electronic structure of NaAlSi shows semimetallic low carrier density states because of occurring of the carrier compensation. In the case of general superconductor with dilute carrier state, $T_c \sim 7$ K is too high to explain in the standpoint of past reports. Thus, to understand the relationship between electronic states and the superconducting mechanism of NaAlSi will open the new way to develop the high T_c superconductor. In addition, recent theoretical study has shown that the electronic structure of NaAlSi shows Dirac nodal line, and this material is the candidate of topological superconductor [2].

Although the superconductivity of this material has been discovered over 10 years ago [3], the electronic structure has not yet been determined experimentally due to the unstable nature of the material under the atmosphere. In this beamtime, we solved this problem by preparing the sample in a glove box, and directly observed the electronic structure of NaAlSi using angle-resolved photoemission spectroscopy (ARPES) using synchrotron radiation.

As a result of the ARPES measurement, the crossing between valence band originating from the Si-2p orbitals and the conduction band originating from the Al-3sp orbitals is occurred, and Dirac nodal line, which predicted by theoretical study, is observed. The valence band has a flat shape near the Fermi level. The result of k_z dependent band dispersion measurement indicates that the electronic structure of NaAlSi showing pseudo two dimensionally (Fig. 1). As shown in Fig. 1, the Fermi wave number k_F is observed only at specific k_z .

We tried to evaluate the superconducting gap in this electronic structure from the synchrotron ARPES measurement in BL5U having low temperature / high resolution measurement system. From the comparison between the leading-edge-midpoint measured at 4 K (superconducting state) and that of 8 K (normal state), the leading-edge-midpoint shift, i.e., superconducting gap is observed at 4 K. This result suggests the possibility of the relationship between unique two-dimensional electronic structure with the dilute carrier state and occurring of the superconductivity in this material.

In future, if the superconducting mechanism and topological states of this material are fixed, we may establish the new standpoint in order to develop the high T_c topological superconductor.

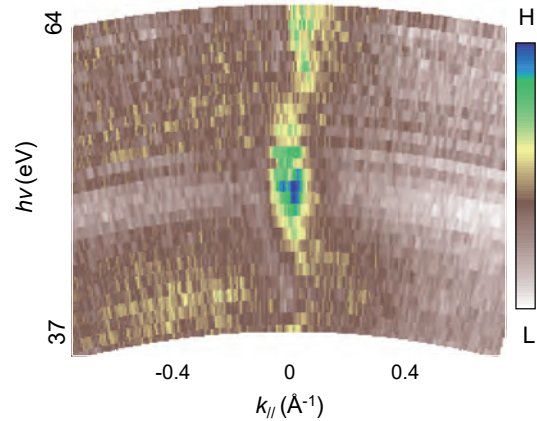


Fig. 1. k_z dispersion around Fermi level of NaAlSi.

- [1] H. B. Rhee *et al.*, Phys. Rev. B **81** (2010) 245114.
[2] L. Jin *et al.*, J. Mater. Chem. **7** (2019) 10694.
[3] S. Kuroiwa *et al.*, Physica C **466** (2007) 11.

BL5U

Demonstration of Final State Effect: Deflector Map in Double Layer Cuprate Bi2212

S. Ideta^{1,2}, S. Ishida³ and K. Tanaka^{1,2}¹National Institutes of Natural Science, Institute for Molecular Science, Okazaki 444-8585, Japan²The Graduate University for Advanced Studies, SOKENDAI, Okazaki 444-8585, Japan³Electronics and Photonics Research Institute, National Institute of Advanced Industrial Science and Technology, Tsukuba 305-8565, Japan

To understand the mechanism of high- T_c superconductivity in cuprates is one of the crucial issues. Angle-resolved photoemission spectroscopy (ARPES) is a powerful tool to investigate the electronic structure of solids directly, and has contributed significantly towards an elucidating of the nature of superconductivity of cuprates [1]. However, ARPES spectrum have a strong constraint of the final state effect arising from especially the energy and polarization of the incident photons [2,3]. In addition, in the conventional ARPES experiment, one needs to rotate samples to obtain the information of momentum space. Recently, deflector mode for mapping has been developed and we do not need to rotate samples. We report that the final state effect using a state of the art ARPES system with a new electron lens with deflectors (MB Scientific AB) in Double-layer Bi-based cuprate superconductor, $\text{Bi}_2\text{Sr}_2\text{Ca}_2\text{CuO}_{8+\delta}$ (Bi2212).

Bi2212 is the one of the most common samples to study the electronic structure using ARPES. Bi2212 has two equivalent CuO_2 planes and therefore shows the bilayer splitting reflecting bonding and anti-bonding bands. In this study, as a first step to elucidate the final state effect using the deflector mode and sample rotation mode, we have investigated the momentum space mapping using the deflector mode on underdoped Bi2212 along the Cu-O and Cu-Cu directions (s polarization).

High-quality single crystals of underdoped $\text{Bi}_2\text{Sr}_2\text{Ca}_2\text{CuO}_{8+\delta}$ (UD Bi2212, $T_c = 65$ K) were grown by the TSFZ method. ARPES experiments were carried out at BL5U of UVSOR-III Synchrotron. Clean sample surfaces were obtained for the ARPES measurements by cleaving single crystals *in-situ* in an ultrahigh vacuum better than 8×10^{-9} Pa. The measurements were performed at 20 K.

In order to estimate the distribution of the spectral weight on momentum space, ARPES experiments have been demonstrated by linearly polarized light and Fermi surfaces (FSs) are observed as displayed in Fig. 1. Figures 1(a) and 1(b) show FSs highlighted by red dots corresponding to the Fermi momentum, k_F , but the experimental momentum cut is along the Cu-O and Cu-Cu directions, respectively. Due to the photon energy, we could not resolve the bilayer splitting in the present study ($h\nu = 60$ eV). From this result, we found that the deflector mode mapping shows a similar FS

reported in previous ARPES study [4-7]. In addition, integrated spectral intensity plotted as a function of FS angle [Figs. 1(c) and 1(d)], and these two experimental geometries have different momentum dependence for the spectral intensity.

As future work, we need to investigate FS mapping using the conventional sample rotation method to compare the spectral weight on momentum space with the result of Fig.1. In addition, we will demonstrate doping dependence and photon energy dependence. These experimental studies will put additional experimental constraint on various microscopic theories and data analysis.

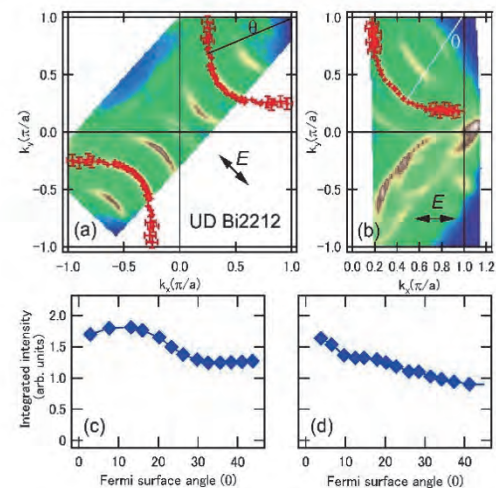


Fig. 1. Momentum-space mappings in underdoped (UD) Bi2212 at energies of -0.01 eV and 0.01 eV ($h\nu = 60$ eV, $T = 20$ K). (a) Mapping along Cu-O direction (nodal direction). (b) Mapping along the Cu-Cu direction (antinodal direction). (c), (d) Spectral intensity integrated by ± 2 degree around k_F is plotted as a function of Fermi surface angle.

- [1] A. Damascelli *et al.*, Rev. Mod. Phys. **75** (2003) 473.
- [2] A. Bansil *et al.*, Phys. Rev. Lett. **83** (1999) 5154.
- [3] D. L. Feng *et al.*, Phys. Rev. B **65** (2002) 220501(R).
- [4] T.-G. Zhong *et al.*, Phys. Rev. B **98** (2018) 140507(R).
- [5] J. D. Rameau *et al.*, Phys. Rev. B **90** (2014) 134509.
- [6] K. Tanaka *et al.*, J. Phys. Soc. Jpn. **88** (2019) 044710.
- [7] P. B. Bogdanov *et al.*, Phys. Rev. Lett. **89** (2002) 167002.

BL5U

Polarization Dependence of the Photoelectron Intensity Distribution from MoS₂

 S. Tanaka¹, K. Ueno², S. Ideta³ and K. Tanaka³
¹The institute of Scientific and Industrial Research, Osaka Univ., Ibaraki 567-0047, Japan

²Graduate School of Science and Engineering Saitama University, Saitama 338-8570, Japan

³UVSOR Synchrotron Facility, Institute for Molecular Science, Okazaki 444-8585, Japan

The photoelectron intensity in the angle-resolved photoelectron spectroscopy (ARPES) is determined by the Fermi's golden rule, where the matrix element $\langle \varphi_f | \mathbf{A} \cdot \mathbf{p} | \varphi_i \rangle$ plays a crucial role. In the matrix element, $\langle \varphi_f |$ denotes the final state which is approximately the plane wave; $\mathbf{A} \cdot \mathbf{p}$ corresponds to the photoexcitation Hamiltonian and \mathbf{A} and \mathbf{p} respectively denote the vector potential of the photon and the momentum of the electron. We can change \mathbf{A} by controlling the polarization of the photon, and detailed electronic properties of the initial state $|\varphi_i\rangle$ can be investigated by the polarization-dependent photoelectron intensity distribution.

For this purpose, we made an investigation for the band at the top of the valence band in MoS₂, which is mainly constructed from the Mo-4d and S-3p orbitals. Figures 1 show the constant energy maps at the binding energy of 0.77 eV taken at $h\nu=60$ eV. The polarizations of the incident photons are linearly horizontal (i.e., p-pol), linearly vertical (i.e., s-pol), circularly right-handed (CW), and circularly left-handed (CCW). The band forms a circular shape around the Γ -point. This means that the operation of rotation for the wavefunction does not change the energy (the eigenvalue of the Hamiltonian), and the angle around the Γ -point is a good quantity for describing the system. The photoelectron intensity distributions are drastically changed with changing the polarization. The intensity distributions as functions of the azimuthal angle are displayed after expanding by repeating the signals as the period of 2π in Figs. 2. The distribution taken with the vertical polarized light shows a complete different one from the other three. The horizontal, CW, and CCW polarizations yield the distribution of nearly the same form $I_0 \cos^2\left(\frac{\theta - \theta_0}{2}\right)$, although the phases are shifted as changing the polarization. The phase-shift in the photoelectron intensity distribution with changing the photon polarization was reported for the Dirac cone of the graphene, where the "Berry's phase" of the wavefunction in the Dirac cone plays a key role [1]. Accordingly, an important information about the wavefunction of the valence band MoS₂ will be given. Theoretical investigation and more detailed analysis are in progress.

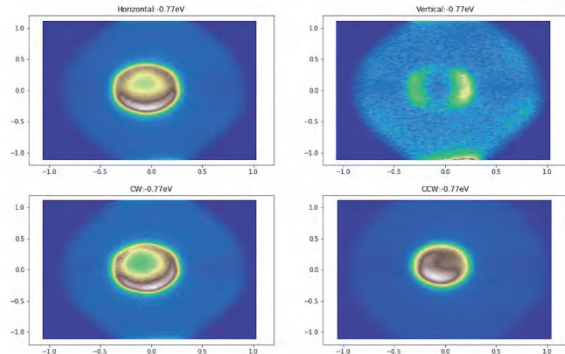


Fig. 1. Polarization-dependent photoelectron intensity map at the binding energy of 0.77 eV near the Γ -point of MoS₂.

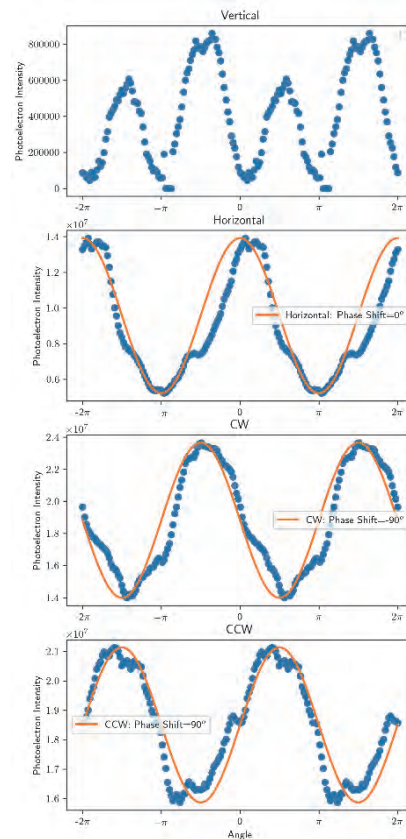


Fig. 2. Photoelectron intensity distribution at the binding energy of 0.8 eV as a function of the angle around the Γ -point of MoS₂. Solid lines show $I_0 \cos^2\left(\frac{\theta - \theta_0}{2}\right)$, where θ_0 is the phase-shift.

[1] Y. Liu *et al.*, Phys. Rev. Lett. **107** (2011) 166803.

BL5B

Study on Optical Properties of Metallic Sodium by Vacuum Ultra Violet in UVSOR (2)

M. Kawaguchi^{1,2}, J. Saito¹, H. Daido³ and T. Suemoto⁴

¹Sodium Technology Development Group, Japan Atomic Energy Agency, Tsuruga 919-1279, Japan

²Research Institute of Nuclear Engineering, University of Fukui, Tsuruga 914-0055, Japan

³Institute for Laser Technology, Suita 565-0871, Japan

⁴Toyota Physical and Chemical Research Institute, Nagakute 480-1192, Japan

Metallic sodium is well-known as a typical alkali metal, but the optical properties in vacuum ultraviolet (VUV) range are controversial [1,2]. One of the authors (H. D.) demonstrated VUV light (Wave length: 115-180 nm) penetrates in several millimeters of sodium with high transmittance for the first time [3]. Inspired by the experiment, the transmittance measurement of metallic sodium using VUV has been performed at BL5B in UVSOR [4]. In this year, we adopted calcium fluoride (CaF₂, Pier Optics Co, ltd.) for windows of the sodium sample (Diameter: 18 mm^φ, Thickness: 2.0 mm^t) to decrease interaction between the sodium and the windows, which were seemed to be one of significant causes of decreasing drastically the transmittance.

Figure 1 shows intensities of 0th light, 1st light and transparent VUV, which denote the raw light radiated from UVSOR, the light passed through lithium fluoride (LiF) filter, and the transparent light passed through the LiF filter and the CaF₂ windows, respectively. Because of the band gaps, the LiF and the CaF₂ can be transparent to more than about 100 nm and about 120 nm in wave length, respectively. Therefore, the intensities of the 1st light and the transparent VUV show the stepwise increases in the characteristic wave lengths, which are corresponded to those of the LiF and the CaF₂. Figure 2 shows the transmittance of the CaF₂ windows, which was obtained by dividing the intensity of the transparent VUV by that of the 1st light. In this calculation, the 0th light can't be used because it includes the short-range wave-length light. The measured transmittance of CaF₂ windows is almost consistent with the literature datum [5], and it concluded that there were no problems in the transmittance measurement and CaF₂ windows.

However, the transparency phenomenon of VUV in the metallic sodium has never been confirmed by our group. Because the reaction (deterioration) of the sodium on the surface of the windows proceeded gradually and the products might hinder the transparency of VUV, we need to improve the technique of making the sodium sample.

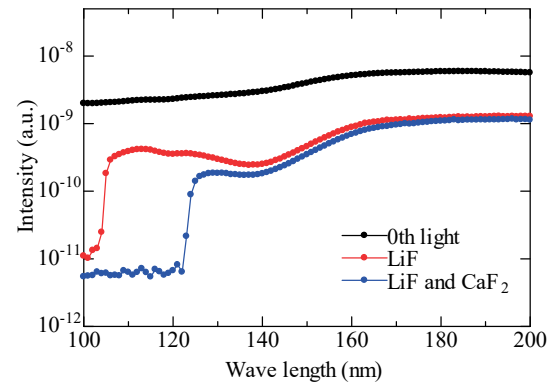


Fig. 1. Intensities of 0th light at BL5B and of lights through LiF and CaF₂ windows (2mm^t), and transmittance of CaF₂ window.

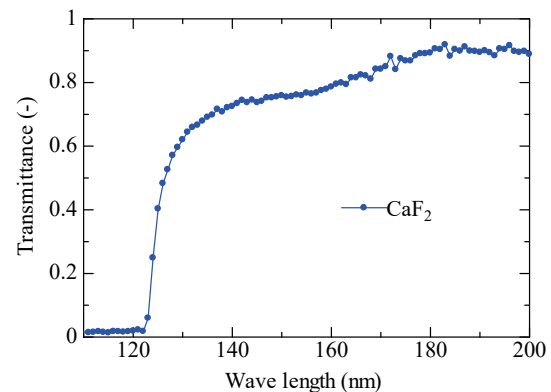


Fig. 2. Transmittance of CF₂ windows

- [1] J. C. Sutherland *et al.*, Optical properties of sodium in the vacuum ultraviolet (ORNL-TM-1776, Oak Ridge National Laboratory, 1967).
- [2] R. W. Wood, Phys. Rev. **44** (1933) 353.
- [3] H. Daido *et al.*, Optics express **21** (2013) 28182.
- [4] M. Kawaguchi, J. Saito, H. Daido and T. Suemoto, UVSOR Activity Report 2018 **46** (2019) 89.
- [5] <http://www.pier-optics.com/transparent.html>

BL6U

Temperature-dependent Electronic Structure of a Quasi-2D Material η -Mo₄O₁₁

 T. Kobayashi¹, E. Iwamoto², K. Sakamoto², M. Koyano³, F. Matsui⁴ and S. Suga⁵
¹Department of Material and Life Science, Osaka University, Suita 565-0871, Japan

²Department of Applied Physics, Osaka University, Suita 565-0871, Japan

³School of Materials Science, Japan Advanced Institute of Science and Technology, Nomi 923-1292, Japan

⁴UVSOR Synchrotron Facility, Institute for Molecular Science, Okazaki 444-8585, Japan

⁵Institute of Scientific and Industrial Research, Osaka University, Ibaraki 567-0047, Japan

Angle resolved photoelectron spectroscopy (ARPES) with extremely high resolutions in both energy and momentum is indispensable to obtain detailed understanding of various phenomena in condensed matters physics, such as charge density wave (CDW), Rashba effect, properties of topological materials, and so on. These kind of studies may be effectively performed by momentum microscopy (MM) in the near future.

In order to check the performance of the beam line BL6U, where the MM is planned to be setup, we have measured the electronic structure of a quasi-2D material η -Mo₄O₁₁ at different temperatures. By performing electrical resistivity measurements, η -Mo₄O₁₁ has been reported to show transitions at $T_{c1}=109$ K and $T_{c2}=30$ K that are very likely due to CDW instabilities [1]. However, neither band gap opening nor band folding, which should be present in case of CDW transition, has been observed in the former ARPES study [2]. In the present study, we performed ARPES measurements at temperatures above and below the two CDW transitions to obtain more detailed information on the property of this material.

Figure 1 shows the Fermi surface of η -Mo₄O₁₁ measured at 8.6 K. Straight lines indicating the presence of three 1D metallic bands in different direction are clearly observed. The observation of three 1D metallic bands is consistent with that reported in Ref. [2] but not with the electrical resistivity measurements [1] since the measurement temperature in Fig. 1 is lower than T_{c2} . The Fermi wave number of the metallic bands are ca. 35 % of the Brillouin zone. In Fig. 2, we show the energy distribution curves (EDC) measured at $T>T_{c1}$ (300 K), $T_{c1}>T>T_{c2}$ (60 K), and $T_{c2}>T$ (8.6 K). As well as the result in Fig. 1, no trace of CDW transition can be confirmed in Fig. 2. The peak just below the Fermi level shift a bit to lower binding energy and becomes shaper as the temperature decreases. The energy shift and the change in the Fermi wave vector (not shown) indicate hole-doping during the cooling. The closer the Fermi surface is to the half of the Brillouin zone the more likely the CDW transition occurs. In the present case, the Fermi surface is much smaller than the half of the Brillouin zone and thus the metallic behavior at all temperatures might be resulting from the hole-doping induced by the residual gas adsorption.

Since the in situ cleavage was successful to provide single crystal domains of the order of sub-mm, and because very complex band structures were detected in the present study, η -Mo₄O₁₁ would be a suitable material for checking the performance of the MM in the near future.

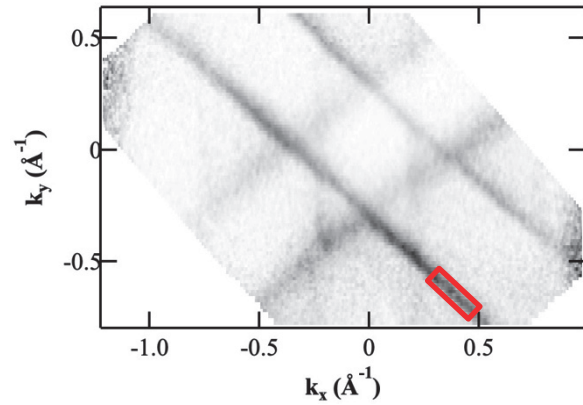


Fig. 1. Fermi surface of η -Mo₄O₁₁ measured at 8.6 K.

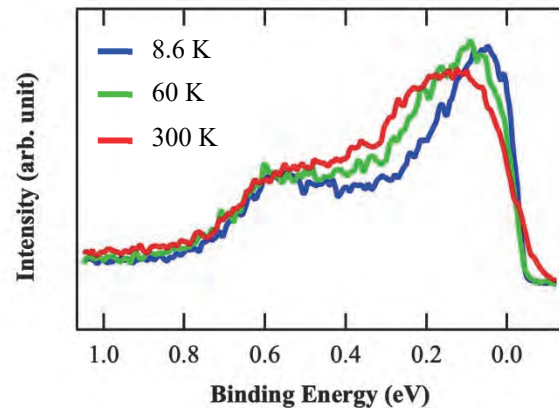


Fig. 2. EDC spectra obtained by integrating the data surrounded by the red rectangle shown in Fig. 1.

[1] H. Guyot *et al.*, J. Phys. C **16** (1983) L1227.

[2] G.-H. Gweon *et al.*, Phys. Rev. B **72** (2005) 035126.

BL6U

Angle-Resolved Photoemission Spectroscopy of Topological Insulators for Clarification of Origin of Pressure-Driven Superconductivity

Y. Kubozono¹, R. Eguchi¹, H. Goto¹, T. He¹, K. Kobayashi¹, T. Takahashi¹,
H. Ozaki², K. Hayashi² and F. Matsui³

¹Research Institute for Interdisciplinary Science, Okayama University, Okayama 700-8530, Japan

²Nagoya Institute of Technology, Nagoya 466-8555, Japan

³Institute for Molecular Science, Okazaki 444-8585, Japan

Two-dimensional angle-resolved photoelectron spectroscopy (ARPES) is a powerful tool to study the electronic structure of crystalline materials, in particular the unique electronic structures of topological materials such as topological insulators, Dirac / Weyl semimetals, and axion insulators have been extensively investigated during a past decade. The initial state binding energy (E) and the wave vector (\mathbf{k}) can be easily determined from the kinetic energy and the direction of the detected ARPES data. Some of topological insulators such as $\text{Bi}_{2-x}\text{Sb}_x\text{Te}_{3-y}\text{Se}_y$ [1] and Sr or Ag doped Bi_2Se_3 [2,3] provided the pressure-driven superconducting phases.

To understand the correlation between the electronic property and pressure-driven superconductivity, we must obtain the detailed information of electronic structures of topological insulators at ambient pressure. Admittedly, in case of $\text{Bi}_{2-x}\text{Sb}_x\text{Te}_{3-y}\text{Se}_y$, the Fermi level and Dirac point significantly shifted against x and y [4]. Therefore, the superconductivity of topological insulators induced by pressure must be investigated by associating exactly with their electronic structures, as well as with the structural transitions. In addition, the superconducting gap function (Cooper pair symmetry) of pressure-driven superconductivity in topological insulators must be clarified to show the topologically non-trivial nature of superconductivity, which requires the exact information of electronic structures at ambient pressure. For these purposes, the study on electronic structure by ARPES is indispensable for topological insulators. In this study, we measured the ARPES data of Ag doped Bi_2Se_3 ($\text{Ag}_x\text{Bi}_{2-x}\text{Se}_3$; $x = 0.05$), Nb doped Bi_2Se_3 ($\text{Nb}_x\text{Bi}_{2-x}\text{Se}_3$; $x = 0.5$), $\text{Bi}_{2-x}\text{Sb}_x\text{Te}_{3-y}\text{Se}_y$ ($x = 1.0$, $y = 2.0$) and those precursor sample, Bi_2Se_3 using the MBS A-1 Lens#5 analyzer installed at BL6U.

We measured the ARPES data of the non-doped Bi_2Se_3 single crystal recorded at room temperature. A clear band dispersion showing a single Dirac cone, and conduction / valence bands was recorded as previously reported [5]. This means that the measurement system is available for detecting the exact information of electronic structures of topological insulators.

We measured the ARPES of $\text{Ag}_x\text{Bi}_{2-x}\text{Se}_3$ ($x = 0.05$) single crystal at 10 K. At the present stage, the ARPES of $\text{Ag}_x\text{Bi}_{2-x}\text{Se}_3$ was not distinguished from that of Bi_2Se_3 , *i.e.*, the Ag doping was ambiguous. The reason is not clear, but one possibility that the cleaved surface of single crystal of $\text{Ag}_x\text{Bi}_{2-x}\text{Se}_3$ might not include Ag atom was suggested. In other words, the area where no

Ag atoms are included may be selectively cleaved in the $\text{Ag}_x\text{Bi}_{2-x}\text{Se}_3$ crystal.

Moreover, we measured the ARPES of $\text{Nb}_{0.5}\text{Bi}_2\text{Se}_3$. A clear superconducting transition at ~ 3 K was observed in the magnetic susceptibility for this material. Figure 1 shows the band dispersion of $\text{Nb}_{0.5}\text{Bi}_2\text{Se}_3$ measured at 10 K. Fermi energy is 55.5 eV in kinetic energy. A single Dirac cone and the top of the valence band were observed.

Now, we are trying to measure the ARPES of new topological insulators which was recently found to show the pressure-driven superconductivity.

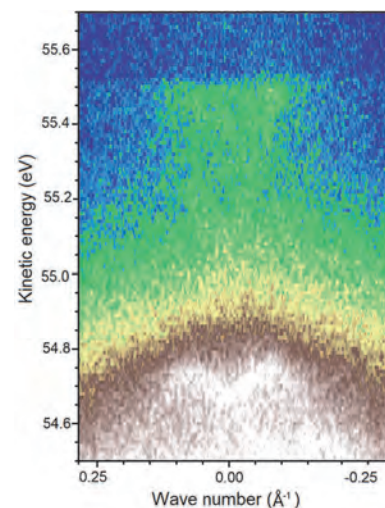


Fig. 1. Band dispersion of $\text{Nb}_{0.5}\text{Bi}_2\text{Se}_3$.

- [1] T. He *et al.* Phys. Rev. B **100** (2019) 094525.
- [2] Y. Zhou *et al.* Phys. Rev. B **93** (2016) 144514.
- [3] T. He *et al.* Phys. Rev. B **97** (2018) 104503.
- [4] T. Arakane *et al.* Nature Commun. **3** (2012) 636.
- [5] Y. L. Chen *et al.* Science **329** (2010) 659.

BL6U

Photon-energy-dependence in the Photoelectron Angular Distribution from MoS₂

 S. Tanaka¹, K. Ueno², H. Matsuda³ and F. Matsui³
¹The Institute of Scientific and Industrial Research, Osaka Univ., Ibaraki 567-0047, Japan

²Graduate School of Science and Engineering Saitama University, Saitama 338-8570, Japan

³UVSOR Synchrotron Facility, Institute for Molecular Science, Okazaki 444-8585, Japan

2H-MoS₂ is one of the most typical transition metal dicalchogenides, and its electronic property is a fundamental issue for the fabrication of new functional low-dimensional electronic devices. In this report, we show a comparison in the momentum space between the ARPES measurement by using photons in the wide energy range (60-200 eV) and the DFT-calculation to demonstrate the validity of the photon-energy-dependent ARPES for identifying the characterization of the valence band of the materials.

The ARPES measurements were carried out at the room temperature, and the DFT calculation was made employing the QUANTUM ESPRESSO package (version 6.3), which had been installed in the computer at Research Center for Computational Science in IMS. Figures 1 show a part of the series of the photon-energy-dependence in the photoelectron angular distribution from MoS₂ at the same binding energy (1.8 eV). The first Brillouin zones are indicated as black lines. Shapes clearly change as a function of the photon energy; at 73-93 eV and 149 eV, a hexagon consisting of small triangles is shown; at 113 eV, a smaller hexagram is shown; and at 103 eV, both are shown. This behavior is not consistent with the calculated k_z value (not shown here), and thus cannot be interpreted to the dispersion along the k_z axis. Instead, this can be ascribed to the character of the band. Figures 2 show the calculated projected density of states for the Mo-4d and S-3p orbitals in the momentum space at the binding energy of -1.2 eV. The binding energy for the calculation was chosen so as to display shapes similar to the experiments. The discrepancy of 0.6 eV may partly be to the difference in the reference (in the ARPES, it is the Fermi level measured by using Au film, and in the DFT calculation it is the valence band maximum). It is clear that ARPES results at photon energies of 73-93 eV resembles to the band provided by Mo-4d while the hexagram shape obtained by ARPES at 103-113 eV resembles to the band of S-3p. Figure 3 shows the photoexcitation cross section of the atomic orbitals. The photoexcitation cross section of Mo-4d is higher than S-3p in the photon energy regions below ~70 eV and above ~170 eV. Although the crossing point at ~70 eV in Fig. 3 is significantly lower than ~100 eV which is derived from Figs. 1, a general trend shows a good agreement, and thus the characteristics of the band is well explained. More detailed analyses are in progress.

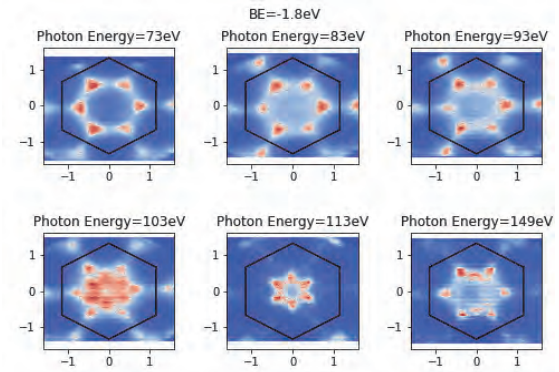


Fig. 1. Photoelectron angular distributions of the same binding energy from MoS₂ at various photon energies.

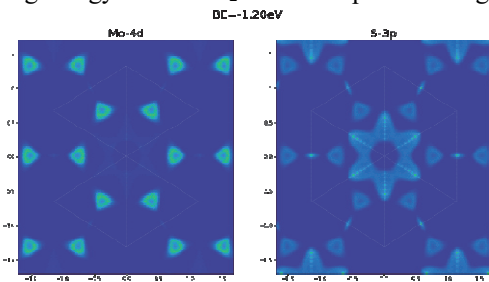


Fig. 2. Calculated density of states at BE=-1.2 eV which are projected into the Mo-4d and S-3p orbitals

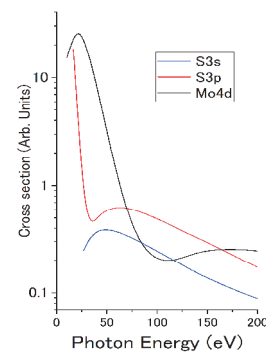


Fig. 3. Photoexcitation cross sections of S3s, S3p and Mo4d atomic orbitals [1].

[1] J. J. Yeh *et al.*, *At. Data Nucl. Data Tables* **32** (1985) 1.

BL6U

Anisotropy of Photoelectron Intensity Distribution upon Hole-Vibration Coupling in Perfluoropentacene Monolayer on Ag(111)

Y. Hasegawa¹, K. Maduwantha², R. Koswattage², T. Nakamura³, F. Matsui⁴ and S. Kera^{1,4}

¹Department of Photo-Molecular Science, Institute for Molecular Science, Okazaki 444-8585, Japan

²Sabaragamuwa University of Sri Lanka, Belihuluoya 70140, Sri Lanka

³Department of Physics, Graduate School of Science, Osaka University, Toyonaka 560-0043, Japan

⁴UVSOR Synchrotron Facility, Institute for Molecular Science, Okazaki 444-8585, Japan

Organic semiconductor thin films have been getting attention as next promising optical and electronic devices. Optimizing charge transfer between weakly connected materials is one of a key issue to improve the performance. Considering the charge transfer is affected by the coupling of the charge to specific vibrational modes of molecules, the impact of anisotropic deformation of a molecule upon ionization at the interface on the transfer efficiency should be investigated.

We have found perfluoropentacene (PFP) monolayer on inert crystalline substrate shows hole-vibration coupling upon angle-resolved ultraviolet photoelectron spectroscopy (ARPES) measurement and distinct angular distribution of highest occupied molecular orbital (HOMO) features depending on the vibronic couplings [1]. To address the origin of the photoelectron intensity distribution of the vibronic states, a precise experiment of the photoelectron momentum map (PMM) was carried out to evaluate the intensity modulation.

PFP monolayer of 2.5 Å was deposited onto a clean Ag(111) substrate. Low energy electron diffraction (LEED) and PMM were carried out at the sample temperature of 16 K. PMM was taken by means of acceptance-cone-tunable spectrometer equipped with A-1 analyzer (MBS) which enables mechanical deflector scan. Detail of the setup is reported elsewhere [2].

ARPES measurement of PFP monolayer on Ag(111) shows HOMO with fine structure, a main peak of HOMO, labeled H(00), followed by the vibrational progression of satellite peaks toward higher binding energy. Figures 1(a) and (b) are PMM taken from H(00) and the first satellite, H(01), respectively. The PMMs correspond to the photoelectron intensity integrated for the two different domains, where the molecular arrangements of A and C are shown in Fig. 1 (c). Note the one from arrangement A is marked by dashed oval. Figure 2 shows the line profiles of the PMMs taken from k_1 and k_2 direction marked by dashed and solid allows in Fig. 1, respectively. In direction of k_2 subtle difference of the intensity between H(00) and H(01) is observed whereas little difference is evaluated in direction of k_1 . This observation indicates that the nuclei position is not fixed during the photoionization process as found in gas-phase system, meaning the breaking of sudden approximation in the thin film. Moreover the wavefunction of the molecular orbital is modulated only in a certain direction upon a specific hole-vibration

coupling, thus designing a distortion of the molecular structure in real space upon ionization would be important to control device characteristics. The correlation between the distortion of the molecule upon vibronic excitation and the PMM would be further discussed beyond Franck-Condon approximation.

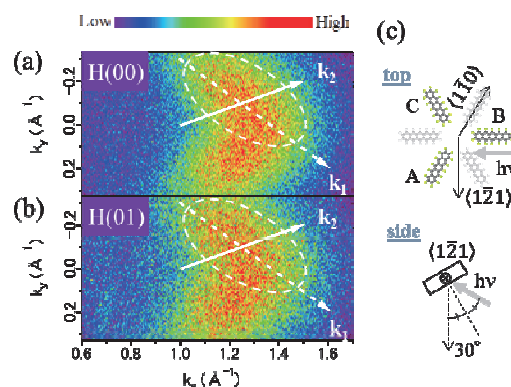


Fig. 1. PMM image taken at the HOMO of the (00) and (01) peaks ($\Delta E \sim 50$ meV) of PFP/Ag(111) with $h\nu = 50$ eV. The color scaling and intensity are normalized at maximum intensity. (c) Geometry for the measurement.

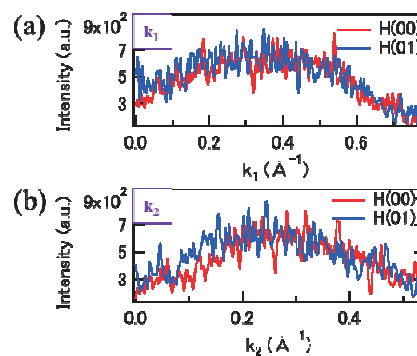


Fig. 2. Line profiles taken from H(00) and H(01) indicated by white arrows, (a) k_1 and (b) k_2 in Figs. 1(a) and (b), respectively. Origins of k_1 and k_2 in (k_x, k_y) are (1, -0.3) and (1.0, 0.0), respectively.

- [1] S. Kera *et al.*, Prog. Surf. Sci. **84** (2009) 135.
 [2] H. Yamane *et al.*, Rev. Sci. Instrum. **90** (2019) 093102.

BL6B, BL7B

Anisotropic Metal-Insulator Transition in RuAs

Y. Nakajima¹, Z. Mita², H. Watanabe^{2,1}, Y. Ohtsubo^{2,1}, T. Ito^{3,4}, H. Kotegawa⁵, H. Sugawara⁵, H. Tou⁵ and S. Kimura^{2,1}

¹Department of Physics, Graduate School of Science, Osaka University, Toyonaka 560-0043, Japan

²Graduate School of Frontier Biosciences, Osaka University, Suita 565-0871, Japan

³Nagoya University Synchrotron Radiation Research Center, Nagoya University, Nagoya 464-8603, Japan

⁴Graduate School of Engineering, Nagoya University, Nagoya 464-8603, Japan

⁵Department of Physics, Graduate School of Science, Kobe University, Kobe 657-8501, Japan

Ruthenium mono-antimonide, RuAs, which is one of related materials to iron-pnictide superconductors, shows a metal-to-insulator (MIT) transition accompanied with structural change [1]. The metallic character at room temperature changes to an insulating one detected by an electrical resistivity measurement [2] through a two-step structural phase transition at about 250 K (T_{M1}) and about 200 K (T_{M2}). The orthorhombic crystal structure with space group $Pnma$ at room temperature changes to the formation of a $3 \times 3 \times 3$ superlattice of the original unit cell of the monoclinic structure with space group $P2_1/c$ below T_{M2} . However, the origin of the two-step phase transition has not been clarified yet because the intermediate phase at temperatures between T_{M1} and T_{M2} has not been identified. So, to clarify the change of the electronic structure due to the two-step phase transition, we measured temperature-dependent polarized optical conductivity [$\sigma(\omega)$] spectra and revealed the anisotropic change of the electronic structure.

Optical reflectivity [$R(\omega)$] spectra as well as $\sigma(\omega)$ spectra of single-crystalline RuAs samples, with the largest size of about $0.1 \times 0.5 \times 0.2$ mm³, were measured along the b and c axes in the photon energy range from 15 meV to 30 eV to ensure an accurate Kramers-Kronig analysis (KKA). Infrared (IR) and terahertz (THz) measurements at the photon energy regions of 15 meV to 1.5 eV have been performed using conventional reflectivity measurement setups and IR and THz microscopes at BL6B. In the photon energy range of 1.2–30 eV, the $R(\omega)$ spectrum was measured only at 300 K at BL7B for accurate KKA.

Figure 1 shows the temperature dependence of the $\sigma(\omega)$ spectra at around 200 K ($\sim T_{M2}$), where large spectral change is expected. In $E // b_H$, which is the b axis above T_{M2} , the spectrum changes little above 200 K, but below the temperature, the intensity at ~ 0.1 eV decreases, and that at about 0.16 eV increases, suggesting the appearance of an energy gap. At 160 K, the energy gap structure becomes recognized spectrum at 210 K slightly changes from that at 230 K, where clearly, as shown in Fig. 1. On the other hand, in $E // c_H$, the spectrum at 210 K slightly changes from that at 230 K where the intensity below (above) 0.22 eV decreases (increases). The change becomes clearer with decreasing temperature, which indicates the energy gap opening. These results imply that the spectral change in

$E // b_H$ starts at $T \lesssim 210$ K, but that in $E // c_H$ gradually occurs between 210 and 230 K. This suggests that the temperature of the $\sigma(\omega)$ spectral change as well as the change of the electronic structure is anisotropic, i.e., the change along the b_H (c_H) axis occurs at lower (higher) temperature. The anisotropic change of the electronic structure is considered to be the origin of the two-step phase transition [3].

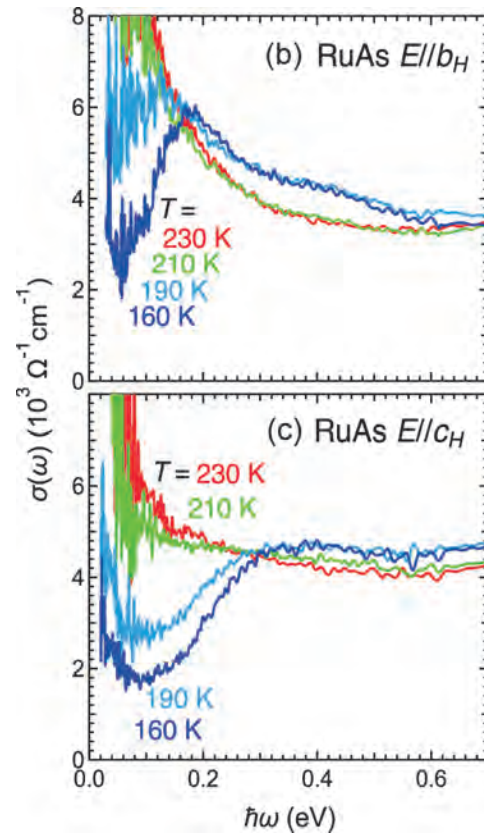


Fig. 1. Temperature-dependent polarized $\sigma(\omega)$ spectra of RuAs in $E // b_H$ and $E // c_H$ near the first-order phase transition temperature of ~ 200 K (T_{M2}).

[1] D. Hirai *et al.*, Phys. Rev. B **85** (2012) 140509(R).

[2] H. Kotegawa *et al.*, Phys. Rev. Mater. **2** (2018) 055001.

[3] Y. Nakajima *et al.*, Phys. Rev. B **100** (2019) 125151.

BL6B

Infrared Reflectivity Spectrum for Au-codoped Mg₂Si:Bi Crystal

T. Tanimoto¹, M. Kitaura², H. Udono³ and A. Ohnishi²

¹Graduate school of Science and Engineering, Yamagata University, Yamagata 990-8560, Japan

²Faculty of Science, Yamagata University, Yamagata 990-8560, Japan

³Department of Electrical and Electronics Engineering, Ibaraki University, Hitachi 316-8511, Japan

Mg₂Si is a thermoelectric material with high figure of merit ZT . This material is composed of nontoxicity and abundant elements, and attract much attention as a KANKYO semiconductor [1]. The value of ZT is generally influenced by the carrier concentration. The increase in carrier concentration is mainly caused by impurity doping. The effect of such impurity doping on thermoelectric properties of Mg₂Si has been studied so far. The Bi atom is known as an effective element for electron doping in Mg₂Si. The electronic structure of Bi-doped Mg₂Si (Mg₂Si:Bi) has been studied [2]. Recently, it was reported that the carrier concentration above 10^{20} cm^{-3} is attained by multiple impurity doping [3]. On the other hand, the effect of impurity codoping on the carrier concentration has not yet been reported for Mg₂Si:Bi.

In the present study, the effect of Au codoping on the carrier concentration in Mg₂Si:Bi was investigated. In this work, infrared reflective spectra were measured at 300 K to determine the carrier concentration of an Au-codoped Mg₂Si:Bi crystal. In n-type semiconductors, infrared reflectivity spectra exhibit the structure due to the plasma reflection, which arises from collective excitation of free electrons [4]. The carrier concentration can be determined by analyzing the plasma reflection.

Au-codoped Mg₂Si:Bi crystals were grown from the melt by the Bridgeman method. Infrared reflectivity spectra were obtained using a FT-IR spectrometer at the beamline BL6B. The infrared reflectivity spectra were analyzed using the software RefFit [5]. The parameters of the plasma frequency ω_p , dielectric constant ϵ_∞ , and damping constant Γ_p were determined by the fit of the Drude-model to the experimental data. Using these parameters, the carrier concentration N and relaxation time τ were also determined, and was compared to that determined by the Hall effect experiment.

Generally, it is hard to determine the absolute reflectivity correctly, because the absolute reflectivity is sensitive to roughness and contamination of the crystal surface. The absolute reflectivity was corrected using the refractive index and dielectric constant at 5000 cm^{-1} in the transparent region [4,6]. The infrared reflectivity spectrum for an Au-codoped Mg₂Si:Bi crystal, thus obtained, is shown in Fig. 1. The reflectivity spectrum exhibits a dip around 1100 cm^{-1} . The reflectivity is rapidly increased with decreasing wavenumber. This feature is explained as so-called Drude-like behavior. The reflectivity spectrum is almost agreement to the result of the curve fit analysis. The parameters obtained are listed in Table 1. The values of N and τ determined

were also listed in Table 1. The value of N is approximately consistent with that ($=5.0 \times 10^{19} \text{ cm}^{-3}$) determined by the Hall effect experiment. On the other hand, the value of τ is larger than those in Ref. [3]. It is known that τ becomes small with increasing N . The value of N in our sample is one-order magnitude smaller, compared to those in Ref. 3. It is thus reasonable to attribute the difference in τ to that in N . The analysis of the infrared reflectivity spectrum apparently gives reasonable physical parameters dominating electric properties of n-type Mg₂Si.

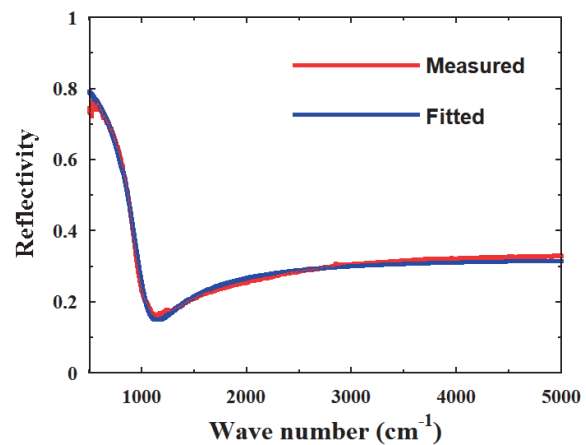


Fig. 1. Infrared reflective spectrum for an Au-codoped Mg₂Si:Bi crystal. Red and blue lines indicate the experimental data and the fit curve, respectively.

Table 1. Summary of the parameters in Drude-model, determined from the curve fit analysis.

$\omega_p(\text{cm}^{-1})$	$\Gamma_p(\text{cm}^{-1})$	$\tau(\text{s})$	$N(\text{cm}^{-3})$
1026.2	310.1	1.1×10^{-13}	1.3×10^{19}

- [1] K. Kambe *et al.*, J. Electron. Mater. **43** (2014) 2212.
- [2] N. Farahi *et al.*, Dalton Trans. **43** (2014) 14983.
- [3] J. Zhao *et al.*, J. Mater. Chem. A. **39** (2015) 19774.
- [4] D. McWilliams *et al.*, Phys. Rev. **130** (1963) 2248.
- [5] A. B. Kuzmenko, Rev. Sci. Instrum. **76** (2005) 083108.
- [6] D. McWilliams *et al.*, J. Opt. Soc. Am. **53** (1963) 298.

BL7U

d_{xy} Orbital Character of Hole Bands in $\text{NdFeAs}_{1-x}\text{P}_x\text{O}_{0.9}\text{F}_{0.1}$ Observed by Angle Resolved Photoemission Spectroscopy

 Z. H. Tin¹, T. Adachi¹, A. Takemori¹, S. Miyasaka¹, S. Ideta^{2,3}, K. Tanaka^{2,3} and S. Tajima¹
¹Department of Physics, Osaka University, Osaka 560-0043, Japan

²UVSOR Synchrotron Facility, Institute for Molecular Science, Okazaki 444-8585, Japan

³School of Physical Sciences, The Graduate University for Advanced Studies, SOKENDAI, Okazaki 444-8585, Japan

The iron-based superconductors (IBSs) has provided us new opportunity to investigate the unconventional superconductivity (SC). Among various systems of IBSs, 1111 system has highest T_c . In this 1111 system, however, it is difficult to synthesize the single crystals with high quality, and there are a few reports for study of angle resolved photoemission spectroscopy (ARPES). In this system, the electronic structure (Fermi surfaces (FSs)) can be controlled by the phosphorus doping on the arsenide site. Our previous result indicated that there are two superconducting states in $\text{NdFeAs}_{1-x}\text{P}_x\text{O}_{0.9}\text{F}_{0.1}$ and the critical P concentration is $x \sim 0.2$ [1]. The previous result of ARPES using the p -polarization configuration shows that FS topology is changed by P doping at the same value of $x=0.2$ [2]. Theoretical investigation predicted that the hole pocket with xy orbital character is important in realizing high- T_c SC, but the hole bands with this orbital character have not been observed in our previous work [2,3]. In order to clarify the origin of FS topology change and the relationship between the xy hole band and high T_c , we perform the ARPES measurements on the single crystals of $\text{NdFeAs}_{1-x}\text{P}_x\text{O}_{0.9}\text{F}_{0.1}$ ($x=0$ and 0.2).

The ARPES was measured at 10K. ($T_c=43$ K and 24 K for $x=0$ and 0.2 , respectively.) In the present work, the Fe-Fe direction of the single crystal is parallel to the analyzer slit of detector. The photoenergy of incident light was 18eV for high energy resolution, and the s -polarization configuration was used to detect the xy/yz orbital character bands around the Brillouin zone center.

As shown in Fig. 1, we observed the yz band (green dotted line) in $\text{NdFeAsO}_{0.9}\text{F}_{0.1}$. In addition, we have observed other hole band below -50 meV, which we assign to γ band. This hole band should have the xy orbital character, since there should be only one band with the yz character in the result of the theoretical calculation. This γ band may play an important role in full-gapped s_{\pm} wave symmetry based on spin-fluctuation theory. However, this band does not cross Fermi level. Interestingly, the small flat band appears at zone center around the binding energy of -18 meV. This flat band may also have xy character.

In $x=0.2$ sample, the similar band dispersion has been observed. As shown in Fig. 2, this compound has 3 hole bands around zone center, and the energy levels of γ and flat bands are slightly different from those in $x=0$. The γ band shifts down by 10 meV with P doping, while the flat band shift upward by 6 meV. This behavior can be explained by the sensitivity of γ band to the structural

parameter, h_{pn} and α . The h_{pn} (α) decreases (increases) with phosphorus doping. Our result is consistent with the shift down of γ band with decreasing h_{pn} . On the other hand, the flat xy band near Fermi level overlaps with the top of the xz hole band, which shows the systematic energy shift with P doping [2]. The present results suggested that the yz/xz band splitting is induced by the mixing of xy/xz orbital characters on the top of the hole band.

Finally, a suspicious intensity enhancement is observed on this flat band below T_c . This suggests that the flat band is related to the high- T_c SC. We need further investigation to clarify this mixing xy orbital character on the flat band.

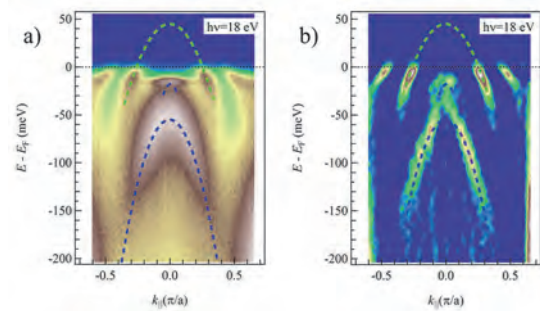


Fig. 1. ARPES results of $\text{NdFeAsO}_{0.9}\text{F}_{0.1}$ around zone center. The ARPES intensity plot (a) and its 2nd derivative plot (b) with respect to k , respectively.

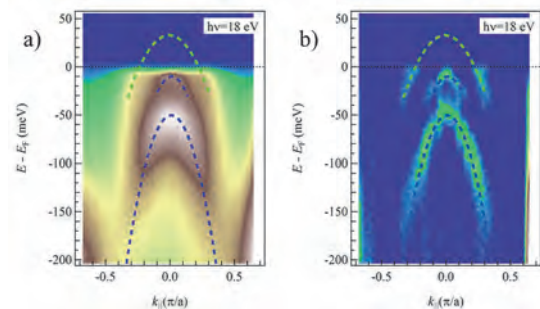


Fig. 2. ARPES results of $\text{NdFeAs}_{0.8}\text{P}_{0.2}\text{O}_{0.9}\text{F}_{0.1}$ around zone center. The ARPES intensity plot (a) and its 2nd derivative plot (b) with respect to k , respectively.

[1] S. Miyasaka *et al.*, J. Phys. Soc. Jpn. **82** (2013) 124706.

[2] A. Takemori *et al.*, Phys. Rev. B **98** (2018) 100501(R).

[3] K. Kuroki *et al.*, Phys. Rev. B **79** (2009) 224511.

BL7U

High-resolution ARPES Study of High-temperature Iron-based Superconductor Fe(Se,Te)

K. Nakayama¹, R. Tsubono¹, Y. Kubota¹, F. Nabeshima², T. Ishikawa², T. Shikama²,
A. Maeda², T. Takahashi^{1,3,4} and T. Sato^{1,3,4}

¹Department of Physics, Tohoku University, Sendai 980-8578, Japan

²Department of Basic Science, the University of Tokyo, Tokyo 153-8902, Japan

³Center for Spintronics Research Network, Tohoku University, Sendai 980-8577, Japan

⁴WPI Research Center, Advanced Institute for Materials Research, Tohoku University, Sendai 980-8577, Japan

Since the discovery of topological insulators, the search for new material phases characterized by nontrivial topology of electronic wave functions is a hot topic in condensed-matter physics. A leading example is a topological superconductor in which gapless bound states appear at edges and/or vortex cores. The gapless bound states in topological superconductors consist of Majorana quasiparticles which have the unique property that the particle is own antiparticle, and are predicted to be useful for various applications such as fault-tolerant quantum computations. Therefore, the experimental demonstration of topological superconductivity is highly desired.

Recently, it was suggested that an iron-based superconductor Fe(Se,Te) (a superconducting transition temperature T_c of 14 K) hosts topological Dirac-cone surface states, and proximity-induced s -wave superconductivity therein leads to two-dimensional topological superconductivity with Majorana bound states in vortex cores [1].

In this study, to explore ‘high- T_c ’ topological superconductivity, we performed angle-resolved photoemission spectroscopy (ARPES) measurements of compressive-strained Fe(Se,Te) thin films which show a 1.5 times higher T_c (~23 K) than bulk counterpart [2-4], and searched for the topological surface states responsible for topological superconductivity.

High-quality compressive-strained Fe(Se,Te) thin films with the thicknesses of approximately 400 layers were grown on CaF₂ substrate by pulsed laser deposition. High-resolution ARPES measurements were performed by using a MBS-A1 spectrometer at BL7U with linearly-polarized energy-tunable photons of 7-25 eV. The clean surface necessary for the ARPES measurements was obtained by cleaving the thin film *in situ* in an ultrahigh vacuum better than 1×10^{-10} Torr.

Since the topological Dirac-cone surface states are expected to emerge at the center of the Brillouin zone in Fe(Se,Te), we performed band-structure mapping near the Γ point with high energy and momentum resolutions by utilizing a low photon energy of 7 eV at BL7U. Figure 1(a) displays the ARPES intensity map at the Fermi level plotted as a function of two-dimensional wave vector, measured in the normal state ($T = 30$ K). One can find a strong intensity spot at the Γ point and a relatively large circular-shaped intensity distribution. Next, we determined the band dispersion along the

momentum cut crossing the Γ point [Fig. 1(b)]. One can see a holelike band approaching the Fermi level in the vicinity of the Γ point, which produces the strong intensity spot in Fig. 1(a). One can also find another holelike band forming the circular Fermi surface seen in Fig. 1(a). In this study, we also performed photon-energy dependent ARPES measurements and tried to distinguish the topological surface states from the three-dimensionally-dispersive bulk states.

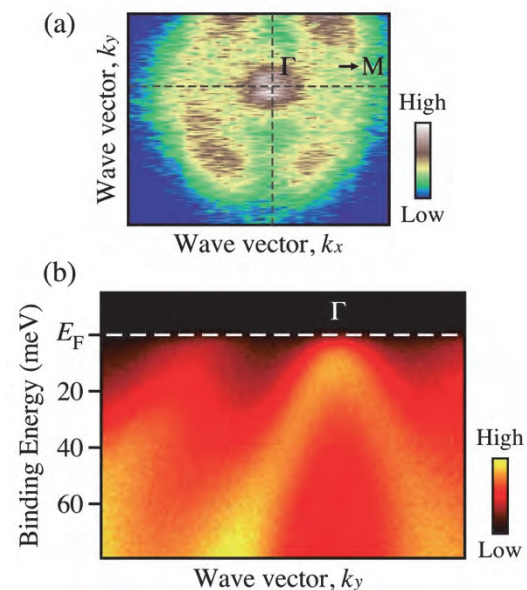


Fig. 1. (a) Fermi surface mapping plotted as a function of two-dimensional wave vector measured on compressive strained Fe(Se,Te) thin film ($T_c = 23$ K) at $T = 30$ K. (b) ARPES intensity plot as a function of binding energy and wave vector.

[1] P. Zhang *et al.*, *Science* **360** (2018) 182.

[2] F. Nabeshima *et al.*, *Appl. Phys. Lett.* **103** (2013) 172602.

[3] Y. Imai *et al.*, *Proc. Natl. Acad. Sci. USA* **112** (2015) 1937.

[4] Y. Imai *et al.*, *Sci. Rep.* **7** (2017) 46653.

BL7U

Pd-doping Dependent Energy Level of Dirac Point in $\text{Ni}_{1-x}\text{Pd}_x\text{Te}_2$ Observed by Angle Resolved Photoemission Spectroscopy

 A. Kanayama¹, K. Yoshino¹, Z. H. Tin¹, S. Miyasaka¹, S. Tajima¹, S. Ideta^{2,3} and K. Tanaka^{2,3}
¹Department of Physics, Graduate School of Science, Osaka University, Toyonaka 560-0043, Japan

²UVSOR Synchrotron Facility, Institute for Molecular Science, Okazaki 444-8585, Japan

³School of Physical Sciences, The Graduate University for Advanced Studies, SOKENDAI, Okazaki 444-8585, Japan

The Ni, Pd, and Pt dichalcogenides MX_2 (M=Ni, Pd, Pt; X=S, Se, Te) have several crystal structures such as the 2-dimensional (2D) CdI_2 -type, the pseudo-2D PdSe_2 -type and the 3-dimensional pyrite-type structures. We have studied MX_2 and their solid solution systems to explore the new physical properties. These systems show various physical properties coupled with the crystal structures.

Recently 2D CdI_2 -type MTe_2 revisited from a viewpoint of Dirac fermion [1-3]. The experimental studies on PdTe_2 and PtTe_2 have indicated that these compounds have type II Dirac fermion state [1,2]. The results of angle resolved photoemission spectroscopy (ARPES) have revealed that the Dirac point exists at $(0, 0, k_z)$ and the Dirac cone is strongly tilted along Γ -A direction (k_z -direction) in PdTe_2 and PtTe_2 . The ARPES result for related material NiTe_2 indicates that this compound also has type II Dirac cone. The Dirac point exists just above Fermi level (E_F) ($\sim +0.2$ eV) in NiTe_2 , while they in Pd and Pt systems are located around $-0.6 \sim -0.8$ eV below E_F [1-3].

We have tried to control the energy level of Dirac point in the Pd-doped NiTe_2 system $\text{Ni}_{1-x}\text{Pd}_x\text{Te}_2$. In the end members, NiTe_2 and PdTe_2 , the Dirac point is located above E_F ($\sim +0.2$ eV) and below E_F (~ -0.6 eV), respectively. We expected that the energy level of Dirac point can be turned near E_F by slightly Pd doping in NiTe_2 and the systematic change of Dirac point energy level with Pd doping can be observed by ARPES measurements.

The single crystals of $\text{Ni}_{1-x}\text{Pd}_x\text{Te}_2$ ($x=0, 0.05, \text{ and } 0.10$) were synthesized by a flux method in an evacuated silica tube. The results of the energy dispersive X-ray spectroscopy (EDX) indicated that the actual Pd concentration was the same as the nominal one. The ARPES spectra were measured at BL7U of UVSOR facility in Institute for Molecular Science using incident photons with $h\nu=10\text{-}30$ eV. All the measurements were carried out at ~ 10 K.

First of all, we measured the k_z -dependence of band structure by changing the incident photoenergy from 10 eV to 30 eV for $x=0.05$ and 0.10 samples. In all the single crystals, we observed the clear band crossing around $(0, 0, 0.37c^*)$ just below E_F indicating that these materials have Dirac point around this point. In the end member NiTe_2 , the similar k_z -dependence of band structure has been observed. Below E_F , however, we did not observe the band crossing related with the Dirac point in NiTe_2 . The present result has suggested that

the Dirac point exists above E_F , as reported previously [3].

Next, we have focused the Pd-doping dependence of Dirac point energy level. Figures 1 and 2 show the ARPES intensity plot along k_{\parallel} (parallel to Γ -M direction) at $(0, 0, 0.37c^*)$ for $x=0.05$ and 0.10, respectively. Both samples have linear band dispersion indicating the existence of Dirac cone. The Dirac point, where the two bands with linear k_{\parallel} dispersion cross, shifts down with Pd doping, as shown in Figs. 1 and 2. This result indicates that in NiTe_2 , the energy level of Dirac point can be controllable by Pd doping.

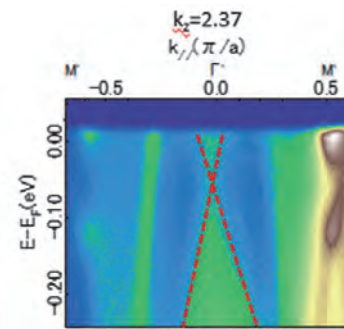


Fig. 1. ARPES intensity plot along k_{\parallel} (parallel to Γ -M direction) at $(0, 0, 0.37c^*)$ for $x=0.05$.

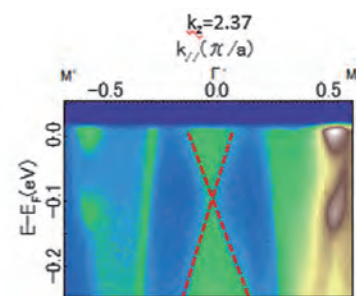


Fig. 2. ARPES intensity plot along k_{\parallel} (parallel to Γ -M direction) at $(0, 0, 0.37c^*)$ for $x=0.10$.

- [1] H.-J. Noh *et al.*, Phys. Rev. Lett. **119** (2017) 016401.
- [2] K. Zhang *et al.*, Phys. Rev. B **96** (2017) 125102.
- [3] B. Ghosh *et al.*, Phys. Rev B **100** (2019) 195134.

BL7U

Three Dimensional Comparison between the ARPES Measurements and DFT Calculation for MoS₂

S. Tanaka¹, K. Ueno², S. Ideta³ and K. Tanaka³¹ The institute of Scientific and Industrial Research, Osaka Univ., Ibaraki 567-0047, Japan² Graduate School of Science and Engineering Saitama University, Saitama 338-8570, Japan.³ UVSOR Synchrotron Facility, Institute for Molecular Science, Okazaki 444-8585, Japan.

2H-MoS₂ is one of the most typical TMDCs, and its electronic structure has been extensively studied by using angle-resolved photoelectron spectroscopy (ARPES). In these studies, comparison with the theoretical calculation was commonly made for revealing the electronic structure. However, most of the comparison has been made only on the highly symmetric lines in the Brillouin zone, and the other points are usually omitted. In this report, we made the comparison of the constant energy map derived from the photoelectron angular distribution in the ARPES measurement to those derived from the first principles calculation in the momentum space.

The experiments were carried out at the BL7U. The sample temperature was 9K and the photon energy used was 21 eV. The A-1 electron energy analyzer collects the photoelectron within the window of 30° along the photon-incident plane (defined as k_x axis hereafter), and the volume map was obtained by changing the sample tilt angle which is perpendicular to the photon incidence plane (defined as k_y axis hereafter).

The energy band of MoS₂ was calculated within the density functional theory (DFT) framework, employing the QUANTUM ESPRESSO package (version 6.3), which had been installed in the computer at Research Center for Computational Science in IMS. The eigen energies are calculated at 64×64×16 grid points in the Brillouin zone. Then, the band energies are broadened by the convolution with the Gaussian-peak function with the width of 0.05 eV at each k-point; which is a usual procedure for obtaining a density of states curve. The dispersion along the k_z line is averaged by adding all 16 spectra at one (k_x, k_y) point. The final constant-energy maps for comparing the experiments were made by the broadening in the k -space with the Gaussian function with the width of 0.02 Å⁻¹.

Figure 1 show the comparison between the constant energy maps derived from the ARPES measurements (left-hand side) and those from the DFT calculations (right-hand side). The binding energies are scaled with respect to the valence band maximum. The energy here are determined so as that the calculation and experiments show similar shape and symmetry. The relation of energies used in Figs. 1 are phenomenologically given by the formula $E_{calc} = 0.078E_{exp}^2 + 1.43E_{exp}(eV)$. This indicates that there are errors of the binding energies in the DFT calculation of this work. In spite of this considerable disagreement in the electron energy, the overall shape and symmetry in the constant-energy

map by ARPES is well represented by the calculation. This means that characteristics of the electron band is well reproduced by the DFT calculation, suggesting an advantage of the comparison in the k -space to a comparison of dispersions only on the highly symmetric lines in which the energetic agreements are necessary to match.

The method of the comparison in the three dimensions shown above, is instinctive and easy to understand. However, in order to achieve scientifically new results, it is required to take more detailed measurements combining e.g., the photon-energy-dependence and the polarization dependence, which are in progress.

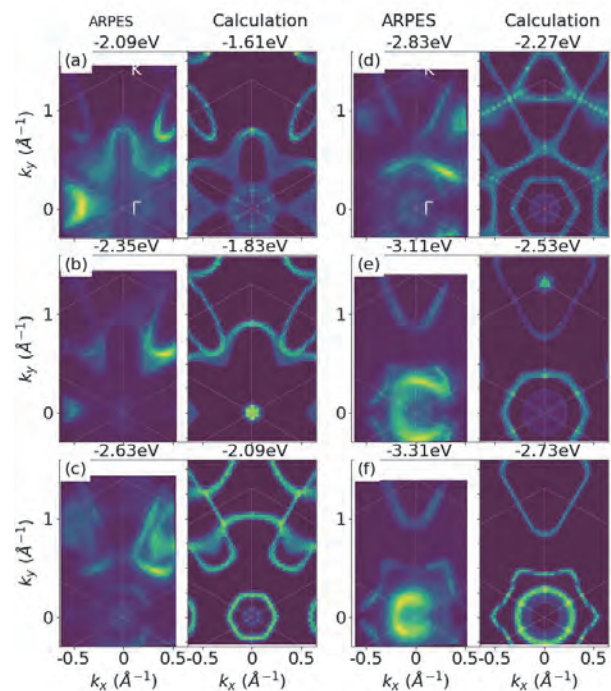


Fig. 1. Comparison of the constant energy maps between the ARPES measurements (left) and the DFT calculation(right).

BL7U

Charge Density Wave State of CeTe₃ Investigated by Angle-resolved Photoemission Spectroscopy

Y. Arai¹, K. Kuroda¹, Y. Wan¹, Y. Dong¹, Y. Fujisawa², S. Ideta³, K. Tanaka³
Y. Okada² and T. Kondo¹

¹*ISSP, University of Tokyo, Kashiwa 277-8581, Japan*

²*Quantum Material Science Unit, OIST, Onna-son 904-0495, Japan*

³*UVSOR Synchrotron Facility, Institute for Molecular Science, Okazaki 444-8585, Japan*

In strongly correlated electron systems, the many-body effect often significantly reconstructs the electronic structure of matter in the vicinity of the Fermi energy; for example, charge density wave (CDW) opens a band gap, and Kondo effect leads to heavy quasi-particle bands. The conflict or interplay among such multiple many-body effects is of great interest in condensed matter physics. CeTe₃ with 4*f* orbitals exhibits CDW state, thus offers an excellent playground to study such an intriguing physics.

CeTe₃ is composed of an alternate stacking of Te planes and CeTe slabs as shown in Fig. 1 (a). Te planes mainly contribute to the Fermi surface and host the CDW state. The transition temperature of CDW is more than 400 K [1] and the lattice originally of square Te planes is distorted by as much as 0.2 Å [2], indicating that the CDW state is quite robust; this is further confirmed by a large CDW gap as large as 400meV observed by angle-resolved photoemission spectroscopy (ARPES) [3]. The electronic state of CeTe₃ is also characterized by the Kondo effect, which is observed in the electrical resistivity increasing below 10 K with a local maximum value at 6 K [1]. Since this temperature is associated with the coherence derived from the Kondo lattice, both CDW and Kondo effects are expected to affect the electronic structure below 6 K in CeTe₃.

Although ARPES is a suitable probe to investigate the electronic reconstruction due to CDW and Kondo effect, the previous research observed the band structure only down to 25 K, where only the CDW occurs. In this study, therefore, we have conducted the ARPES measurements down to 6 K comparable with the Kondo temperature, in order to realize the coexistence between the CDW and Kondo effect and study the relationship of these.

Figure 1(b) shows the Fermi surface mapping, where the ARPES intensities are integrated from E_F to E_F-200 meV. Due to the interlayer coupling between Te planes and Ce-Te slabs, Te plane bands are folded along the three-dimensional Brillouin zone [3]. We clearly observed that a CDW gap is opened along the Fermi surface, and its size increases from $k_y \sim 0 \text{ \AA}^{-1}$ to $k_y = \pm 0.4 \text{ \AA}^{-1}$ (Fig. 1(g)), reaching the maximum of about 400 meV. This result at 6 K is consistent with the previous ARPES studies at 25 K; this indicates that CDW in the Te plane is almost independent of the Kondo effect associated with Ce ions in the slab probably because the interaction between the Ce-Te slab structure and the Te planes is relatively weak.

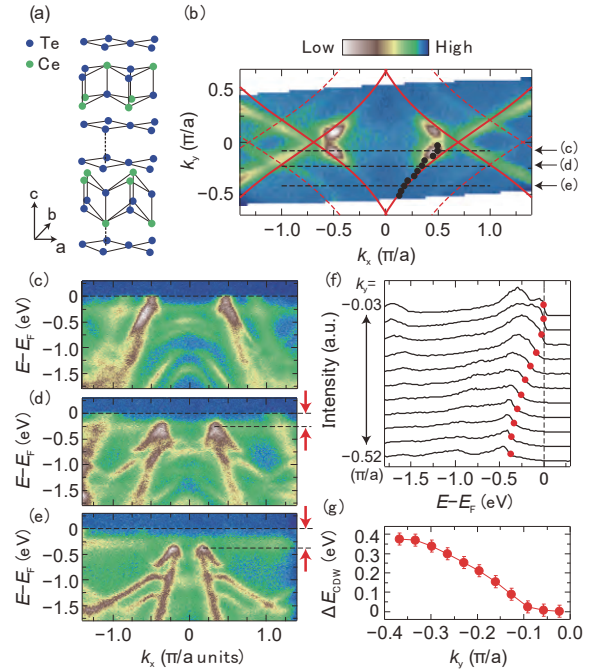


Fig. 1. Electronic structure in CDW state of CeTe₃. (a) Crystal structure of CeTe₃. Note that, unlike the convention, the *c* axis is set to be perpendicular to the Te planes. (b) Fermi surface map at 6 K measured by ARPES. Red lines represent calculated Fermi surface dominated by the Te plane, and red dotted lines are that folded about the 3D BZ [1]. (c-e) Band dispersions measured at black dotted lines in (b). Red arrows highlight CDW gaps. (f) Energy distribution curves along the Fermi surface corresponding to the black points in (b). Red points indicate the leading edge of the spectra. (g) *k* dependence of the CDW gap along (f).

[1] N. Ru *et al.*, Phys. Rev. B. **73** (2006) 033101.

[2] H. J. Kim *et al.*, Phys. Rev. Lett. **96** (2006) 226401.

[3] V. Brouet *et al.*, Phys. Rev. Lett. **93** (2004) 126405.

BL7U

High-resolution ARPES Study on the Electronic Structure of Heterointerfacial Superconductors

R. Tsubono¹, K. Nakayama¹, Y. Kubota¹, F. Nabeshima², T. Ishikawa², T. Shikama²,
A. Maeda², T. Takahashi^{1,3,4} and T. Sato^{1,3,4}

¹Department of Physics, Tohoku University, Sendai 980-8578, Japan

²Department of Basic Science, the University of Tokyo, Tokyo 153-8902, Japan

³Center for Spintronics Research Network, Tohoku University, Sendai 980-8577, Japan

⁴WPI Research Center, Advanced Institute for Materials Research, Tohoku University, Sendai 980-8577, Japan

Since the discovery of superconductivity in a LaAlO₃/SrTiO₃ heterostructure consisting of band insulators [1,2], heterointerfaces have been an interesting research target for investigating unconventional superconductivity due to the low dimensionality, spatial inversion-symmetry breaking, and interfacial interactions. A recently-discovered interfacial superconducting system is the hybrid between a topological insulator Bi₂Te₃ and a parent compound of iron-based superconductors FeTe [see Fig. 1(a) for a schematic view of the heterostructure] [3]. Although both Bi₂Te₃ and FeTe are non-superconducting, the superconducting transition temperature T_c of Bi₂Te₃/FeTe heterostructure reaches ~ 12 K, which is about ten times higher than that of LaAlO₃/SrTiO₃. This finding triggered intensive investigations on Bi₂Te₃/FeTe, and, consequently, several peculiar properties have been reported in Bi₂Te₃/FeTe and related heterostructures. An intriguing finding is the lack of interfacial superconductivity in the selenide counterpart, Bi₂Se₃/FeSe. Understanding the origin of such a remarkable difference in the superconducting property between structurally identical Bi₂Te₃/FeTe and Bi₂Se₃/FeSe would provide a key to clarify the nature of exotic interfacial superconductivity. Therefore, a comparative study on the electronic states of Bi₂Te₃/FeTe and Bi₂Se₃/FeSe is of crucial importance.

In this study, we performed high-resolution angle-resolved photoemission spectroscopy (ARPES) and determined the electronic structure relevant to the interfacial superconductivity of Bi₂Te₃/FeTe and Bi₂Se₃/FeSe. ARPES measurements at BL7U were performed using a MBS-A1 spectrometer with energy-tunable photons. The energy and angular resolutions were set to be 5–20 meV and 0.3°, respectively. The sample was kept at $T = 30$ K during the ARPES measurements.

We plot in Fig. 1 the representative ARPES results obtained on the as-grown FeSe films. As seen from Fig. 1(b), the as-grown FeSe film has small Fermi surfaces centered at the Γ and M points in the Brillouin zone. These Fermi surfaces originate from holelike and electronlike energy bands of Fe 3d orbitals [see Fig. 1(c)], indicating the semimetallic character of FeSe. Upon interfacing Bi₂Se₃ layers, we observed clear differences in the FeSe-derived energy bands. We compared these results to those obtained in Bi₂Te₃/FeTe [4] and found an important insight into the origin of interfacial superconductivity.

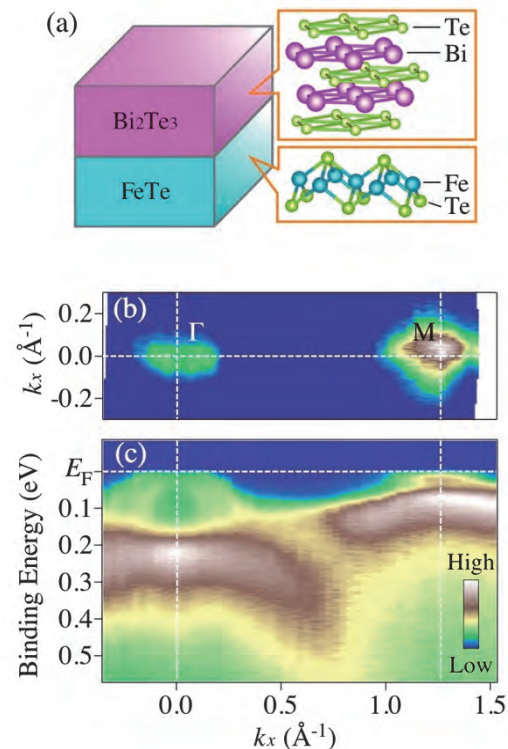


Fig. 1. (a) Schematic of Bi₂Te₃/FeTe heterostructure. (b) ARPES intensity mapping at the Fermi level plotted as a function of two-dimensional wave vector, measured at $T = 30$ K at $h\nu = 21$ eV in FeSe. (c) Experimental band dispersion measured along the Γ M high-symmetry line.

[1] A. Ohtomo and H. Y. Hwang, *Nature (London)* **427** (2004) 423.

[2] N. Reyren *et al.*, *Science* **317** (2007) 1196.

[3] Q. L. He *et al.*, *Nat. Commun.* **5** (2014) 4247.

[4] K. Owada *et al.*, *Phys. Rev. B* **100** (2019) 064518.

BL7U

Doping Dependence of the Superconducting Gap in Bi2223 Observed by Angle-Resolved Photoemission Spectroscopy

S. Ideta^{1,2}, T. Yoshida³, A. Fujimori⁴, S. Adachi⁵, N. Sasaki⁵, S. Yamaguchi⁵, T. Watanabe⁵
T. Noji⁶ and K. Tanaka^{1,2}

¹National Institutes of Natural Science, Institute for Molecular Science, Okazaki 444-8585, Japan

²The Graduate University for Advanced Studies, SOKENDAI, Okazaki 444-8585, Japan

³Graduate School of Human and Environmental Studies, Kyoto University, Kyoto 606-8501, Japan

⁴Department of Applied Physics, Waseda University, Tokyo 169-8555, Japan

⁵Graduate School of Science and Technology, Hirosaki University, Hirosaki 036-8561, Japan

⁶Department of Applied Physics, Tohoku University, Sendai 980-8579, Japan

To understand the mechanism of high- T_c superconductivity in cuprates is one of the crucial issues. Especially, the energy gap seen in the superconducting (SC) and normal states is believed to be an important piece of evidence for the non-BCS behavior of the SC transition from the underdoped to overdoped regime in the high- T_c cuprate superconductors. In cuprates, two different representative energy gaps are present in the SC and normal states, namely, the SC gap and pseudogap [1-3]. Doping dependence of the SC gap has been considered as the direct evidence to reveal high- T_c superconductivity and sheds light on its nature.

Triple-layer Bi-based cuprate superconductor, $\text{Bi}_2\text{Sr}_2\text{Ca}_2\text{Cu}_3\text{O}_{10+\delta}$ (Bi2223), which shows the highest T_c (110 K) among the Bi-based cuprates, has two inequivalent CuO_2 planes with different hole carrier [4-6]. In this study, we have investigated the momentum and doping dependence of the energy gap anisotropy and found that the SC gap obtained from different doping showed a similar magnitude. We observed two bands corresponding to the outer (OP) and inner (IP) CuO_2 planes. Hole concentration was deduced from the IP and OP Fermi surfaces actually increases in going from the underdoped to overdoped samples.

High-quality single crystals of underdoped, optimally-doped, and overdoped $\text{Bi}_2\text{Sr}_2\text{Ca}_2\text{Cu}_3\text{O}_{10+\delta}$ (UD, Opt, and OD Bi2223, $T_c = 80$ K, 110 K, and 110 K, respectively) were grown by the TSFZ method. Underdoped Bi2223 samples were successfully obtained in the two-step annealing in order to control their doping levels [7]. ARPES experiments were carried out at BL7U of UVSOR-III Synchrotron. Clean sample surfaces were obtained for the ARPES measurements by cleaving single crystals *in-situ* in an ultrahigh vacuum better than 6×10^{-9} Pa. The measurements were performed at 10 K.

In order to estimate the doping and momentum dependence of the SC gap, as shown in Fig. 1, the SC gap (10 K) estimated along the Fermi surface is plotted as a function of the d -wave order parameter. For the IP band, the extrapolated SC gap from the nodal to the antinode (a black dotted line) shows a similar magnitude at the antinode. As for the OP band too, the SC gap at the antinode shows the same magnitude in spite of different doping. Note that we need to exclude the result of the OP-bonding band (BB) [8]. These

results are similar to the double-layer cuprate $\text{Bi}_2\text{Sr}_2\text{CaCu}_2\text{O}_{8+\delta}$ observed by ARPES [9]. Here, the present ARPES study raises a question about the mechanism; why the SC transition temperature and hole carrier is different in Bi2223, the SC gap keeps the same magnitude at the antinode.

As future work, we need to investigate the pseudogap and the Fermi arc length above T_c in order to determine the relationship between the T_c and effective SC gap in Bi2223.

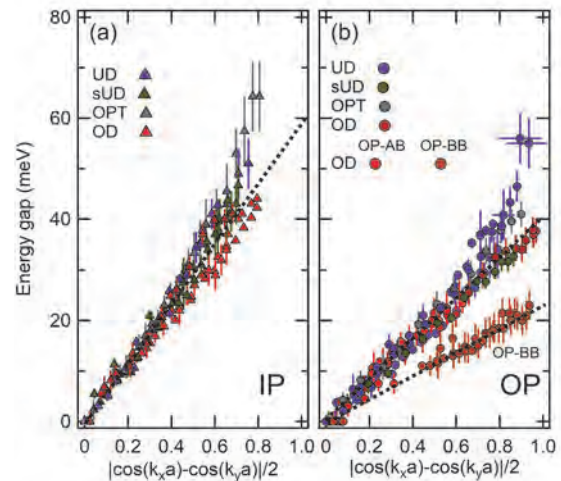


Fig. 1. Superconducting (SC) gap of Bi2223 with different doping. (a) SC gap of the IP band. (b) SC gap of the OP band.

- [1] D. S. Marshall *et al.*, Phys. Rev. B **76** (1996) 4841.
- [2] A. G. Loeser *et al.*, Science **273** (1996) 325.
- [3] H. Ding *et al.*, Nature (London) **382** (1996) 51.
- [4] S. Ideta *et al.*, Phys. Rev. Lett. **104** (2010) 227001.
- [5] S. Ideta *et al.*, Phys. Rev. B **85** (2012) 104515.
- [6] S. Ideta *et al.*, Physica C **470** (2010) S14-S16.
- [7] S. Adachi *et al.*, Physics Procedia **65** (2015) 53.
- [8] S. Ideta *et al.*, UVSOR Activity Report 2016 **44** (2017) 90.
- [9] I. M. Vishik *et al.*, PNAS **109** (2012) 18332.

BL7U

Angle-resolved Photoemission Study of MAX Phase Compound Ti_2SnC

 T. Ito^{1,2}, M. Ikemoto², D. Pinek³, M. Nakatake⁴, S. Ideta^{5,6}, K. Tanaka^{5,6} and T. Ouisse³
¹Nagoya University Synchrotron radiation Research center (NUSR), Nagoya University, Nagoya 464-8603, Japan

²Graduate School of Engineering, Nagoya University, Nagoya 464-8603, Japan

³Grenoble Alpes, CNRS, Grenoble INP, LMGP, F-38000 Grenoble, France

⁴Aichi Synchrotron Research Center, Seto, 489-0965, Japan

⁵UVSOR Synchrotron Facility, Institute for Molecular Science, Okazaki 444-8585, Japan

⁶The Graduate University for Advanced Studies, SOKENDAI, Okazaki 444-8585, Japan

MAX phase compounds, i.e., $\text{M}_{n+1}\text{AX}_n$ where M is a transition metal, A belongs to groups 13-16 and X is the C or N element, have recently been attracted much attention due to their possible application for new class of two-dimensional systems called MXenes by removing A atoms [1]. On the other hand, the bulk electronic structure of MAX phase has been studied mostly by calculations, mainly because of lack of well-established single crystalline samples. In this study, we have performed angle-resolved photoemission spectroscopy (ARPES) on MAX phase compound Ti_2SnC [2] to directly investigate the electronic structure of this system.

ARPES measurements were performed at the UVSOR-III BL5U. Data were acquired at $T = 25$ K with $h\nu = 22.5$ eV which enables us to trace around the ΓKM plane with inner potential of $V_0 = 10.7$ eV estimated from the photon energy dependent measurement (not shown). It should be noted that each ARPES images were obtained without changing the photon incident angle relative to the sample surface by utilizing two-dimensional mapping lens mode of MBS A-1 analyzer.

Figure 1 shows the obtained Fermi surface (FS) image on the ΓKM plane (a) compared with the FS topologies calculated by DFT method (b,c). Around the corner of hole-like FS (β), a broad egg-shaped FS counter has been observed. To elucidate the detail electronic structure around the observed egg-shaped FS, the band structure near the Fermi level (E_F) and momentum distribution curve (MDC) at E_F along the k_x (#1) and k_y (#2) cut across the FS are shown in Fig. 2 (a) and (b), respectively. From the comparison with DFT calculation, the egg-shaped FS seems to be in consistent with Dirac-cone like dispersive features of γ -branch. In addition, we have found the Dirac point (DP) or bottom of the upper Dirac cone locates around 250 meV from the present ARPES, while DP around 400 meV has been expected by DFT calculation. To pursue the relation between the complicated FS and the thermodynamic properties of Ti_2SnC , further studies are intended.

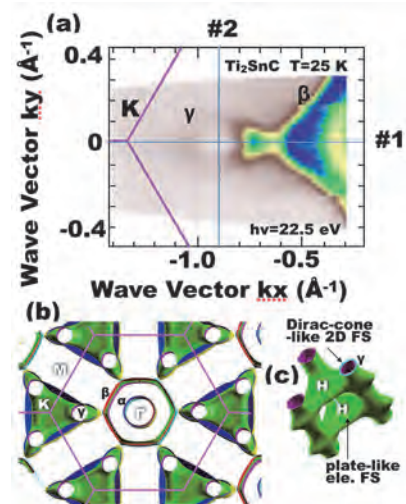


Fig. 1. Fermi surface (FS) image on ΓKM plane of Ti_2SnC (a). (b,c) FS calculated by DFT shown as projection along the $[001]$ axis (b) and enlarged FS around the KH axis (c).

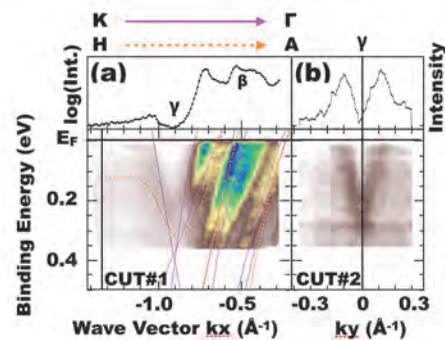


Fig. 2. Band structure near E_F (lower panel) and MDC spectra at E_F (upper panel) along the CUT#1 (a) and CUT#2 (b) indicated in Fig. 1(a) of Ti_2SnC . Dirac-cone like dispersive features have been observed on the γ -branch. Solid and dashed lines are DFT calculation along the ΓK and AH lines, respectively.

[1] M. Basoum, *MAX phases* (Wiley, Weinheim 2013).

[2] J. Y. Wu, Y. C. Zhou and J. Y. Wang, *Mat. Sci. Eng. A* **422** (2006) 266.

BL7B

Evaluation of Achromatic Vacuum-ultraviolet Lens

T. Shimizu, Y. Minami, K. Kuroda, K. Shinohara, D. Umeno and N. Sarukura
Institute of Laser Engineering, Osaka University, Suita 565-0875, Japan

Vacuum ultraviolet (VUV) has numerous scientific and technological applications including spectroscopy, environmental monitoring, surface micromachining, sterilization and so on. In the study of VUV materials, it has been found that fluoride materials can be applied as new VUV optics including lenses. For VUV lenses, the material must be transparent to the light in the VUV region, have chemical stability, have a high melting point, and be uniform and of good quality. In this study, an achromatic lens made of two materials was fabricated based on a design that minimizes chromatic aberration in the 150-300 nm range using fluoride crystals with high VUV transmittance.

A combination of LiCaF_6 and BaLiF_3 was used as materials for the convex and concave lenses of the VUV achromatic lens because it has the lowest chromatic aberration in combinations of fluoride crystals with high transmittance in the vacuum ultraviolet region. Chromatic aberration at 150 nm and 300 nm is corrected for in this design. In addition, since there is no lens adhesive that can transmit vacuum ultraviolet light, there is a gap between the convex and concave lenses, which is fixed by sandwiching them with a lens folder. The coating agent used for the anti-reflection coating, which suppresses reflections on the lens surface, is not applied because it cannot penetrate VUV light and may reduce the transmittance and degrade the vacuum due to vaporization.

The performance of VUV achromatic lenses is evaluated in the following three areas: transmittance, chromatic aberration, and focusing performance. For the transmittance measurement, VUV achromatic lenses were irradiated with synchrotron radiation of 50 to 1000 nm wavelengths at BL7B (Fig. 1). The transmittance can be measured by measuring the beam intensity of the incident light and the beam intensity after passing through the VUV achromatic lens. The transmittance of the VUV achromatic lenses was measured in the wavelength region of 100-300 nm. The absorption edge was found to be 123 nm, which is enough to transmit the light in the range of 150-300 nm, which was the target in the original design. We have concluded that the degradation of the absorption edges of LiCaF_6 and BaLiF_3 was caused by the quality of the crystals. In addition, since no AR coating was applied, it was confirmed that the overall transmittance was low due to the reflection of the lens surface.

The evaluation of chromatic aberration will be carried out in the second half of the experiment using BL3B.

In the future, a rigorous evaluation is required, and it is important to further increase the knowledge of achromatic lenses in the vacuum ultraviolet region. In addition, the development of an imaging spectrometer with a VUV achromatic lens is expected to be carried out in parallel for practical use.

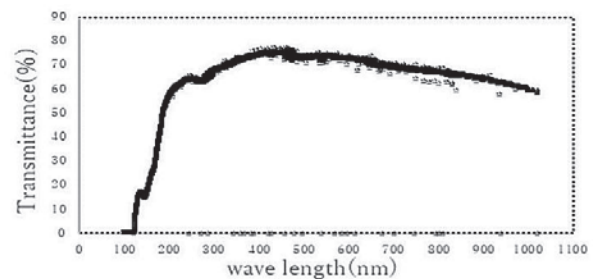


Fig. 1. Transmittance measurement results.

- [1] K. Shimamura, H. Sato, A. Bensalah, H. Machida, N. Sarukura and T. Fukuda, *J. Alloys Cmpds.* **343** (2002) 204.
- [2] M. V. Luong, M. J. F. Empizo, M. Cadatal-Raduban, R. Arita, Y. Minami, T. Shimizu, N. Sarukura, H. Azechi, M. H. Pham, H. D. Nguyen, Y. Kawazoe, K. G. Steenbergen and P. Schwerdtfeger, *Opt. Mater.* **65** (2017) 15.
- [3] R. Arita, Y. Minami, M. Cadatal-Raduban, M. H. Pham, M. J. F. Empizo, M. V. Luong, T. Hori, M. Takabatake, K. Fukuda, K. Mori, K. Yamanoi, T. Shimizu, N. Sarukura, K. Fukuda, N. Kawaguchi, Y. Yokota and A. Yoshikawa, *Opt. Mater.* **47** (2015) 462.
- [4] T. Shimizu, M. V. Luong, M. Cadatal-Raduban, M. J. F. Empizo, K. Yamanoi, R. Arita, Y. Minami, N. Sarukura, N. Mitsuo, H. Azechi, M. H. Pham, H. D. Nguyen, K. Ichiyanagi, S. Nozawa, R. Fukaya, S. Adachi, K. G. Nakamura, K. Fukuda, Y. Kawazoe, K. G. Steenbergen and P. Schwerdtfeger, *Appl. Phys. Lett.* **110** (2017) 141902.
- [5] M. V. Luong, M. Cadatal-Raduban, M. J. F. Empizo, R. Arita, Y. Minami, T. Shimizu, N. Sarukura, H. Azechi, M. H. Pham, H. D. Nguyen and Y. Kawazoe, *Jpn. J. Appl. Phys.* **54** (2015) 122602.
- [6] K. Yamanoi, T. Murata, Y. Arikawa, T. Nakazato, M. Cadatal-Raduban, T. Shimizu, N. Sarukura, M. Nakai, T. Norimatsu, H. Nishimura, H. Azechi, S. Fujino, H. Yoshida, A. Yoshikawa, N. Satoh and H. Kan, *Opt. Mater.* **35** (2013) 1962.